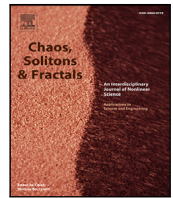


目 录

1. 代表性期刊论文 1.....	1
2. 代表性期刊论文 2.....	11
3. 代表性期刊论文 3	22
4. 代表性期刊论文 4.....	43
5. 国家自然科学基金青年项目	61
6. 第六届南京审计大学教师教学创新大赛二等奖.....	63
7. 指导全国大学生统计建模大赛省一等奖.....	64



Canards dynamics to explore the rhythm transition under electromagnetic induction

Feibiao Zhan^{a,*}, Jianzhong Su^b, Shenquan Liu^c

^a Department of Applied Mathematics, Nanjing Audit University, Nanjing 211815, China

^b Department of Mathematics, University of Texas at Arlington, Arlington, TX 76019, USA

^c School of Mathematics, South China University of Technology, Guangzhou 510640, China

ARTICLE INFO

Keywords:

Electromagnetic induction

Canards

Transition dynamics

Discharge pattern

Nociceptive neuron model

ABSTRACT

The encoding and transmission of neural information is closely related to neuronal electrophysiological activity such as spike, burst and so on. The main purpose of the paper is to explain the mechanism of transition dynamics between discharge rhythm of mathematical model for neurons under electromagnetic induction. The main dynamical system features involve torus canards. First, the dynamics of spike-burst mode and spiking patterns is demonstrated separately. In addition, the intermediate state spikes of amplitude modulation (AM spike) are found when the spike modes of the neuron are numerically calculated, and the AM mode is illustrated using torus canards. Moreover, the discharge patterns of neuron are compared when considering whether the electromagnetic induction is introduced into the system, and the effect of electromagnetic induction on the discharge rhythm is discussed. Furthermore, the existence regime of the canards phenomenon changes when the system is under the electromagnetic induction, and the dynamics of burst is also different to the original system. Finally, the function of electromagnetic induction on the dynamics of neuron bursts mode, spiking mode and transition mode between burst and spiking is explained.

1. Introduction

The discharge patterns of neuronal electrophysiological activity are closely related to neural information processing, and explaining the dynamic behavior of electrophysiological activity pattern is particularly important for understanding the encoding of neural information. This paper focuses on the neuronal rhythm of nociceptive neuron and their transition mechanism in the model using dynamical system tools. The pain channel is activated by surrounding nociceptive receptors, and it transmits signals to the nociceptive neurons through afferent neurons [1]. Nociceptive neurons have a rich spiking sequence under external stimuli [2]. The burst sequence is also considered as the basic unit of neuron information expression, which greatly improves the authenticity of signal transmission between neurons [3,4]. Discharge patterns are related to the transmission of pain signals [5]. The burst mode and spiking mode as well as the transition between them contain abundant biological information [6–11]. Recently Valero et al. have found that monitoring the subthreshold behavior of neurons is particularly important in understanding how they integrate excitatory and inhibitory inputs [12]. Therefore, it is helpful to explore the burst pattern, spike pattern and subthreshold oscillations as well as the

dynamic behavior of transitions between them for understanding the expression of biological information.

The mechanism of the spiking and burst of single neuron has been explained by some researchers before. For instances, using fast-slow dynamics to explain the firing pattern of a single neuron [13–18], or using saddle-node canards to explain the mechanism of mixed-mode oscillation [19–21]. These results describe dynamics in the firing patterns of neurons, and understanding their mathematical mechanisms is very meaningful for exploring the feedback of information expression between neurons. The main issue to study here is the transition dynamics between neuronal rhythms. Some researchers use the idea of 'blue sky catastrophe' to explain the dynamics between burst and spiking [22–25]. There are also researchers who study the transition between spiking and burst of the quasi-periodic phenomenon to analyze the dynamics of system, and discuss various torus bifurcations, including torus canards, the coexistence of resonant tori and nested torus, and complex bistable dynamics caused by the torus breakdown [26]. Roberts et al. combines the averaging method and the idea of fold singularity as well as torus canards to explain the transition between burst and spiking in the coupled neuron model [27]. Drover et al. have illustrated the delayed bifurcation using canards mechanism [28].

* Corresponding author.

E-mail address: zhanfeibiao@yeah.net (F. Zhan).

<https://doi.org/10.1016/j.chaos.2023.113304>

Received 16 December 2022; Received in revised form 7 February 2023; Accepted 21 February 2023

Available online 1 March 2023

0960-0779/© 2023 Elsevier Ltd. All rights reserved.

This paper will focus on the discharge mode of neuron system under electromagnetic induction, and mainly explains the transition dynamics between discharge rhythms using the idea of torus canards.

Kramer et al. first have discovered the relationship between the phenomenon of torus canards and neuron firing patterns in the Purkinje cell model [29], researchers have gradually proposed and discussed the torus canards phenomenon in some neuron models [30,31]. Subsequently, a mixed-type canards (limit cycle canards and torus canards coexist) is also found in the neuron model [32]. Burke et al. have reviewed several types of torus canards found in neuron models [33]. Roberts have explained the theoretical basis of canards analysis of neuron models, and he have introduced basic research methods as well as torus canards appearing in two types of neuron models [34]. Recently, Dick have analyzed the dynamics of the model before and after the nociceptive receptor is stimulated with the drug and demonstrated the possibility of the existence of canards [35]. Canards is also presented in the cardiac action potential model [36].

According to the laws of magnetoelectricity and electromagnetic induction, changes in action potentials in neurons can cause fluctuates in the surrounding magnetic flux distribution. And this fluctuation will bring about important changes in the neural network. Therefore, it is necessary to consider adding electromagnetic flux to the neuron model to ensure the reliability of the model. Recent research suggests significantly that its effect on the firing patterns of individual neurons should not be overlooked [37–39]. Buschman et al. found evidence that oscillatory synchronization of local field potentials (LFPs) formed neural ensembles representing the rules: there were rule-specific increases in synchrony at “beta” (19–40 Hz) frequencies between electrodes [40]. The change in electromagnetic induction can be expressed by calculating the magnetic flux [41,42]. We discuss the transition induced by electromagnetic flux.

The rest of this paper is organized as follows. Section 2 describes the nociceptive neuron model and explains the theoretical tools that we use in simulation. In Section 3.1, the impact of changes in external stimuli on the transition of periodic solutions is discussed. In Section 3.2, the response of the system periodic solution to electromagnetic induction is explained. In Section 4.1, the mathematical mechanism of the system discharge mode is considered. In Section 4.2, the effect of electromagnetic induction changes on the system's discharge mode mechanism is demonstrated. In Section 4.3, the sensitivity of the system bifurcation structure to electromagnetic induction is explored. Finally, we have a conclusion in Section 5.

2. Model and methods

The improved model that we propose is conductance-based Hodgkin Huxley neuron model. Here the nociceptive neuron model is used because of its rich neuronal rhythm and we add the electromagnetic induction to the sensory neurons to discuss its discharge pattern [35]. This model consists of fast inactivated sodium ion current (I_{Na_f}), medium inactivated sodium ion current (I_{Na_I}), slow inactivated sodium ion current (I_{Na_s}), leakage current (I_L) and the electromagnetic induction equation as well as external stimulus I_d . Same as the Dick [35], in this modification, we only considered to the incoming sodium currents and does not take into account the outgoing potassium currents, but uses only the leakage current as the outgoing current. We use a single slow variable r as a slow variable, which describes the inactivation of the slow sodium channel. Variable ϕ denotes the magnetic flux across the membrane, $\rho(\phi)$ represents the incremental memductance function of flux controlled memristor [42], and which is used to describe the coupling between membrane potential and magnetic flux. The incremental memductance function is often described by $\rho(\phi) = \alpha + 3\beta\phi^2$, and α, β are fixed parameters [37,42]. The term $k\rho(\phi)V$ could be viewed as induction current on the membrane as follows:

$$i' = \frac{dq(\phi)}{dt} = \frac{dq(\phi)}{d\phi} \frac{d\phi}{dt} = \rho(\phi)V_0 = k\rho(\phi)V$$

Transmembrane potential V , ion channels and magnetic flux ϕ can be described as follows:

$$\frac{dV}{dt} = (I_d - k\rho(\phi)V - I_{Na_f} - I_{Na_I} - I_{Na_s} - I_L)/C_m, \quad (1)$$

$$\frac{dx}{dt} = (x_\infty(V) - x)/\tau_x(V), \quad x = m, h, b, s, r, \quad (2)$$

$$\frac{d\phi}{dt} = k_1 V - k_2 \phi. \quad (3)$$

Where the expression of each ion current is as follows:

$$I_{Na_f} = g_{Na_f} m^3 h (V - V_{Na}),$$

$$I_{Na_I} = g_{Na_I} m_{I\infty} b (V - V_{Na}),$$

$$I_{Na_s} = g_{Na_s} s^3 r (V - V_{Na}),$$

$$I_L = g_L (V - V_L).$$

The equation of each kinetic parameter is as follows:

$$m_\infty = 1/(1 + \exp(-(34.1 + V)/9.1)),$$

$$h_\infty = 1/(1 + \exp((56.4 + V)/7.2)),$$

$$m_{I\infty} = 1/(1 + \exp(-(25.3 + V)/9.1)),$$

$$b_\infty = 1/(1 + \exp((72.5 + V)/8)),$$

$$\tau_m = 0.01 + 0.11 \exp(-0.5((V + 28.7)/25.5)^2),$$

$$\tau_h = 0.246 + 1.63 \exp(-0.5((V + 61.9)/15.3)^2),$$

$$\tau_b = 0.22 \exp(-0.07V).$$

Corresponding system parameters are: membrane capacitance $C_m = 1 \mu\text{F}/\text{cm}^2$, reversal potential $V_{Na} = 62 \text{ mV}$ (sodium) and $V_L = -77 \text{ mV}$ (leakage), maximum conductance $g_{Na} = 40 \text{ mS}/\text{cm}^2$, $g_{Na_I} = 27 \text{ mS}/\text{cm}^2$, $g_L = 1.4 \text{ mS}/\text{cm}^2$ and related electromagnetic induction parameters $\alpha = 0.4$, $\beta = 0.02$, $k = 0.001$, $k_1 = 1$. Other parameters throughout the paper is not fixed, g_{Na_s} , I_d and k_2 will be considered as bifurcation parameters. Dynamic function of slow sodium channels in nociceptive neurons change subtly before and after drug administration [35], their expressions are as follows.

The dynamic function before modifying the channel is as follows:

$$s_\infty(V) = 1/(1 + \exp(-(22 + V)/16)),$$

$$r_\infty(V) = 1/(1 + \exp((34 + V)/11)),$$

$$\tau_s(V) = 2 + 25 \exp(-((50 + V)/65)^2),$$

$$\tau_r(V) = 50 + 250 \exp(-((21 + V)/31)^2).$$

The dynamic function after modifying the channel is as follows:

$$s_\infty(V) = 1/(1 + \exp(-(10 + V)/25)),$$

$$r_\infty(V) = 1/(1 + \exp((32 + V)/11)),$$

$$\tau_s(V) = 2 + 30 \exp(-((30 + V)/85)^2),$$

$$\tau_r(V) = 45 + 250 \exp(-((19 + V)/31)^2).$$

The theoretical tools we use are torus canards [29] and Izhikevich's classification method [14]. MATCONT is an extension package in MATLAB, which has powerful nonlinear dynamic bifurcation and chaos analysis performance. This paper uses the MATLAB and MATCONT packages [43,44] for all numerical calculations and graphic rendering.

3. Periodical solution transition of discharge mode

3.1. Impact of external stimulus changes on the transition of periodical solution

Fig. 1. shows the entire transition process of the discharge mode when $g_{Na_s} = 10$. It shows in detail the regular spiking pattern with the bursts, the alternation of bursts mode and isolated spikes, periodic oscillations (with only one period), AM spike, the spiking mode, 2-spike burst with the subthreshold oscillations and the irregular slow spikes as well as the rest stationary state. This process is only achieved by

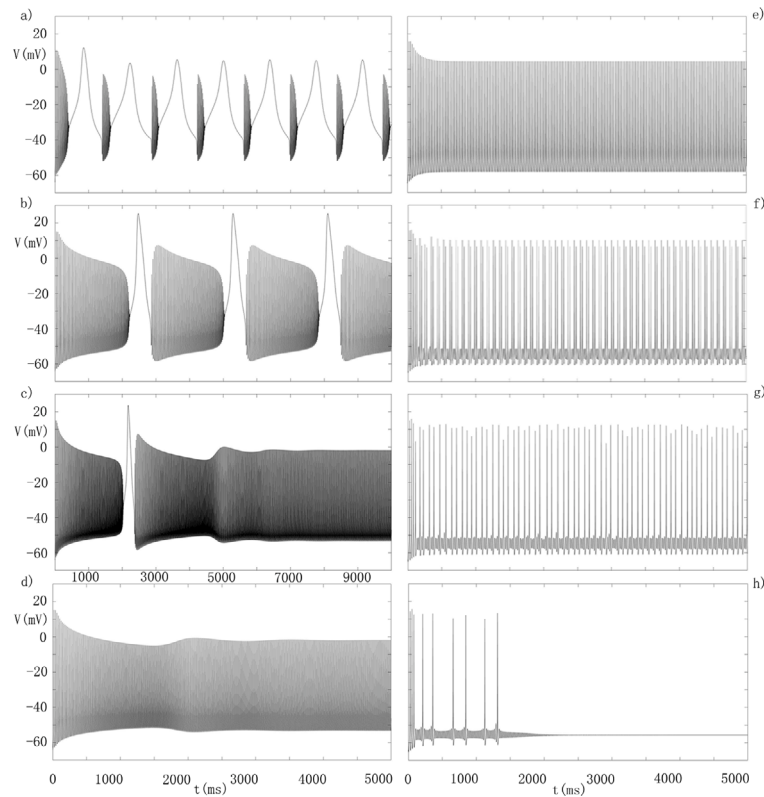


Fig. 1. Changes in the firing pattern of the system as external stimuli shifting, $g_{Nas} = 10$, $k = 0$, without adding electromagnetic induction. (a) to (h) correspond to the current stimulation of the system are 21.89, 17.73, 17.70636, 17.706, 16.5, 15.8, 15.49, 15.3, respectively.

adjusting the direct external stimulus I_d . As we can see from Fig. 1(a), there are seven regular spiking with the bursts in between. Unlike the bursts mode we usually see, the resting state of the firing pattern is replaced by bursts. At the end of each burst pattern, there is an upward jump forming a regular spiking. The dynamics behave as mixed-mode oscillations, as we studied in the paper [21]. Here, we are interested in studying the mechanism of rhythm transition in bursts mode. As the external stimulus decreases, the interval of bursts mode gradually increases and forms the bursts intercalated with isolated spikes (spike-burst mode) (Fig. 1(b)). In the range of 5000 ms, only three complete burst patterns appear, indicating that the number of peaks per burst is increasing. When continuing to reduce external stimuli, it is found that only one period spike-burst mode appears and followed by the AM spikes as well as the spiking mode (Fig. 1(c)). In Fig. 1(d), we can see that the spike-burst pattern disappears, and the AM spikes is observed. An explanation on the side is that the number of spikes in the spike-burst mode continues to increase, and it appears like the spiking pattern when the number of peaks in spike-burst is infinite. The system shows the spikes mode when the external stimulus $I_d = 16.5$ (Fig. 1(e)). Regular mixed-mode oscillation occurs when continuing to reduce external stimuli. In addition to small oscillations below the threshold value ($V = 0$), it can be found there are two different membrane voltage values in the mixed-mode oscillation (Fig. 1(f)). This mixed-mode oscillation is newly discovered. As external stimuli continuing to decrease, the mixed-mode begins to become irregular slow spikes (Fig. 1(g)), until the entire spikes state changes from spiking to resting (Fig. 1(h)). This process explains in detail how the system firing pattern changes from the spikes with the bursts mode to the spike mode through a intermediate state with the change of external stimulus parameter, and then transit from the mixed-mode to the resting state.

Fig. 2. shows the influence of electromagnetic induction on the discharge pattern of model, and its external stimulus is correspond to Fig. 1. By comparing Figs. 1(a) and 2(a), it can be seen that

regular spikes with the bursts gradually tend to resting state under the electromagnetic induction. The following discussions are expanded by comparing Figs. 1 and 2. As the external parameters decrease, the neuron model exhibits the spike-burst mode and there are four complete periods in the display range (Fig. 2(b)). From Figs. 2(c) and 2(d), it can be seen that the number of burst has not changed much. And the number of the spike in each burst remain slightly modulation, but there is not much change in the visual comparison. The tonic spike and regular mixed-mode oscillation modes are still maintained from Figs. 2(e) and 2(f). It can be seen from Fig. 2(g) that the irregular slow spikes is still greatly affected by electromagnetic induction, and the irregularity has changed greatly. Especially, the resting neuron produces discharge activities again under the influence of electromagnetic induction when $I_d = 15.3$ (Fig. 2(h)). The role of electromagnetic induction is found when considering its influence process on the discharge pattern of neurons. And it may be that the sudden transition starts from quantitative accumulation to essential jump when the external stimuli add to a determinate value. Hence it is not obvious to observe its effect on certain discharge modes. When the external stimulus exceeds some fixed value, the effect of electromagnetic induction immediately appears. Below we will also explain the dynamic properties of the system under electromagnetic induction.

3.2. Response of system periodic solution to changes of electromagnetic induction variables

Fig. 3. shows the change of the system's discharge pattern with external stimuli when $g_{Nas} = 5$. When $I_d = 24.83$, the system exhibits the bursts pattern (Fig. 3(a)). Obviously, the resting state between bursts pattern is stable. At the end of each bursts pattern, there is the resting state. It is different from the upward jump forming a regular spiking between bursts mode mentioned above (Fig. 1(a)). As shown

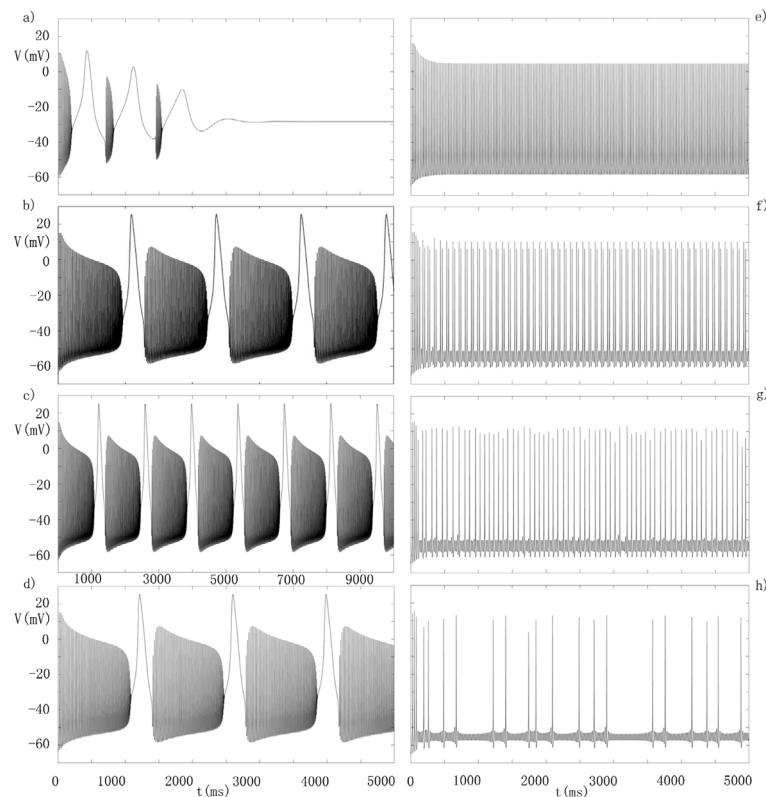


Fig. 2. Changes in the firing pattern of the system as external stimuli change, $g_{Nas} = 10$, $k_2 = 25$, with electromagnetic induction. (a) to (h) correspond to the current stimulation of the system are 21.89, 17.73, 17.70636, 17.706, 16.5, 15.8, 15.49, 15.3, respectively.

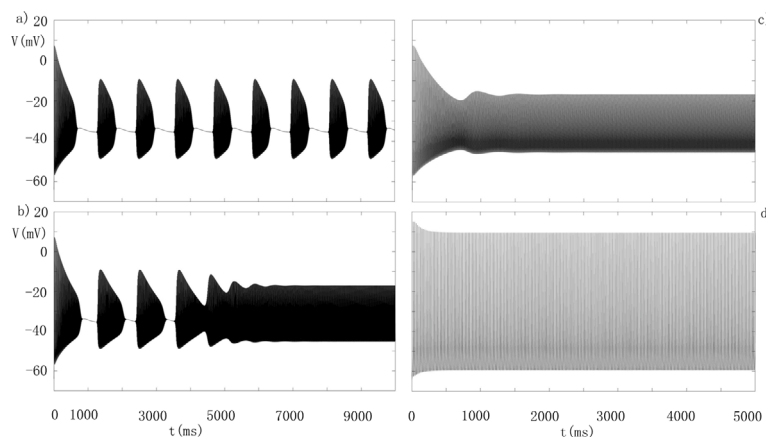


Fig. 3. Changes in the firing pattern of the system as external stimuli shifting, $g_{Nas} = 5$, $k = 0$, without adding electromagnetic induction to the system. (a)–(d) correspond to the current stimulation of the system are $I_d = 24.83, 24.7779, 24.75, 18.0$, respectively.

in Fig. 3(b), it shows a mixed-mode state. The early stage is composed of three bursting modes, and then follow by AM spikes, finally transit to spiking pattern. It is more like the display of the combination of bursting and spiking. Continuing to reduce external stimuli, the firing mode will first appear with AM spikes and finally tend to the spiking pattern (Fig. 3(c)). Similar to the transition mode mentioned earlier, the next section will explain the dynamic of the transition mode. The system behaves as a spiking mode (Fig. 3(d)) when $I_d = 18.0$. This exhibits a process in which the system discharge from the bursting to the spiking pattern.

The influence of electromagnetic induction on the discharge pattern of neuron is considered when $g_{Nas} = 5$, $I_d = 24.75$. Obviously, it

corresponds to the firing mode of Fig. 3(c) when without adding electromagnetic induction to the system. When electromagnetic induction parameter $k_2 = 2$, the system is in a resting state. It can be said that electromagnetic induction stimulation makes the neuron firing mode change from the AM spikes mode to the resting state (Fig. 4(a)). As described in Fig. 4(b), the system presents bursts mode when $k_2 = 5$, and the left-side spike of the bursts mode rises at a slower rate. With the increasing of k_2 to 25, the system firing mode presents an intermediate state, which is the transition between the bursts pattern and spiking mode. That is, the burst mode is followed by the AM mode and spiking mode (Fig. 4(c)). As shown in Fig. 4(d), the system firing shows a mixture of AM spike mode and spiking mode. Changes in electromagnetic induction have a positive effect on the transition of neuron

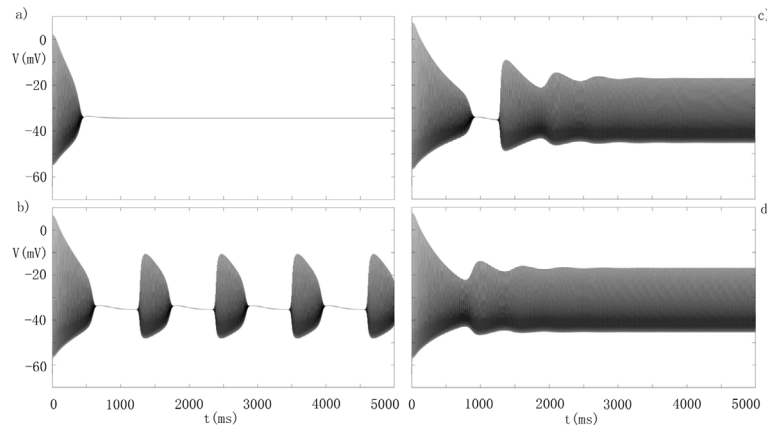


Fig. 4. Changes in the firing pattern of the system as current stimulation shifting, $g_{NaS} = 5$, $I_d = 24.75$, with electromagnetic induction. (a)–(d) correspond to the electromagnetic induction stimuli are $k_2 = 2, 5, 25, 50$, respectively.

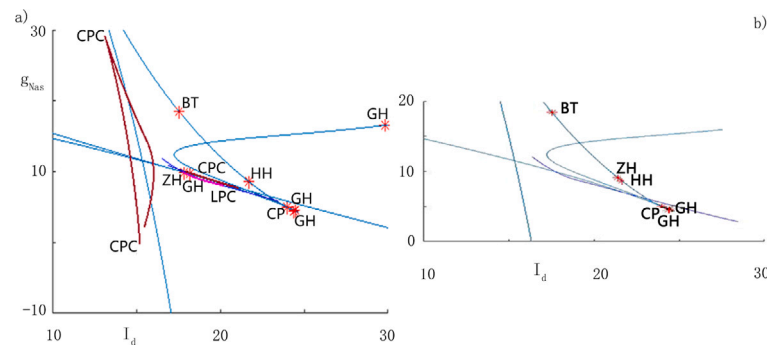


Fig. 5. (color online) The codimension-2 bifurcation diagram of the system when electromagnetic induction is added or not. (a) without adding electromagnetic induction to the system, $k = 0$; (b) system with electromagnetic induction, $k_2 = 25$. Where GH indicates Generalized Hopf bifurcation (Bautin), CP represents cusp bifurcation, HH indicates double Hopf bifurcation, ZH represents Zero-Hopf, BT represents Bogdanov–Takens bifurcation, CPC represents the cusp of the limit cycle and LPC represents the fold of limit cycle.

discharge pattern. The discharge mode can be shifted by adjusting the electromagnetic induction parameter. The discharge activity have more patterns, and the bursts interval and the number of peaks per bursts will change.

Above we have examined the effect of the system parameter g_{NaS} and external stimulus variable I_d on the discharge mode. Next, we use these two parameters to do a codimension-2 analysis, and compare its bifurcation diagram before and after electromagnetic induction is added (Fig. 5.). MATCONT software package is used to calculate and obtain many codimension-2 bifurcation points when electromagnetic induction is added to the system or not. The rich bifurcation diagram means that it has complex dynamic properties. And we find the cusp bifurcation point of the cycle and the double Hopf point, etc (Fig. 5(a)), which are not easy to find. Here we focus on the pink LPC bifurcation curve. The basic bifurcation curves such as the Hopf curve, saddle-node curve and NS curve are retained (Fig. 5(b)). That is, the whole bifurcation structure of the system is still there. The system may become more robust when electromagnetic induction is introduced into the system, and LPC bifurcation curve cannot be detected. However, it may be that the software cannot implement, and that does not mean it does not exist. Therefore, the system dynamics have changed slightly. The transition of discharge modes associated with this LPC bifurcation change will be examined in more detail below. Here we will focus on the transition of discharge rhythm and AM spikes mode. The discussion of these phenomena can give a deeper understanding of the dynamic characteristics of the system.

4. Dynamics mechanism of discharge mode

4.1. Mathematical mechanism of system firing mode

Comparing the time variables of each ion channel, it can be seen that the time variable τ_r is much larger than the time variables of other ion channels. So this section will consider r as a slow variable parameter to illustrate the mechanism of dynamic behavior patterns. That is, a single slow variable r was used as a slow variable, which describes the inactivation of the slow sodium channel. Quantitative analysis of the system is necessary to obtain the stable solution of the system before and after the electromagnetic induction is added. First, the equilibrium point (blue trajectory) and limit cycle of the system are calculated when $I_d = 17.73$, and the maximum and minimum values of the limit cycle are represented by the red point trajectory. The phase diagrams of the system are superimposed on the plane together, as shown in Fig. 6(a). The three-dimensional phase space of the discharge pattern is shown in Figs. 6(b), and 6(a) is partially enlarged and shown in Fig. 6(c). Examining the change of r over time, we can find that the system trajectory starts firing downward via the LP point. Until it hits the fold of limit cycle, the trajectory have produced the firing that gradually decrease the interval of the spikes. This process will form a burst pattern. After passing through the fold of the limit cycle, the trajectory is gradually restricted by the unstable limit cycle. The trajectory will make an upward jump when it has through a finite rotation and reaches a radius of zero, and eventually it tends to an upward jump forming a regular spiking. The same process will be

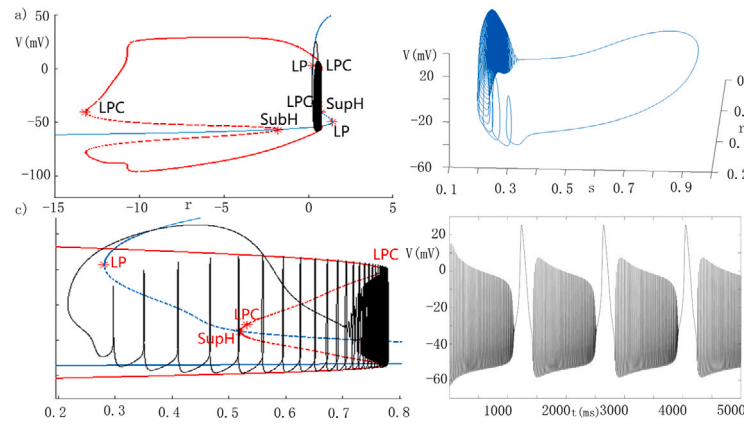


Fig. 6. (color online) Bifurcation dynamic analysis of the system when without adding electromagnetic induction to the system, $g_{Nas} = 10$, $k = 0$, $I_d = 17.73$. (a) The superposed diagram of the equilibrium point of the system and phase plane diagram as well as the maximum and minimum values of the limit cycle; (b) three-dimensional spike phase diagram of the system; (c) is a partial enlarged view of the figure (a); (d) membrane potential time series diagram. Red curve represents the set of maximum and minimum value of limit cycles, black curve represents the phase plane diagram of the trajectory, and the blue curve is the equilibrium point of the fast subsystem. LPC represents the fold of limit cycle, LP represents saddle-node bifurcation, SubH represents Subcritical Hopf bifurcation, SupH represents Supercritical Hopf bifurcation. Reader should compare with Fig. 1(b). (For interpretation of the references to color in this figure legend, the reader is referred to the web version of this article.)

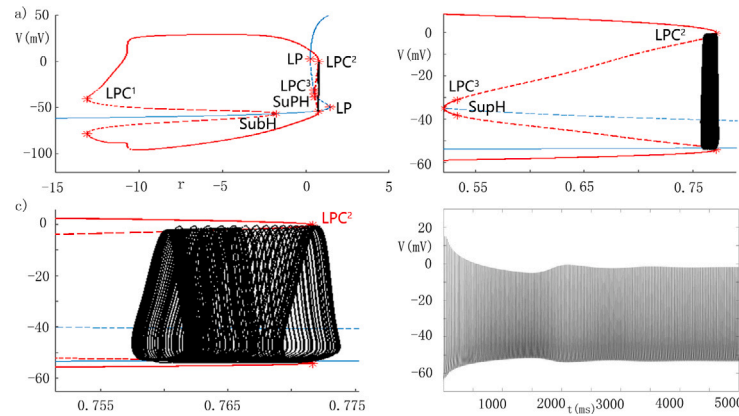


Fig. 7. (color online) Bifurcation dynamic analysis of the system when without adding electromagnetic induction to the system, $g_{Nas} = 10$, $k = 0$, $I_d = 17.706$. (a) The superposed diagram of the equilibrium point of the system and phase plane diagram as well as the maximum and minimum values of the limit cycle; (b) and (c) is a partial enlargement of (a); (d) membrane potential time series diagram. The explanation of each label is the same as in Fig. 6. Reader should compare with Fig. 1(d).

repeated next. This firing behavior can be regarded as “fold/fold circle” discharge mode.

The system numerical solution changes substantially when $I_d = 17.706$. As shown in Fig. 7(a), we have only partly intercepted the phase diagram of the AM spike and overlaid them to the system phase plane. The superposed trajectory is enlarged and displayed in Fig. 7(b) and (c). It can be observed that the phase trajectory wanders in the area to the left of the LPC^2 bifurcation. As shown in Fig. 7(b), the inner side of the red curve indicates the maximum and minimum values of the unstable limit cycle, and the outer side indicates the maximum and minimum values of the stable limit cycle. The joint effect of the two type limit cycle makes the trajectory solution of the system hover in small intervals. Because the existence interval of AM spike is very small, this range is generally easily ignored in simulation calculations. Later analysis find that there is a Neimark–Sacker (NS) bifurcation in the bifurcation structure of the system, and there is a saddle-node bifurcation points of the limit cycle. There are branch of repelling and attracting limit cycle near the LPC^2 . They are the basic conditions for the occurrence of torus bifurcation. We find that a torus bifurcation is formed near the LPC^2 of the fast subsystem. It is closely related to the AM spike mode. As the parameter r changes, the alternation of

the unstable limit cycle (repelling branch) and the stable limit cycle (attracting branch) will continue for a long time. The external stable limit cycle continuously transitions to the internal unstable limit cycle via the saddle-node of the limit cycle. As the parameter r decreases, the internal unstable limit cycle and the external stable limit cycle combine to form a loop. In this way, a torus is formed in numerical simulation. This canards mode is called “headless canard”. The discharge mode mentioned in Fig. 6. is similar to the “head canard”. If the stable limit cycle and the unstable limit cycle hit at the fold of the limit cycle (LPC), the unstable limit cycle is not bound by the outer stable limit cycle, and returns to the attracting equilibrium point via the saddle-node to continue this discharge process, this is the formation process of the spike-burst mode. This discharge pattern is known as the torus canards.

When $I_d = 16.5$, the system discharge mode behaves as a spiking. The dynamic bifurcation diagram is shown in Figs. 8, and 8(b) is a partial enlargement of it. It can be seen that the stable periodic trajectory of the system under the parameter is shown in the figure. The dynamic bifurcation structure of the fast subsystem is still maintained. There is a stable limit cycle corresponding to the spiking. Changing the external parameters makes the spike-burst mode transition to the spiking mode via the intermediate state AM spike. A similar process

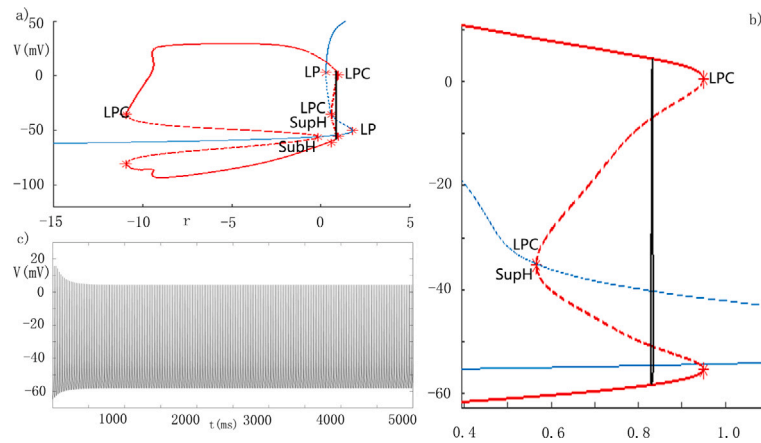


Fig. 8. (color online) Bifurcation dynamic analysis of the system when without adding electromagnetic induction to the system, $g_{Nas} = 10$, $k = 0$, $I_d = 16.5$. (a) The superposed diagram of the equilibrium point of the system and phase plane diagram as well as the maximum and minimum values of the limit cycle; (b) is a partial enlarged view of the figure (a); (c) membrane potential time series diagram. The explanation of each label is the same as in Fig. 6. Reader should compare with Fig. 1(e).

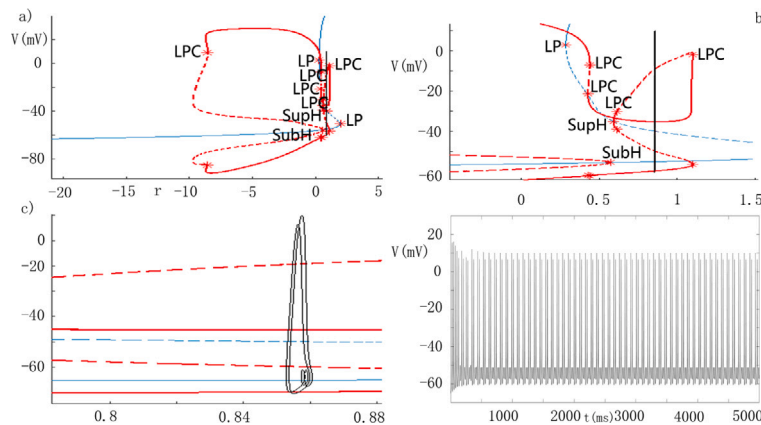


Fig. 9. (color online) Bifurcation dynamic analysis of the system when without adding electromagnetic induction to the system, $g_{Nas} = 10$, $k = 0$, $I_d = 15.8$. (a) The superposed diagram of the equilibrium point of the system and phase plane diagram as well as the maximum and minimum values of the limit cycle; (b) and (c) is a partial enlargement of (a); (d) membrane potential time series diagram. The explanation of each label is the same as in Fig. 6. Reader should compare with Fig. 1(f).

has also been mentioned in previous article [22,29]. The discussion on the spiking and spike-burst mode as well as intermediate states are also helpful for the research of neural networks. The following section will also discuss the effect of electromagnetic induction on the transition of neuronal firing patterns.

By comparing the dynamic bifurcation diagram, we can find that its structure has significantly changed when $I_d = 15.8$. As shown in Fig. 9(a), the saddle-node bifurcation of the limit cycle appears many times. Zooming in on the figure is shown in Figs. 9(b) and 9(c). It can be clearly seen that the bifurcation structure of the fast subsystem has an extra saddle-node bifurcation of limit cycle. The trajectory forms an unstable limit cycle after passing through the Subcritical Hopf bifurcation point. As the parameter r increases, the limit cycle gradually approaches the saddle-node of the cycle. The stable limit cycle not remains outside the unstable branch, but the maximum and minimum of the limit cycle are smaller than the unstable limit cycle, and they appear alternately. It then go through the second saddle-node bifurcation of the limit cycle and turn to the next unstable limit cycle trajectory. As we can see from Fig. 9(c), the mixed-mode oscillation is consist of two large-amplitude and two small-amplitude oscillations. The four red curves are the maximum and minimum values of the unstable limit cycle curve (first and third), and the maximum and minimum values of the stable limit cycle curve (second and fourth). Under the combined action of the stable limit cycle and the unstable limit cycle, the mixed oscillation mode is formed under this parameter.

4.2. Effect of electromagnetic induction changes on system discharge mode

This section discusses the dynamics behaviors of the system under electromagnetic induction. The corresponding system parameters are $g_{Nas} = 5$, $I_d = 24.75$. The bifurcation diagram is shown in Fig. 10. when $k_2 = 5$. The equilibrium point curve has four turns (four saddle-nodes) instead of the “z” type curve as we known earlier. It can be found that there are not only saddle-nodes and Hopf bifurcation point, but also the saddle-node of limit cycle (LPC), period doubling point (PD) and NS bifurcation point. This also makes the system’s discharge mode and dynamic behavior more abundant. Fig. 10(b) shows the three-dimensional phase space of the system under this set of parameters, and this spatial graph is more like a torus. The dynamics of specific bursts patterns can be obtained from Fig. 10(c), which is partial enlargement of Fig. 10(a). First, the system trajectory begins to produce spike via the Subcritical Hopf bifurcation point, and then reaches the LPC² under the action of the external attracting branch, finally it turns to the internal repelling branch. The system trajectory returns to equilibrium point under the joint action of the internal repelling branch and the external attracting branch. It will be spike again through the Subcritical Hopf point, and repeating this process will form a bursts mode state. The discharge mode process is called “SubHopf/fold circle”. We can see the variation trend of instantaneous firing rate under the bursts mode in Fig. 10(e).

The dynamic bifurcation diagram is shown in Fig. 11. when the electromagnetic induction parameter $k_2 = 25$. The structure of its

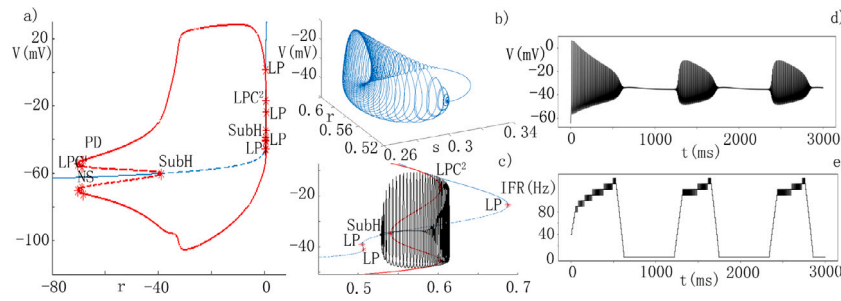


Fig. 10. (color online) Bifurcation dynamic analysis diagram when the system with the electromagnetic induction, $g_{Nas} = 5$, $I_d = 24.75$, $k_2 = 5$. (a) The superposed diagram of the equilibrium point of the system and phase plane diagram as well as the maximum and minimum values of the limit cycle; (b) three-dimensional spike phase diagram of the system. (c) is a partial enlargement of (a); (d) is the time series of membrane voltage at this parameter; (e) is the instantaneous firing rate (IFR) corresponding to the time series of membrane voltage. PD indicates period-doubling bifurcation, NS indicates Neimark–Sacker bifurcation, the other labels are the same as in Fig. 6. Reader should compare with Fig. 4(b).

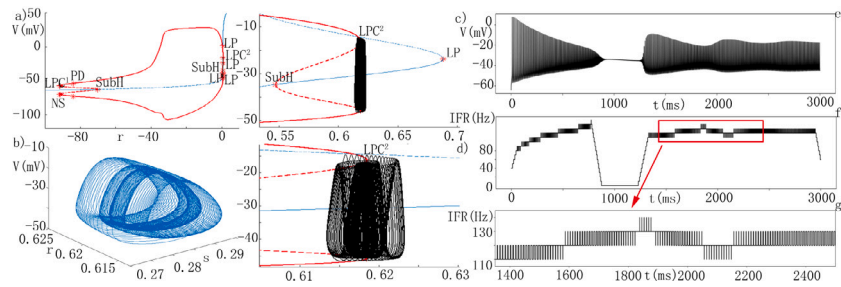


Fig. 11. (color online) Bifurcation dynamic analysis diagram when the system with the electromagnetic induction, $g_{Nas} = 5$, $I_d = 24.75$, $k_2 = 25$. (a) The superposed diagram of the equilibrium point of the system and phase plane diagram as well as the maximum and minimum values of the limit cycle; (b) three-dimensional spike phase diagram of the system. (c) and (d) is a partial enlargement of (a); (e) is the time series of membrane voltage at this parameter; (f) is the instantaneous firing rate (IFR) corresponding to the time series of membrane voltage; (g) is a partial enlargement of (f). The explanation of each label is the same as in Fig. 10. Reader should compare with Fig. 4(c).

equilibrium point curve also appears with four saddle-nodes, LPC point, Hopf bifurcation point, period doubling bifurcation point and NS bifurcation point. The three-dimensional discharge pattern diagram of AM spike under these parameters is shown in Fig. 11(b), which is a torus structure. The observation of the local enlargement of the dynamic structure is shown in Fig. 11(c). Fig. 11(d) is a partial enlargement again, and the formation process of the torus is illustrated. The stable period formed by the trajectory gradually approaches the saddle-node of limit cycle under the action of attracting branches, and the unstable period trajectory gradually shifts also the LPC². Eventually, the stable and unstable bifurcation makes the trajectory wander around the saddle-node of limit cycle. A torus canards is formed under their interactions, which is related to the AM spike mode. In the bifurcation diagram, the occurrence of the Neimark–Sacker bifurcation is found, and there are stable and unstable periodic trajectories as well as saddle-node of limit cycle. These are necessary ingredients to the formation of the torus canards. By comparing the result as shown in Figs. 10 and 11., we find that the most obvious difference is that the electromagnetic induction affects the starting point of spike (the first 1000 ms are not full bursts). In Fig. 11(f), we observed that the instantaneous firing rate of AM spike increased first and then decreased. This discharge pattern is also known as the torus canards.

4.3. Sensitivity of system bifurcation structure to electromagnetic induction

This section shows the changes of the dynamic bifurcation diagram before and after the model modification under electromagnetic induction (Fig. 12.). External stimulus I_d as a bifurcation parameter, where Fig. 12(a) represents the system bifurcation diagram before modification, and Fig. 12(b) represents the modified system bifurcation diagram. Comparing the two graphs, the most obvious change is that the two equilibrium point curves are different. The system equilibrium point before modification can detect the existence of the

saddle-node, and the saddle-node disappears after modification. The existence regime of the limit cycle of the modified system becomes larger. One significant change is that the supercritical Hopf before the modification is changed to the subcritical Hopf after the modification. From Fig. 12(b), we can see that the interval between NS bifurcation points is smaller than before the modification. This shows that the addition of electromagnetic induction causes substantial changes in the dynamic properties of the system. Electromagnetic induction can be used to detect potential dynamic changes before and after model modification, and then feedback for model adjustment.

5. Discussion and conclusions

This paper mainly discusses the effect of electromagnetic induction on the transition of neuron rhythm patterns. We have to conclude that electromagnetic induction makes the system more robust. The addition of magnetic flux makes the less bifurcation and when electromagnetic induction is added to the model, the discharge modes are more stable than before. We have discussed the different discharge modes of neurons caused by adding electromagnetic induction to the system, and understood that the influence of electromagnetic induction on the discharge rhythm patterns of neurons cannot be ignored. By comparing Figs. 1 and 2, it can be found that the addition of electromagnetic induction changes the discharge rhythm of the original system with the same external stimulation parameters I_d (especially (a), (c), (d) in Figs. 1 and 2). It can be seen from the change of Figs. 1(d) and 2 that the introduction of electromagnetic induction transit the AM spike caused by the torus canards into a regular rhythm bursting discharge. By comparison with Figs. 3(c) and 4, it is found that the difference of electromagnetic induction makes the system discharge present diversity. Meanwhile, with the increase of electromagnetic induction, the system discharge transit from “SubHopf/fold circle” bursts to the AM spiking caused by the torus canards. Therefore, electromagnetic

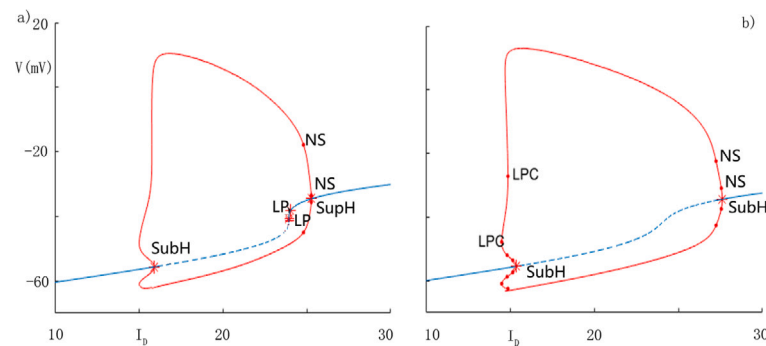


Fig. 12. (color online) Bifurcation dynamic analysis diagram of the system with electromagnetic induction when I_d is used as a bifurcation parameter, $g_{Nas} = 5$, $k_2 = 25$. (a) Superposition of the equilibrium point and the maximum and minimum of the limit cycle before the system modification; (b) Superposition of the equilibrium point and the maximum and minimum of the limit cycle after the system modification. The explanation of each label is the same as in Fig. 10.

induction is very sensitive to the intermediate states of discharge mode. The intervention of electromagnetic induction can make the original regular spiking with the bursts mode into a resting state and can also change the original resting state to a spike state as well as make the range of the intermediate state of AM spike mode change. The dynamic bifurcation diagram of the neuron model about the external stimulation parameter I_d and the maximum conductance g_{Nas} is discussed. The mechanism of firing dynamics of adding electromagnetic induction to the fast subsystem is explained. We have discovered the existence of “fold/fold circle” spike-burst mode, and the torus canards of the system without adding electromagnetic induction. Necessary conditions for torus canards exist, that is, saddle-node periodic orbit and Neimark-Sacker bifurcation as well as repelling cycle branch. The “SubHopf/fold circle” bursts pattern under electromagnetic induction is discovered, and the torus canards under electromagnetic induction also appear. The formation of torus canards is explained in detail. We have compared the changes in the dynamic bifurcation diagram before and after model modification. The paper have described the transition between neuron firing patterns under the effect of electromagnetic induction. First of all, it is emphasized that the separate discussion of the discharge pattern of a single neuron model has been explained, and there are also a large number of studies on the dynamics of single burst mode or spiking mode. Canards has been found in nerve system model and aircraft ground dynamics as well as chemical reactions [21,45–48], so, the study of canards phenomenon is helpful to solve practical problems. Electromagnetic induction cannot be ignored in many real problems, including the effect on neurons [37–42]. The study on the dynamics of rhythm transition induced by canards under electromagnetic induction in this paper is helpful for deep understanding of neurons, and the results may provide some reference for experimental neuroscience. Discussion about the transition dynamics between various burst modes, between spiking modes, between burst and spiking modes and between various types of mixed-mode burst has been endless. This paper focuses on the transition dynamics of mathematical models of neurons under electromagnetic induction. In future research, the research on the transition dynamics between the firing modes will also continue to be strengthened.

CRediT authorship contribution statement

Feibiao Zhan: Conceptualization, Methodology, Investigation, Writing – original draft. **Jianzhong Su:** Writing – review & editing, Supervision. **Shenquan Liu:** Conceptualization, Validation, Writing – review & editing.

Declaration of competing interest

The authors declare that they have no known competing financial interests or personal relationships that could have appeared to influence the work reported in this paper.

Data availability

Data will be made available on request.

Acknowledgments

This work was supported by the National Natural Science Foundation of China (Grant No. 12202208 and 11872183), the Basic Science (Natural Science) Research Project of Colleges and Universities of Jiangsu Province, China (Grant No. 22KJB130009), the Research and Cultivation Project for Young Teachers of Nanjing Audit University, China (Grant No. 2021QNPY015), 2022 Doctoral program of Entrepreneurship and Innovation in Jiangsu Province, China and the China Scholarship Council (Grant No. 201906150100).

References

- [1] Boucher TJ, McMahon SB. Neurotrophic factors and neuropathic pain. *Curr Opin Pharmacol* 2001;1:66–72. [http://dx.doi.org/10.1016/S1471-4892\(01\)00010-8](http://dx.doi.org/10.1016/S1471-4892(01)00010-8).
- [2] Michaelis M, Liu X, Janig W. Axotomized and intact muscle afferents but no skin afferents develop ongoing discharges of dorsal root ganglion origin after peripheral nerve lesion. *J Neurosci* 2000;20:2742–8. <http://dx.doi.org/10.1523/JNEUROSCI.20-07-02742.2000>.
- [3] Lisman JE. Bursts as a unit of neural information: Making unreliable synapses reliable. *Trends Neurosci* 1997;20:38–43. [http://dx.doi.org/10.1016/S0166-2236\(96\)10070-9](http://dx.doi.org/10.1016/S0166-2236(96)10070-9).
- [4] Izhikevich EM, Desai NS, Walcott EC, Hoppensteadt FC. Bursts as a unit of neural information: Selective communication via resonance. *Trends Neurosci* 2003;26:161–7. [http://dx.doi.org/10.1016/S0166-2236\(03\)00034-1](http://dx.doi.org/10.1016/S0166-2236(03)00034-1).
- [5] Devor M. Ectopic discharge in $a\beta$ afferents as a source of neuropathic pain. *Exp Brain Res* 2009;196:115–28. <http://dx.doi.org/10.1007/s00221-009-1724-6>.
- [6] Eyherabide HG, Rokem A, Herz AVM, Samengo I. Burst firing is a neural code in an insect auditory system. *Front Computat Neurosci* 2008;2:3. <http://dx.doi.org/10.3389/neuro.10.003.2008>.
- [7] Kepecs A, Lisman J. How to read a burst duration code. *Neurocomputing* 2004;58–60:1–6. <http://dx.doi.org/10.1016/j.neucom.2004.01.014>.
- [8] Stanley GB. Reading and writing the neural code. *Nature Neurosci* 2013;16:259–63. <http://dx.doi.org/10.1038/nn.3330>.
- [9] Bialek W, Rieke F, Steveninck R, Warland D. Reading a neural code. *Science* 1991;252:1854–7. <http://dx.doi.org/10.1126/science.2063199>.
- [10] Brown EN, Frank LM, Tang D, Quirk MC, Wilson MA. A statistical paradigm for neural spike train decoding applied to position prediction from ensemble firing patterns of rat hippocampal place cells. *J Neurosci* 1998;18:7411–25. <http://dx.doi.org/10.1523/JNEUROSCI.18-18-07411.1998>.
- [11] Quiroga RQ, Panzeri S. Extracting information from neuronal populations: Information theory and decoding approaches. *Nature Rev Neurosci* 2009;10:173–85. <http://dx.doi.org/10.1038/nrn2578>.
- [12] Valero M, Zutshi I, Yoon E, Buzsaki G. Probing subthreshold dynamics of hippocampal neurons by pulsed optogenetics. *Science* 2022;375:570–4. <http://dx.doi.org/10.1126/science.abm1891>.
- [13] Rinzel J. A formal classification of bursting mechanisms in excitable systems. Berlin: Heidelberg; 1987.
- [14] Izhikevich EM. Neural excitability, spiking and bursting. *Int J Bifurcation Chaos* 2000;10:1171–266. <http://dx.doi.org/10.1142/S0218127400000840>.
- [15] Izhikevich EM, Hoppensteadt F. Classification of bursting mappings. *Int J Bifurcation Chaos* 2004;14:3847–54. <http://dx.doi.org/10.1142/S0218127404011739>.

- [16] Yang Z, Lu Q. Different types of bursting in chay neuronal model. *Sci China Ser G* 2008;51:687–98. <http://dx.doi.org/10.1007/s11433-008-0069-7>.
- [17] Wang J, Lu B, Liu S, Jiang X. Bursting types and bifurcation analysis in the pre-botzinger complex respiratory rhythm neuron. *Int J Bifurcation Chaos* 2017;27:1750010. <http://dx.doi.org/10.1142/S0218127417500109>.
- [18] Zhan F, Liu S, Wang J, Lu B. Bursting patterns and mixed-mode oscillations in reduced purkinje model. *Internat J Modern Phys B* 2018;32:1850043. <http://dx.doi.org/10.1142/S0217979218500431>.
- [19] Desroches M, Guckenheimer J, Krauskopf B, Kuehn C, Osinga HM, Wechselberger M. Mixed-mode oscillations with multiple time scales. *SIAM Rev* 2012;54:211–88. <http://dx.doi.org/10.1137/100791233>.
- [20] Bröns M, Krupa M, Wechselberger M. Mixed mode oscillations due to the generalized canard phenomenon. *Fields Inst Commun* 2006;49:39–63. <http://dx.doi.org/10.1090/fic/049/03>.
- [21] Zhan F, Liu S, Zhang X, Wang J, Lu B. Mixed-mode oscillations and bifurcation analysis in a pituitary model. *Nonlinear Dynam* 2018;94:807–26. <http://dx.doi.org/10.1007/s11071-018-4395-7>.
- [22] Shilnikov A, Cymbalyuk G. Transition between tonic spiking and bursting in a neuron model via the blue-sky catastrophe. *Phys Rev Lett* 2005;94:048101. <http://dx.doi.org/10.1103/PhysRevLett.94.048101>.
- [23] Malashchenko T, Shilnikov A, Cymbalyuk G. Six types of multistability in a neuronal model based on slow calcium current. *PLoS One* 2011;6:e21782. <http://dx.doi.org/10.1371/journal.pone.0021782>.
- [24] Shilnikov A, Calabrese RL, Cymbalyuk G. Mechanism of bistability: Tonic spiking and bursting in a neuron model. *Phys Rev E* 2005;71:056214. <http://dx.doi.org/10.1103/PhysRevE.71.056214>.
- [25] Shilnikov AL, Cymbalyuk G. Homoclinic bifurcations of periodic orbits en a route from tonic spiking to bursting in neuron models. *Regul Chaotic Dyn* 2004;9:281–97. <http://dx.doi.org/10.1070/RD2004v009n03ABEH000281>.
- [26] Ju H, Neiman AB, Shilnikov AL. Bottom-up approach to torus bifurcation in neuron model. *Chaos* 2018;28:106317. <http://dx.doi.org/10.1063/1.5042078>.
- [27] Roberts KL, Rubin JE, Wechselberger M. Averaging, folded singularities, and torus canards: Explaining transitions between bursting and spiking in a coupled neuron model. *SIAM J Appl Dyn Syst* 2015;14:1808–44. <http://dx.doi.org/10.1137/140981770>.
- [28] Drover J, Rubin J, Su J, Ermentrout B. Analysis of a canard mechanism by which excitatory synaptic coupling can synchronize neurons at low firing frequencies. *SIAM J Appl Math* 2004;65:69–92. <http://dx.doi.org/10.1137/S0036139903431233>.
- [29] Kramer MA, Traub RD, Kopell NJ. New dynamics in cerebellar purkinje cells: Torus canards. *Phys Rev Lett* 2008;101:068103. <http://dx.doi.org/10.1103/PhysRevLett.101.068103>.
- [30] Nicholas G Benes, Barry AM, Kaper TJ, Kramer MA, Burke J. An elementary model of torus canards. *Chaos* 2011;21:023131. <http://dx.doi.org/10.1063/1.3592798>.
- [31] Burke J, Desroches M, Granados A, Kaper TJ, Krupa M, Vo T. From canards of folded singularities to torus canards in a forced van der Pol equation. *J Nonlinear Sci* 2016;26:405–51. <http://dx.doi.org/10.1007/s00332-015-9279-0>.
- [32] Desroches M, Burke J, Kaper TJ, Kramer MA. Canards of mixed type in a neural burster. *Phys Rev E* 2012;85:021920. <http://dx.doi.org/10.1103/PhysRevE.85.021920>.
- [33] Burke J, Desroches M, Barry AM, Kaper TJ, Kramer MA. A showcase of torus canards in neuronal bursters. *J Math Neurosci* 2012;2:3. <http://dx.doi.org/10.1186/2190-8567-2-3>.
- [34] Roberts KL. Geometric singular perturbation theory and averaging: analysing torus canards in neural models. Australia: University of Sydney; 2018.
- [35] Dick OE. Mechanisms of dynamical complexity changes in patterns of sensory neurons under antinociceptive effect emergence. *Neurocomputing* 2020;378:120–8. <http://dx.doi.org/10.1016/j.neucom.2019.10.004>.
- [36] Slepukhina E, Bashkirtseva I, Ryashko L, Kügler P. Stochastic mixed-mode oscillations in the canards region of a cardiac action potential model. *Chaos Solitons Fractals* 2022;164:112640. <http://dx.doi.org/10.1016/j.chaos.2022.112640>.
- [37] Mi L, Wang C, Ren G, Ma J, Song X. Model of electrical activity in a neuron under magnetic flow effect. *Nonlinear Dynam* 2016;85:1479–90. <http://dx.doi.org/10.1007/s11071-016-2773-6>.
- [38] Zhang Y, Wu F, Wang C, Ma J. Stability of target waves in excitable media under electromagnetic induction and radiation. *Physica A* 2019;521:519–30. <http://dx.doi.org/10.1016/j.physa.2019.01.098>.
- [39] Baysal V, Yilmaz E. Effects of electromagnetic induction on vibrational resonance in single neurons and neuronal networks. *Physica A* 2020;537:122733. <http://dx.doi.org/10.1016/j.physa.2019.122733>.
- [40] Buschman TJ, Denovellis EL, Diogo C, Bullock D, Miller EK. Synchronous oscillatory neural ensembles for rules in the prefrontal cortex. *Neuron* 2012;76:838–46. <http://dx.doi.org/10.1016/j.neuron.2012.09.029>.
- [41] Bao BC, Liu Z, Xu JP. Steady periodic memristor oscillator with transient chaotic behaviours. *Electron Lett* 2010;46:237–8. <http://dx.doi.org/10.1049/el.2010.3114>.
- [42] Muthuswamy B. Implementing memristor based chaotic circuits. *Int J Bifurcation Chaos* 2010;20:1335–50. <http://dx.doi.org/10.1142/S0218127410026514>.
- [43] Dhooe A, Govaerts W, Kuznetsov YA. MATCONT: A MATLAB package for numerical bifurcation analysis of ODEs. *ACM Trans Math Software* 2003;29:141–64. <http://dx.doi.org/10.1145/779359.779362>.
- [44] Dhooe A, Govaerts W, Kuznetsov YA, Mestrom W, Riet AM, Sautois B. MATCONT and CL MATCONT: Continuation Toolboxes in MATLAB. Netherlands: Utrecht University; 2006.
- [45] Pavlidis E, Campillo F, Goldbeter A, Desroches M. Multiple-timescale dynamics, mixed mode oscillations and mixed affective states in a model of bipolar disorder. *Cogn. Neurodynamics* 2022. <http://dx.doi.org/10.1007/s11571-022-09900-4>.
- [46] Milik A, Szmolyan P. Multiple time scales and canards in a chemical oscillator, in multiple-time-scale dynamical systems. New York: Springer; 2001.
- [47] Rankin J, Desroches M, Lowenberg BK. Canard cycles in aircraft ground dynamics. *Nonlinear Dynam* 2011;66:681–8. <http://dx.doi.org/10.1007/s11071-010-9940-y>.
- [48] Chumakov GA, Chumakova NA. Relaxation oscillations in a kinetic model of catalytic hydrogen oxidation involving a chase on canards. *Chem Eng J* 2003;91:151–8. [http://dx.doi.org/10.1016/S1385-8947\(02\)00148-1](http://dx.doi.org/10.1016/S1385-8947(02)00148-1).

Original Research

Diffusion tensor imaging (DTI) Analysis Based on Tract-based spatial statistics (TBSS) and Classification Using Multi-Metric in Alzheimer's Disease

Yingteng Zhang¹, Feibiao Zhan^{2,*}

¹Department of Mathematics, Taizhou University, 225300 Taizhou, Jiangsu, China

²Department of Applied Mathematics, Nanjing Audit University, 211815 Nanjing, Jiangsu, China

*Correspondence: zhanfeibiao@yeah.net (Feibiao Zhan)

Academic Editor: Gernot Riedel

Submitted: 12 November 2022 Revised: 14 January 2023 Accepted: 17 January 2023 Published: 20 July 2023

Abstract

Background: Alzheimer's disease (AD) is a brain disorder characterized by atrophy of cerebral cortex and neurofibrillary tangles. Accurate identification of individuals at high risk of developing AD is key to early intervention. Combining neuroimaging markers derived from diffusion tensor images with machine learning techniques, unique anatomical patterns can be identified and further distinguished between AD and healthy control (HC). **Methods:** In this study, 37 AD patients (ADs) and 36 healthy controls (HCs) from the Alzheimer's Disease Neuroimaging Initiative were applied to tract-based spatial statistics (TBSS) analysis and multi-metric classification research. **Results:** The TBSS results showed that the corona radiata, corpus callosum and superior longitudinal fasciculus were the white matter fiber tracts which mainly suffered the severe damage in ADs. Using support vector machine recursive feature elimination (SVM-RFE) method, the classification performance received a decent improvement. In addition, the integration of fractional anisotropy (FA) + mean diffusivity (MD) + radial diffusivity (RD) into multi-metric could effectively separate ADs from HCs. The rank of significance of diffusion metrics was FA > axial diffusivity (DA) > MD > RD in our research. **Conclusions:** Our findings suggested that the TBSS and machine learning method could play a guidance role on clinical diagnosis.

Keywords: Alzheimer's disease; diffusion tensor imaging; diffusion metric; tract-based spatial statistics; support vector machine; classification

1. Introduction

Alzheimer's disease (AD) is associated with abnormal functioning of the nervous system and usually appears in people over the age of 60. Patients are often accompanied by memory loss and cognitive decline and other problems, which not only seriously harms the physical and mental health of patients, but also brings a heavy burden on families and society [1]. It is estimated that in 30 years there will be 134.6 million cases of AD worldwide [2]. However, the exact cause of AD is still unknown and existing targeted drugs can only reduce symptoms or delay its progression. Therefore, revealing the brain changes caused by the disease is crucial to explore the underlying cause of AD [3].

Precise diagnosis of AD helps patients improve future quality of life, including early prevention and optimal treatment [4]. With the fast development of artificial intelligence and medical imaging technology, computer-aided diagnosis provides sufficient evidence of accuracy to distinguish AD from healthy control (HC) [5–10]. Traditionally, AD has been thought of as a disease of gray matter (GM) damage, while the effects of white matter (WM) have generally been thought of as damage secondary to GM [11]. Although there is growing concern about WM damage in AD, our knowledge is still limited when compared

to GM atrophy and other biomarkers. In particular, a review illustrates different main research point of penetration for how WM injury leads to AD [12]. One piece of evidence is to study WM degeneration and demyelination as the important pathophysiological features of AD at the microstructural level [13,14]. Another piece of evidence comes from neuroimaging, which have the remarkable advantage of being able to noninvasively observe morphologic changes in patients' brains. Despite the study is focused on WM microstructures, it's important to highlight that diffusion tensor imaging (DTI) can be used to investigate even microstructural changes in GM (not only WM) [15,16]. With the development of DTI technology, it can be used to show the direction of fasciculus in the WM of the brain, which is the only non-invasive imaging method that can show the fasciculus *in vivo* [17].

There are some common metrics that can reflect the brain microstructure in DTI, such as fractional anisotropy (FA), mean diffusivity (MD), axial diffusivity (DA) and radial diffusivity (RD). FA represents the directivity of water molecular dispersion and can reflect the maximum possible arrangement direction of WM tracts. The FA value is higher in WM, close to 1, while it is close to 0 in cerebrospinal fluid. MD represents the overall dispersion of water molecules. DA represents the degree of dispersion



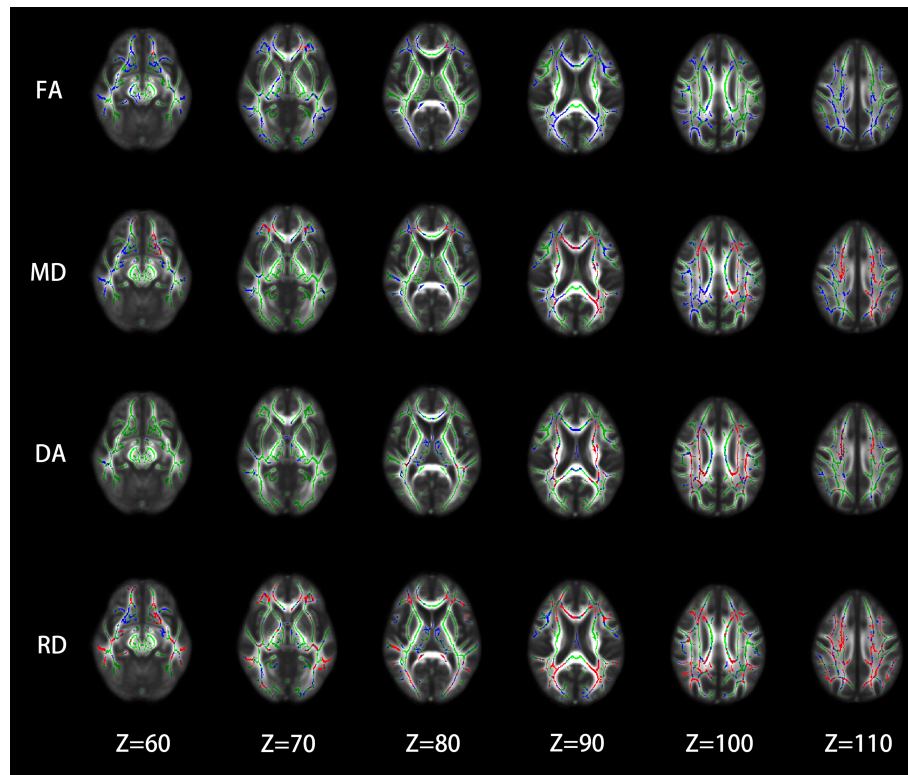


Fig. 1. The TBSS images of the DTI metrics (i.e., FA, MD, DA, RD) in horizontal slices of brain. Each column represents the different Z-axis value from $Z = 60$ to $Z = 110$. Significantly decreased FA and significantly increased MD, DA, RD in ADs versus HCs (Green: the skeleton, Blue: $p < 0.05$ with FWE corrected, red: $p < 0.01$ with FWE corrected). FA, fractional anisotropy; MD, mean diffusivity; DA, axial diffusivity; RD, radial diffusivity; TBSS, Tract-based spatial statistics; DTI, Diffusion tensor imaging; AD, Alzheimer's disease; HC, healthy control, FWE, family-wise error.

of water molecules along the main direction. RD represents the dispersion of water molecules in the other two directions [18,19]. For further understand the pathological mechanisms of WM tracts' change, tract-based spatial statistics (TBSS) method has been applied to research the microstructural of WM [20]. In recent years, machine learning-based neuroimaging technology for AD diagnosis and disease development has become a research hotspot [21–24]. As a widely used supervised learning method, support vector machine (SVM) shows good advantages in solving small sample, nonlinear and high-dimensional pattern recognition problems [25–28].

Here, we aimed to analyze research microstructural difference of WM and predict the accuracy between ADs and HCs. Therefore, the TBSS and SVM method will be used in our study. Specifically, we combined with different kind of DTI metric together for improving classification performance and rank the importance of the WM fiber tract.

2. Materials and Methods

2.1 Subjects

A total of 73 subjects from Alzheimer's Disease Neuroimaging Initiative Grand Opportunities/phase 2 (ADNI-GO/2) database (<http://adni.loni.usc.edu/>) [29] were col-

lected for this study. As everyone knows, the ADNI dataset has the multi-site nature which characterized by different scanners and acquisition protocols, can have an impact on DTI data such as noise and bias. However, harmonization methods already applied on ADNI DTI data in other studies [30,31] could fix this issue in the future. Before scanning, the subjects undergo cognitive and behavioral assessments. Statistical analysis of basic information in Table 1 is completed in SPSS 22.0 (IBM Corp., Armonk, NY, USA). The Table 1 display p -values and t -value for two sample t -tests for each sample characteristic except for gender, which displays p -values and chi square value from a Chi square test.

2.2 Image Acquisition

All subjects are scanned through a 3T GE MEDICAL SYSTEMS scanner (General Electric company, Boston, MA, USA). A whole brain diffusion MRI (dMRI) SE-EPI (spin-echo echo-planar imaging) is acquired with the following parameters: echo time (TE): 68.3 ms, repetition time (TR): 13,000 ms, Slice Thickness: 2.7 mm, Field Strength: 3.0, Flip Angle: 90 degree, 128 mm \times 128 mm matrix size, b-value: 1000 s/mm² (41 non-collinear directions) and 5 images with no diffusion weighting.

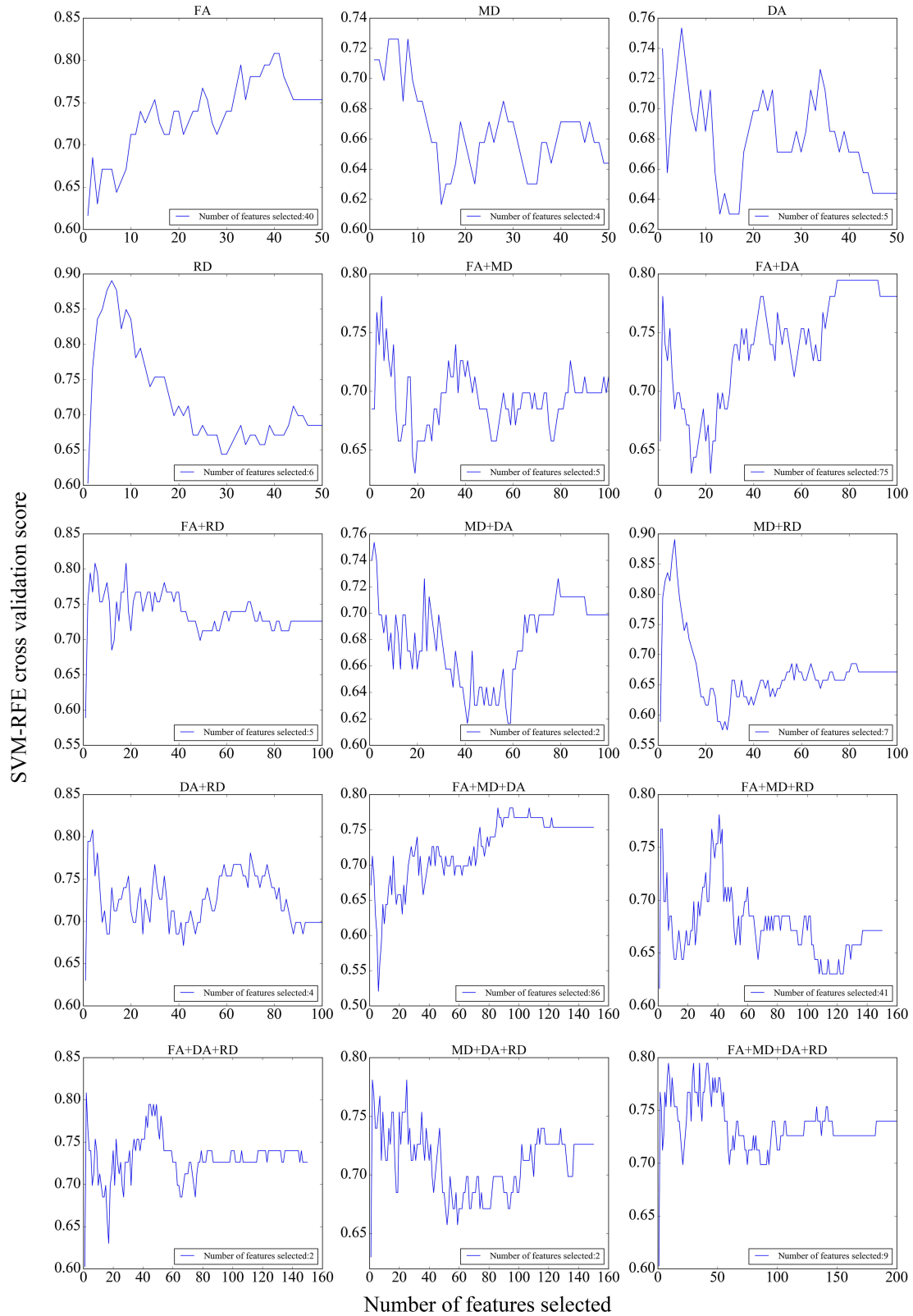


Fig. 2. Feature ranking with SVM-RFE and LOOCV selection of the best number of features. Each subgraph represented the cross validation score corresponding to the number of features selected for 15 kinds of single metric or multi-metric. The best feature dimensions are shown in a rectangular box at the bottom right of each subgraph for each kind of diffusion metrics. SVM-RFE, support vector machine recursive feature elimination; LOOCV, leave-one-out cross validation.

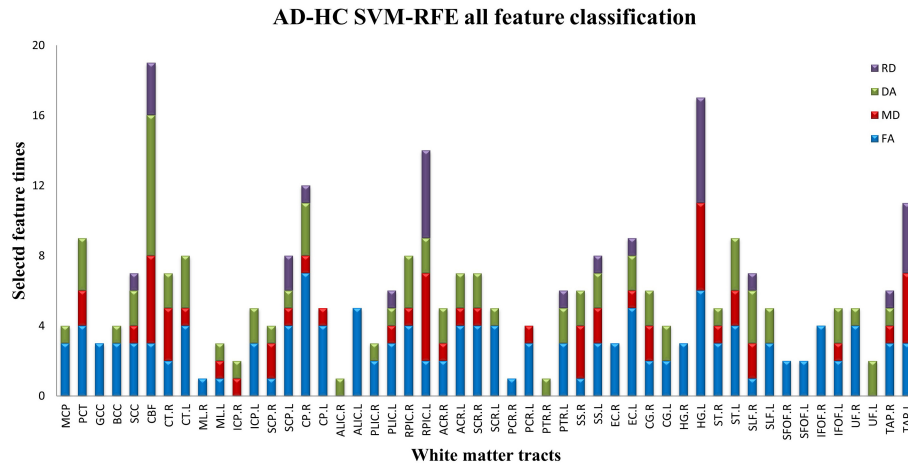


Fig. 3. The feature weighting distribution of WM tracts received by the summation of all combined approaches. WM, white matter.

Table 1. Demographic characteristics of the ADs and HCs.

	ADs (n = 37)	HCs (n = 36)	<i>p</i> -value	Chi2/ t-value
Gender (male:female)	25:12	19:17	0.197	1.667
Age (years)	74.81 ± 8.99	73.28 ± 6.19	0.398	0.85
MMSE	23.38 ± 1.98	28.81 ± 1.56	<0.001	-12.984
CDR	4.55 ± 1.43	0.03 ± 0.12	<0.001	19.153

Data is mean ± standard deviation. Columns on the right display *p*-values and t-value for two sample *t*-tests for each sample characteristic except for gender, which displays *p*-values and chi square value from a Chi square test. MMSE, Mini-Mental State Examination; CDR, Clinical Dementia Rating; AD, Alzheimer's disease; HC, healthy control.

2.3 Data Processing

Currently, PANDA (A Pipeline for Analysing Brain Diffusion Images) [32] is commonly used to process DTI data. PANDA software package is based on Linux operating system (Ubuntu 21.04, Canonical, London, UK) and Matlab software (MATLAB 9.7, MathWorks, Natick, MA, USA). In addition, PANDA's underlying commands invoke Functional magnetic resonance imaging of the brain (FMRIB) Software Library (FSL) tools [33], Diffusion Toolkit [34], Pipeline System for Octave and Matlab (PSOM) [35], and MRICron tools (<https://people.cas.sc.edu/rorden/mricron/install.html>). The preprocessing steps mainly include: (1) converting Digital Imaging and Communications in Medicine (DICOM) data to Neuroimaging Informatics Technology Initiative (NIFTI) format; (2) head movement and eddy current correction; (3) brain tissue was removed by Brain Extraction Tool (BET); (4) DTI metrics (i.e., FA, MD, DA, RD) calculation with non-linear fitting algorithm.

2.4 TBSS Analysis

The tract-based spatial statistics (TBSS) can fully reflect the microstructural changes of the whole brain WM and the skeletonized data processing method can obtain high accuracy without smoothing [20]. All subjects' FA maps were nonlinearly aligned to a $1 \times 1 \times 1$ mm standard space in Montreal Neurological Institute (MNI152) coordinates, using FSL FNIRT and FMRIB58_FA as template image. A template skeleton derived from the FMRIB58_FA (50 core regions are listed in Table 2 (Ref. [36])) was used for the analysis. This skeleton set a thresholds with 0.2 and individual FA data were projected into it for every subject. According to the standard TBSS workflow, data were entered into voxel-wise statistics to test for the group comparisons: HCs versus. ADs. The tool "randomize" was utilized by setting 5000 permutations and statistical threshold of $p < 0.05$ or $p < 0.01$. The threshold-free cluster enhancement (TFCE) was adopted as a correction for multiple comparisons. The result of comparison among groups of each parameter diagram overlaid on the FMRIB58_FA template via FSLEYES tool and used the WM tracts atlas carried by FSL for recognizing the discrepant area which had statistical significance. In addition, in order to visually view the discrepant condition of the same WM tract between groups, the TBSS mapping had converted to corresponding cluster size table via cluster locator tool in PANDA.

2.5 SVM Method and Analysis

The machine learning algorithm used in this study comes from Python's scikit-learn library [37]. The present application demonstrates that SVM was very good at mining information features [38]. Different type of SVM such as linear, non-linear with different kernel, SVM with recursive feature elimination (RFE) or regularization were applied to classify different disorders. In this paper, linear support vector machine recursive feature elimination (SVM-RFE) [39] was used to obtain the feature weight

Table 2. The rICBM-DTI-81 White Matter Parcellation Map (WMPM) FMRIB58 atlas.

rICBM-DTI-81 WMPM FMRIB58 atlas [36]			
Middle cerebellar peduncle	MCP	Pontine crossing tract	PCT
Splenium of corpus callosum	SCC	Column and body of fornix	CBF
Genu of corpus callosum	GCC	Body of corpus callosum	BCC
Medial lemniscus.R	ML.R	Medial lemniscus.L	ML.L
Corticospinal tract.R	CT.R	Corticospinal tract.L	CT.L
Superior cerebellar peduncle.R	SCP.R	Superior cerebellar peduncle.L	SCP.L
Inferior cerebellar peduncle.R	ICP.R	Inferior cerebellar peduncle.L	ICP.L
Cerebral peduncle.R	CPR	Cerebral peduncle.L	CP.L
Posterior limb of internal capsule.R	PLIC.R	Posterior limb of internal capsule.L	PLIC.L
Anterior limb of internal capsule.R	ALIC.R	Anterior limb of internal capsule.L	ALIC.L
Retrolenticular part of internal capsule.R	RPIC.R	Retrolenticular part of internal capsule.L	RPIC.L
Posterior thalamic radiation.R	PTR.R	Posterior thalamic radiation.L	PTR.L
Superior corona radiata.R	SCR.R	Superior corona radiata.L	SCR.L
Anterior corona radiata.R	ACR.R	Anterior corona radiata.L	ACR.R
Posterior corona radiata.R	PCR.R	Posterior corona radiata.L	PCR.L
External capsule.R	EC.R	External capsule.L	EC.L
Sagittal stratum.R	SS.R	Sagittal stratum.L	SS.L
Hippocampus gyrus.R	HG.R	Hippocampus gyrus.L	HG.L
Cingulate gyrus.R	CG.R	Cingulate gyrus.L	CG.L
Stria terminalis.R	ST.R	Stria terminalis.L	ST.L
Superior fronto-occipital fasciculus.R	SFOF.R	Superior fronto-occipital fasciculus.L	SFOF.L
Superior longitudinal fasciculus.R	SLF.R	Superior longitudinal fasciculus.L	SLF.L
Uncinate fasciculus.R	UFR	Uncinate fasciculus.L	UFL
Inferior fronto-occipital fasciculus.R	IFOF.R	Inferior fronto-occipital fasciculus.L	IFOF.L
Tapetum.R	TAP.R	Tapetum.L	TAP.L

ranking that could best distinguished ADs and HCs. The SVM-RFE method could gradually minimize superfluous and irrelevant features [40]. The SVM-RFE method eliminated useless features one by one during each recursive process and had been successfully applied to feature selection in several functional neuroimaging studies [41,42]. In addition, the leave-one-out cross validation (LOOCV) method was used for cross validation [43]. In this process, for each selected number of features, N classifications were made (where N corresponds to the number of subjects). The mean value of N classification accuracies was similar to the classification accuracy of corresponding feature numbers in the training data set.

The result of classification is the mean accuracy, sensitivity and specificity. Sensitivity is the percentage of samples that are actually positive that are judged to be positive. It is calculated as the ratio of true positive (TP) divided by true positive (TP) + false negative (FN) (actually positive but judged negative). Specificity refers to the proportion of samples that are actually negative that are judged to be negative. It is calculated as the ratio of true negative (TN) divided by true negative (TN) + false positive (FP) (actually negative but judged positive). Accuracy is expressed by the percentage of the total number of TP and TN in the number of subjects. For a more complete understanding of the classifier's performance, sensitivity, specificity, and

overall accuracy should be reported. Another very common method of reporting binary classifier results is to plot a receiver operating characteristic (ROC) curve [44]. ROC curve is a complete image of classifier performance provided by setting classification threshold value, in which, the horizontal coordinate represents false positive rate (FPR) (i.e., 1-specificity), and the vertical coordinate represents true positive rate (TPR), i.e., sensitivity. It is always desirable to have a numerical value to indicate whether a classifier is good or bad. The area under ROC curve (AUC) is the size of the area below the ROC curve. Typically, AUC values range from 0 to 1, with a larger AUC representing better performance. AUC is a standard used to measure the quality of a classification model [45].

3. Results

3.1 Statistical Analysis

There are no significant differences ($p > 0.05$) in age and sex between ADs and HCs (See Table 1 for group characteristics). It shows that ADs have a lower score of Mini-Mental State Examination (MMSE) but higher score of Clinical Dementia Rating (CDR) than HCs. The gender and age were regressed as covariables.

As shown in Fig. 1 and Table 3, compared with HC group, FA values of several WM regions in AD group de-

creased, and the WM fiber with the most significant difference was ACR.L (cluster number >100 , $p < 0.01$, FWE corrected).

Table 3. Difference of diffusion metrics of the WM tracts distribution in ADs versus HCs.

WM tracts	ADs versus HCs cluster size			
	FA	MD	DA	RD
GCC	967	993*	670	1072*
BCC	1507	2163*	1367*	2299*
SCC	2063	2155*	1553*	2428*
CBF	-	-	140	140
CP.R	299	-	-	189*
ALIC.L	-	151	175	-
PLIC.R	264	169	184*	136
PLIC.L	-	178	216*	-
RPIC.R	-	-	393*	-
RPIC.L	-	-	237*	-
ACR.R	958	1251*	520*	1328*
ACR.L	1095*	1329*	444*	1414*
SCR.R	475	1520*	1472*	1014*
SCR.L	234	1390*	1292*	681*
PCR.R	388	650	671*	539*
PCR.L	121	538*	608*	349*
PTR.R	721	186	167	673*
PTR.L	636	389*	197*	674*
SS.R	211	229	-	293*
SS.L	205	191	-	402*
EC.L	-	169	113	-
CG.R	296	199	-	288
CG.L	-	129	-	-
HG.R	175	-	-	175*
ST.R	176	-	-	178*
ST.L	199	-	-	193*
SLF.R	773	1460	1028*	1288*
SLF.L	472	1161*	974*	1012*
IFO.R	117	213	-	183
IFO.L	106	260*	-	255*

Note: The numerical value showed above represent the cluster number >100 , $p < 0.05$, FWE corrected. The numerical value marked with an asterisk (*) represent the cluster number >100 , $p < 0.01$, FWE corrected. WM, white matter; FA, fractional anisotropy; MD, mean diffusivity; DA, axial diffusivity; RD, radial diffusivity.

Similarly, compared with HC group, MD values of several WM regions in AD group increased, and the WM fiber with the most significant difference were GCC, BCC, SCC, bilateral ACR, bilateral SCR, PCR.L, PTR.L, SLF.L, IFOF.L (cluster number >100 , $p < 0.01$, FWE corrected).

Similarly, compared with HC group, DA values of several WM regions in AD group increased, and the WM fiber with the most significant difference were BCC, SCC, bilateral PLIC, bilateral RPIC, bilateral ACR, bilateral

SCR, bilateral PCR, PTR.L, bilateral SLF (cluster number >100 , $p < 0.01$, FWE corrected).

Similarly, compared with HC group, RD values of several WM regions in AD group increased, and the WM fiber with the most significant difference were GCC, BCC, SCC, CP.R, bilateral ACR, bilateral SCR, bilateral PCR, bilateral PTR, bilateral SS, HG.R, bilateral ST, bilateral SLF, IFOF.L (cluster number >100 , $p < 0.01$, FWE corrected).

3.2 Feature Selection and Classification Accuracy

The best number of features of 15 kinds of single metric or multi-metric had been drawn in the corresponding rectangular frame through the SVM-RFE and LOOCV. The X-axis value corresponding to the curve peak value was the best feature dimension.

Combined with Fig. 2 and Table 4, it could be found that FA+MD+RD received the highest accuracy which increased from 67.12% to 100% among all kinds of DTI metrics while its optimal feature dimension was not the minimum. Through SVM-RFE approach, the accuracy, sensitivity and specificity of classification received some measure of improvement. For some kinds of multi-metric, the penalty factors had been adjusted which marked with an asterisk in order to improve the classifying quality.

In order to investigate the weight distribution of different WM tract and the percent of different DTI metric on each WM tract, Fig. 3 was computed to depict the WM tract for which could classify the ADs from HCs.

These ROC curves in Fig. 4 showed the classifier performance of different kind of DTI metric combined approach, computed from 5-fold cross-validation. Taking all of these curves, it was possible to calculate the AUC, and intuitively find the improvement of the classifier output performance. From above it could be found that the ROC curve which computed from FA+MD+RD received a high classifier output quality since it had a perfect AUC.

4. Discussion

In our study, two aspects were mainly researched: statistical analysis of DTI data and classification. The subjects were firstly preprocessed using PANDA tool. Then the statistical analysis was operated by TBSS and classification process was conducted by SVM method.

Relevant literatures showed that the association fiber and limbic system were the most reported abnormal regions in the WM tracts of AD [46–48]. Cingulate was the association fiber between cingulate gyrus and other brain structures. Its integrity might directly relate to the emotion and cognitive function in AD patients. In our study, FA value of the right cingulate gyrus in ADs obviously decreased compared to HCs that was agreed with previous researches [49,50]. In addition, association fiber contacted with part cortex of the ipsilateral hemisphere, FA value of bilateral sagittal stratum, superior fronto-occipital fasciculus and superior longitudinal fasciculus in ADs decreased

Table 4. Classification accuracy, sensitivity and specificity of multiple diffusion metrics.

Diffusion metrics	Optimal feature dimensions	Accuracy/%		Sensitivity/%		Specificity/%	
		Before	After	Before	After	Before	After
FA	40	75.34	89.04	75.68	89.19	75.00	88.89
MD	4	64.38	79.45	65.71	78.95	63.16	80.00
DA	5	64.38	82.19	65.71	83.33	63.16	81.08
RD	6	68.49	91.78	66.67	91.89	70.97	91.67
FA + MD	5	71.23	86.30*	72.22	90.91*	70.27	82.5*
FA + DA	75	78.08	90.41	78.38	94.12	77.78	87.18
FA + RD	5	72.60	89.04	71.79	89.19	73.53	88.89
MD + DA	2	69.86	79.45	71.43	82.35	68.42	76.92
MD + RD	7	67.12	93.15	66.67	94.44	67.65	91.89
DA + RD	4	69.86	87.67	71.43	88.89	68.42	86.49
FA + MD + DA	86	75.34	93.15	77.14	97.06	73.68	89.74
FA + MD + RD	41	67.12	100	66.67	100	67.65	100
FA + DA + RD	2	72.60	83.56*	74.29	87.88*	71.05	80*
MD + DA + RD	2	72.60	79.45	75.76	82.35	70.00	76.92
FA + MD + DA + RD	9	73.97	91.78*	76.47	97.06*	71.79	87.5*

The numerical value marked with an asterisk (*) represent a parameter optimization: FA + MD: C = 0.1; FA + DA + RD: C = 0.02; FA + MD + DA + RD: C = 0.1. The default C value is 1 and C represent penalty factor.

compared with HCs that was agreed with Teipel's research [51]. Correlational study found superior fronto-occipital fasciculus influenced visual spatial processing and memory function [52]. The damage of superior longitudinal fasciculus might involve spatial working memory and linguistic function [53]. The decrease of these functions was reflected on ADs than related to our research results. Optic radiation was the central neurons of visual pathway so that its lesion would lead to defect of field vision. In our study, decrease of FA value of posterior thalamic radiation in ADs hinted the damage of visual performance [54]. Wang *et al.* [55] based on TBSS with multi-parameter found that bilateral hippocampus gyrus existed obvious abnormal in ADs and patients with mild cognitive impairment (MCIs), including the decrease of FA value and increase of RD value, especially the right hemisphere in which was most significant. While our study found the difference just exists in the right hippocampus gyrus. MD value increased when the tissue damage. Increased MD and decreased FA were found in the corpus callosum that was agreed with previous research [56]. The corpus callosum was a bundle of fibers connecting the right and left hemispheres of the brain. On the basis of previous researches, the anterior part of the corpus callosum was connected to the prefrontal cortex and was associated with the sense of motivation [57].

Therefore, our results suggested that communication disorders between brain structures might be related to apathy symptoms of ADs [58,59]. Moreover, the particular pattern of association between severity of apathy and corpus callosum integrity might reflect slower initiation and longer response times for tasks involving hemispheric metastasis or interregional integration in apathetic ADs. Previous results had demonstrated increased MD in most lobar regions

of ADs, including frontal lobes [56], temporal lobes [56], parietal lobes [60], and occipital lobe [60]. DA and RD also increased in addition to FA and MD. However, the relevant research for DA and RD was little. Our findings suggested that DA and RD might be a useful biomarker in identifying HCs and ADs.

After the SVM-RFE method, each kind of DTI metric received the optimal feature dimensions that listed in Table 4. Obviously, the majority of diffusion metrics received optimal effect after dimensionality reduction. In addition, the accuracy, sensitivity and specificity of each kind of diffusion metrics were improved via the SVM-RFE method. Several kinds of multi-metrics were further improved by adjusting the penalty factor C value. Table 4 showed that the FA+MD+RD metric received the best classification accuracy. For further investigated the effect of feature weighting on classification performance, Fig. 3 had been drawn to show the feature weighting distribution of WM tracts by the summation of all combined approaches. The feature weighting of CBF, HG.L and RPIC.L exceed 0.6 while that of ML.R, ALIC.R and PCR.R almost zero. It was also found that the rank of significance of diffusion metrics was FA > DA > MD > RD. In order to visually evaluate classifier output quality, The ROC curve and AUC were depicted from before and after the dimension reduction. Fig. 4 showed that the AUC increased after the SVM-RFE method. The results ulteriorly verified the effectiveness of the dimension reduction.

5. Conclusions

In this paper, we introduced multi-metrics measures to identify the difference between HCs and ADs based on TBSS method. The corona radiata, corpus callosum and

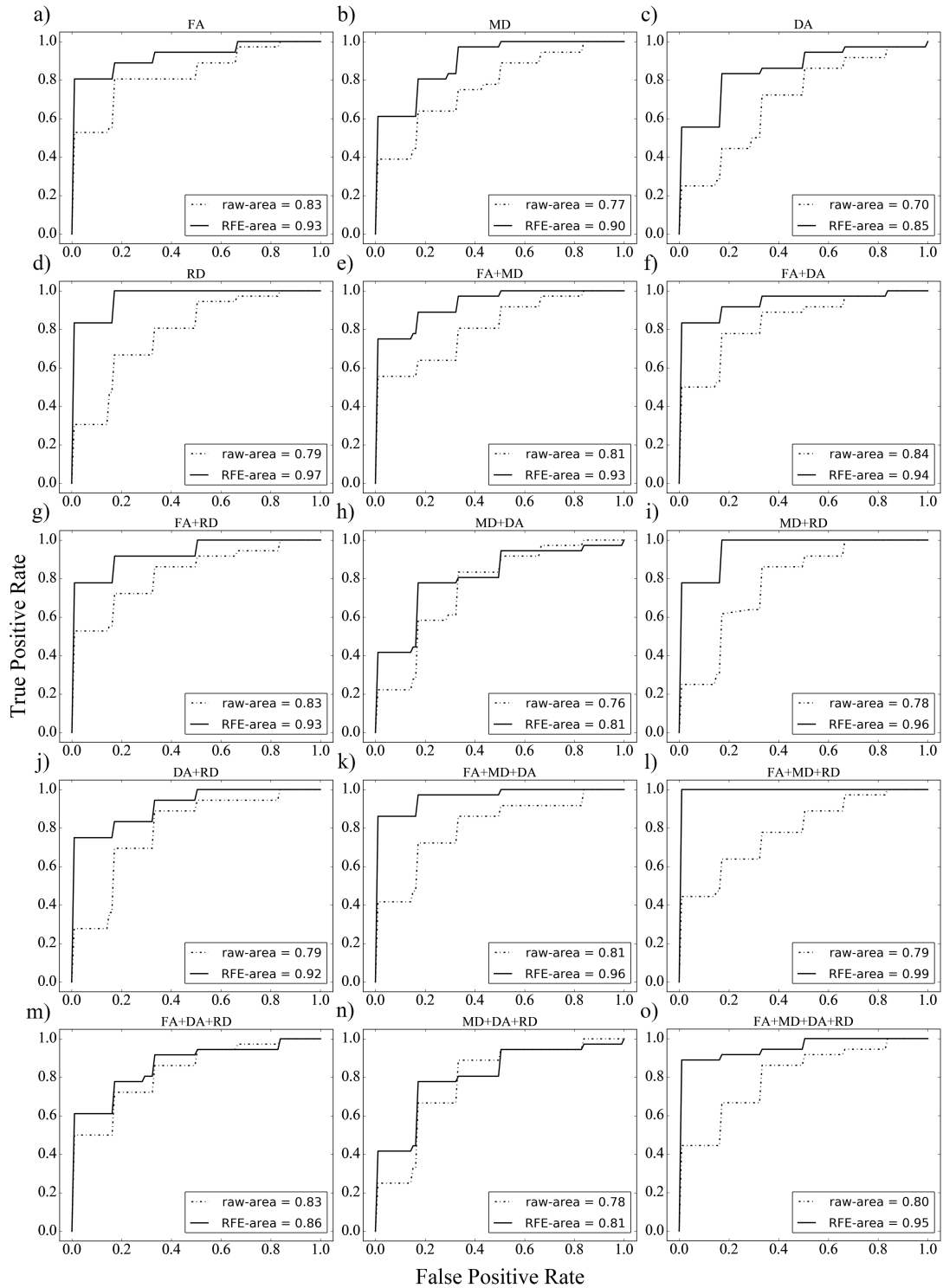


Fig. 4. Different DTI metric of ROC curve to evaluate classifier performance by 5-fold cross-validation. The ROC curve with dotted line represented the AUC before SVM-RFE and the ROC curve with solid line represented the AUC after SVM-RFE. (a–o) represented the ROC curve and AUC for 15 kinds of DTI metric through combined approach, respectively. ROC, receiver operating characteristic; AUC, area under curve.

superior longitudinal fasciculus were the WM fiber tracts which mainly suffered the severe damage in ADs. Inter-group classification was completed by SVM-RFE method. Multi-metrics combination would improve the classifica-

tion performance compared with single diffusion metric. We also depicted the feature weighting distribution of WM tracts for each kind of DTI metric in order to research which WM fiber tract played an important role on classification.

In addition, the ROC curve and AUC could evaluate classifier output quality for each kind of diffusion metric.

There were several limitations to this research. First, small sample size would affect the reliability of classification results. Although our research used SVM model to distinguish AD group from HC group, it needed to be further verified on a larger sample to reinforce the current results and ensured that it had strong generalization ability. Deep learning could be combined if necessary. Another limitation was that the MCI group was absent from this study. MCI was known as a transition stage from health status to AD. It was necessary to include MCI in future studies to understand which features develop gradually over the course of the disease evolution and to reveal the degenerative pattern of the pathological mechanism of AD.

Availability of Data and Materials

The datasets generated and/or analyzed during the current study are available in the ADNI repository, <http://adni.loni.usc.edu/>.

Author Contributions

FZ designed the research study. YZ performed the research, analyzed the data and revised the manuscript. YZ and FZ wrote the manuscript. Both authors contributed to editorial changes in the manuscript. Both authors read and approved the final manuscript. Both authors have participated sufficiently in the work and agreed to be accountable for all aspects of the work.

Ethics Approval and Consent to Participate

The dataset we used was the public dataset of ADNI, the ethical approval was not required. In addition, informed written consent was obtained from all participants at every center.

Acknowledgment

We thank two anonymous reviewers for excellent criticism of the article.

Funding

This work was supported by the National Natural Science Foundation of China (Grant No.12202208), the Basic Science (Natural Science) Research Project of Colleges and Universities of Jiangsu Province (Grant No.22KJB310019, Grant No.22KJB130009), the Scientific Research Foundation of high-level personnel of Taizhou University (Grant No.TZXY2021QDJJ001), the Research and Cultivation Project for Young Teachers of Nanjing Audit University (Grant No.2021QNPY015), 2022 Double-Innovation Doctor of Jiangsu Province, “2022 Taizhou Tuo Ju Project” for Young science and Technology Talents, the Project of Excellent Science and Technology Innovation Team of Taizhou University.

Conflict of Interest

The authors declare no conflict of interest.

References

- [1] Tiwari S, Atluri V, Kaushik A, Yndart A, Nair M. Alzheimer's disease: pathogenesis, diagnostics, and therapeutics. *International Journal of Nanomedicine*. 2019; 14: 5541–5554.
- [2] Ferri CP, Prince M, Brayne C, Brodaty H, Fratiglioni L, Ganguli M, *et al.* Global prevalence of dementia: a Delphi consensus study. *Lancet*. 2005; 366: 2112–2117.
- [3] 2020 Alzheimer's disease facts and figures. *Alzheimer's & Dementia*. 2020; 16: 391–460.
- [4] Guzman-Martinez L, Calfio C, Farias GA, Vilches C, Prieto R, Maccioni RB. New Frontiers in the Prevention, Diagnosis, and Treatment of Alzheimer's Disease. *Journal of Alzheimer's Disease*. 2021; 82: S51–S63.
- [5] Wang Z, Tang Z, Zhu Y, Pettigrew C, Soldan A, Gross A, *et al.* AD risk score for the early phases of disease based on unsupervised machine learning. *Alzheimer's & Dementia*. 2020; 16: 1524–1533.
- [6] Pellegrini E, Ballerini L, Hernandez MDCV, Chappell FM, González-Castro V, Anblagan D, *et al.* Machine learning of neuroimaging for assisted diagnosis of cognitive impairment and dementia: A systematic review. *Alzheimer's & Dementia*. 2018; 10: 519–535.
- [7] Zhutovsky P, Vijverberg EGB, Bruin WB, Thomas RM, Wattjes MP, Pijnenburg YAL, *et al.* Individual Prediction of Behavioral Variant Frontotemporal Dementia Development Using Multivariate Pattern Analysis of Magnetic Resonance Imaging Data. *Journal of Alzheimer's Disease*. 2019; 68: 1229–1241.
- [8] Weiner MW, Veitch DP, Aisen PS, Beckett LA, Cairns NJ, Green RC, *et al.* Recent publications from the Alzheimer's Disease Neuroimaging Initiative: Reviewing progress toward improved AD clinical trials. *Alzheimer's & Dementia*. 2017; 13: e1–e85.
- [9] Katabathula S, Wang Q, Xu R. Predict Alzheimer's disease using hippocampus MRI data: a lightweight 3D deep convolutional network model with visual and global shape representations. *Alzheimer's Research & Therapy*. 2021; 13: 104.
- [10] Yan T, Wang Y, Weng Z, Du W, Liu T, Chen D, *et al.* Early-Stage Identification and Pathological Development of Alzheimer's Disease Using Multimodal MRI. *Journal of Alzheimer's Disease*. 2019; 68: 1013–1027.
- [11] Roher AE, Weiss N, Kokjohn TA, Kuo Y, Kalback W, Anthony J, *et al.* Increased A beta peptides and reduced cholesterol and myelin proteins characterize white matter degeneration in Alzheimer's disease. *Biochemistry*. 2002; 41: 11080–11090.
- [12] Amlen IK, Fjell AM. Diffusion tensor imaging of white matter degeneration in Alzheimer's disease and mild cognitive impairment. *Neuroscience*. 2014; 276: 206–215.
- [13] Sjöbeck M, Haglund M, Englund E. White matter mapping in Alzheimer's disease: A neuropathological study. *Neurobiology of Aging*. 2006; 27: 673–680.
- [14] Nasrabady SE, Rizvi B, Goldman JE, Brickman AM. White matter changes in Alzheimer's disease: a focus on myelin and oligodendrocytes. *Acta Neuropathologica Communications*. 2018; 6: 22.
- [15] Parker TD, Slattery CF, Zhang J, Nicholas JM, Paterson RW, Foulkes AJM, *et al.* Cortical microstructure in young onset Alzheimer's disease using neurite orientation dispersion and density imaging. *Human Brain Mapping*. 2018; 39: 3005–3017.
- [16] Torso M, Bozzali M, Zamboni G, Jenkinson M, Chance SA. Detection of Alzheimer's Disease using cortical diffusion tensor imaging. *Human Brain Mapping*. 2021; 42: 967–977.

- [17] Le Bihan D, Mangin JF, Poupon C, Clark CA, Pappata S, Molko N, *et al.* Diffusion tensor imaging: concepts and applications. *Journal of Magnetic Resonance Imaging*. 2001; 13: 534–546.
- [18] Bassler PJ, Pierpaoli C. Microstructural and physiological features of tissues elucidated by quantitative-diffusion-tensor MRI. *Journal of Magnetic Resonance*. 2011; 213: 560–570.
- [19] Bassler PJ, Pierpaoli C. A simplified method to measure the diffusion tensor from seven MR images. *Magnetic Resonance in Medicine*. 1998; 39: 928–934.
- [20] Smith SM, Jenkinson M, Johansen-Berg H, Rueckert D, Nichols TE, Mackay CE, *et al.* Tract-based spatial statistics: voxelwise analysis of multi-subject diffusion data. *NeuroImage*. 2006; 31: 1487–1505.
- [21] Sheng J, Shao M, Zhang Q, Zhou R, Wang L, Xin Y. Alzheimer's disease, mild cognitive impairment, and normal aging distinguished by multi-modal parcellation and machine learning. *Scientific Reports*. 2020; 10: 5475.
- [22] Ezzati A, Zammit AR, Harvey DJ, Habeck C, Hall CB, Lipton RB, *et al.* Optimizing Machine Learning Methods to Improve Predictive Models of Alzheimer's Disease. *Journal of Alzheimer's Disease*. 2019; 71: 1027–1036.
- [23] Rohini M, Surendran D. Toward Alzheimer's disease classification through machine learning. *Soft Computing*. 2020; 25: 2589–2597.
- [24] Lee JS, Kim C, Shin J, Cho H, Shin D, Kim N, *et al.* Machine Learning-based Individual Assessment of Cortical Atrophy Pattern in Alzheimer's Disease Spectrum: Development of the Classifier and Longitudinal Evaluation. *Scientific Reports*. 2018; 8: 4161.
- [25] Cui Z, Xia Z, Su M, Shu H, Gong G. Disrupted white matter connectivity underlying developmental dyslexia: A machine learning approach. *Human Brain Mapping*. 2016; 37: 1443–1458.
- [26] Dyrba M, Grothe M, Kirste T, Teipel SJ. Multimodal analysis of functional and structural disconnection in Alzheimer's disease using multiple kernel SVM. *Human Brain Mapping*. 2015; 36: 2118–2131.
- [27] Oliveira PPD, Nitrini R, Busatto G, Buchpiguel C, Sato JR, Amaro E. Use of SVM methods with surface-based cortical and volumetric subcortical measurements to detect Alzheimer's disease. *Journal of Alzheimer's Disease*. 2010; 19: 1263–1272.
- [28] Yang B, Chen J, Chou W, Huang WS, Fuh JL, Liu RS, *et al.* Classification of Alzheimer's Disease from 18F-FDG and 11C-PiB PET Imaging Biomarkers Using Support Vector Machine. *Journal of Medical and Biological Engineering*. 2020; 40: 545–554.
- [29] Veitch DP, Weiner MW, Aisen PS, Beckett LA, Cairns NJ, Green RC, *et al.* Understanding disease progression and improving Alzheimer's disease clinical trials: Recent highlights from the Alzheimer's Disease Neuroimaging Initiative. *Alzheimer's & Dementia*. 2019; 15: 106–152.
- [30] Torso M, Ridgway GR, Hardingham I, Schwarz AJ, Chance SA. In Vivo Detection of Changes Related to Cortical Columnar Organization and Neuroinflammation Across the AD Continuum. *The Journal of Prevention of Alzheimer's Disease*. 2022; 9: 769–779.
- [31] Beer JC, Tustison NJ, Cook PA, Davatzikos C, Sheline YI, Shinohara RT, *et al.* Longitudinal ComBat: A method for harmonizing longitudinal multi-scanner imaging data. *NeuroImage*. 2020; 220: 117129.
- [32] Cui Z, Zhong S, Xu P, He Y, Gong G. PANDA: a pipeline toolbox for analyzing brain diffusion images. *Frontiers in Human Neuroscience*. 2013; 7: 42.
- [33] Smith SM, Jenkinson M, Woolrich MW, Beckmann CF, Behrens TEJ, Johansen-Berg H, *et al.* Advances in functional and structural MR image analysis and implementation as FSL. *NeuroImage*. 2004; 23: S208–S219.
- [34] Wang R, Benner T, Sorensen AG, Wedeen VJ. Diffusion Toolkit: A Software Package for Diffusion Imaging Data Processing and Tractography. *Proc Intl Soc Mag Reson Med*. 2007; 15: 3720.
- [35] Bellec P, Lavoie-Courchesne S, Dickinson P, Lerch JP, Zijdenbos AP, Evans AC. The pipeline system for Octave and Matlab (PSOM): a lightweight scripting framework and execution engine for scientific workflows. *Frontiers in Neuroinformatics*. 2012; 6: 7.
- [36] Mori S, Oishi K, Jiang H, Jiang L, Li X, Akhter K, *et al.* Stereotaxic white matter atlas based on diffusion tensor imaging in an ICBM template. *NeuroImage*. 2008; 40: 570–582.
- [37] Abraham A, Pedregosa F, Eickenberg M, Gervais P, Mueller A, Kossaifi J, *et al.* Machine learning for neuroimaging with scikit-learn. *Frontiers in Neuroinformatics*. 2014; 8: 14.
- [38] Furey TS, Cristianini N, Duffy N, Bednarski DW, Schummer M, Haussler D. Support vector machine classification and validation of cancer tissue samples using microarray expression data. *Bioinformatics*. 2000; 16: 906–914.
- [39] Guyon I, Weston J, Barnhill S, Vapnik V. Gene Selection for Cancer Classification using Support Vector Machines. *Machine Learning*. 2002; 46: 34.
- [40] Duan K, Rajapakse JC, Wang H, Azuaje F. Multiple SVM-RFE for gene selection in cancer classification with expression data. *IEEE Transactions on Nanobioscience*. 2005; 4: 228–234.
- [41] Craddock RC, Holtzheimer PE, Hu XP, Mayberg HS. Disease state prediction from resting state functional connectivity. *Magnetic Resonance in Medicine*. 2009; 62: 1619–1628.
- [42] De Martino F, Valente G, Staeren N, Ashburner J, Goebel R, Formisano E. Combining multivariate voxel selection and support vector machines for mapping and classification of fMRI spatial patterns. *NeuroImage*. 2008; 43: 44–58.
- [43] Zhao M, Zhao C, Zheng C. Identifying Concealed Information Using Wavelet Feature Extraction and Support Vector Machine. *Procedia Environmental Sciences*. 2011; 8: 337–343.
- [44] Zweig MH, Campbell G. Receiver-operating characteristic (ROC) plots: a fundamental evaluation tool in clinical medicine. *Clinical Chemistry*. 1993; 39: 561–577.
- [45] Fawcett T. An introduction to ROC analysis. *Pattern Recognition Letters*. 2006; 27: 861–874.
- [46] Xie S, Xiao JX, Gong GL, Zang YF, Wang YH, Wu HK, *et al.* Voxel-based detection of white matter abnormalities in mild Alzheimer disease. *Neurology*. 2006; 66: 1845–1849.
- [47] Huang H, Fan X, Weiner M, Martin-Cook K, Xiao G, Davis J, *et al.* Distinctive disruption patterns of white matter tracts in Alzheimer's disease with full diffusion tensor characterization. *Neurobiology of Aging*. 2012; 33: 2029–2045.
- [48] Agosta F, Pievani M, Sala S, Geroldi C, Galluzzi S, Frisoni GB, *et al.* White matter damage in Alzheimer disease and its relationship to gray matter atrophy. *Radiology*. 2011; 258: 853–863.
- [49] Takahashi S, Yonezawa H, Takahashi J, Kudo M, Inoue T, Tohgi H. Selective reduction of diffusion anisotropy in white matter of Alzheimer disease brains measured by 3.0 Tesla magnetic resonance imaging. *Neuroscience Letters*. 2002; 332: 45–48.
- [50] Stenset V, Bjørnerud A, Fjell AM, Walhovd KB, Hofoss D, Due-Tønnessen P, *et al.* Cingulum fiber diffusivity and CSF T-tau in patients with subjective and mild cognitive impairment. *Neurobiology of Aging*. 2011; 32: 581–589.
- [51] Teipel SJ, Grothe MJ, Filippi M, Fellgiebel A, Dyrba M, Frisoni GB, *et al.* Fractional anisotropy changes in Alzheimer's disease depend on the underlying fiber tract architecture: a multiparametric DTI study using joint independent component analysis. *Journal of Alzheimer's Disease*. 2014; 41: 69–83.
- [52] Catani M, Jones DK, Donato R, Ffytche DH. Occipito-temporal connections in the human brain. *Brain*. 2003; 126: 2093–2107.
- [53] Mesulam MM. A cortical network for directed attention and unilateral neglect. *Annals of Neurology*. 1981; 10: 309–325.

- [54] Rizzo M, Anderson SW, Dawson J, Nawrot M. Vision and cognition in Alzheimer's disease. *Neuropsychologia*. 2000; 38: 1157–1169.
- [55] Wang Y, West JD, Flashman LA, Wishart HA, Santulli RB, Rabin LA, *et al*. Selective changes in white matter integrity in MCI and older adults with cognitive complaints. *Biochimica Et Biophysica Acta*. 2012; 1822: 423–430.
- [56] Bozzali M, Falini A, Franceschi M, Cercignani M, Zuffi M, Scotti G, *et al*. White matter damage in Alzheimer's disease assessed in vivo using diffusion tensor magnetic resonance imaging. *Journal of Neurology, Neurosurgery, and Psychiatry*. 2002; 72: 742–746.
- [57] Clark DL, Boutros NN, Mendez MF. The brain and behavior: an introduction to behavioral neuroanatomy. *Journal of Neuropsychiatry*. 2001; 13: 525–526.
- [58] Hahn C, Lim H, Won WY, Ahn KJ, Jung W, Lee CU. Apathy and white matter integrity in Alzheimer's disease: a whole brain analysis with tract-based spatial statistics. *PLoS ONE*. 2013; 8: e53493.
- [59] Torso M, Serra L, Giulietti G, Spanò B, Tuzzi E, Koch G, *et al*. Strategic lesions in the anterior thalamic radiation and apathy in early Alzheimer's disease. *PLoS ONE*. 2015; 10: e0124998.
- [60] Head D, Buckner RL, Shimony JS, Williams LE, Akbudak E, Conturo TE, *et al*. Differential vulnerability of anterior white matter in nondemented aging with minimal acceleration in dementia of the Alzheimer type: evidence from diffusion tensor imaging. *Cerebral Cortex*. 2004; 14: 410–423.



Research article

The influence of synaptic strength and noise on the robustness of central pattern generator

Feibiao Zhan¹, Jian Song^{2,3,*} and Shenquan Liu²

¹ School of Mathematics, Nanjing Audit University, Nanjing 211815, China

² School of Mathematics, South China University of Technology, Guangzhou 510640, China

³ School of Mathematical and Computational Sciences, Massey University, Auckland 4442, New Zealand

* **Correspondence:** Email: masongj_vlp@mail.scut.edu.cn.

Abstract: In this paper, we explore the mechanisms of central pattern generators (CPGs), circuits that can generate rhythmic patterns of motor activity without external input. We study the half-center oscillator, a simple form of CPG circuit consisting of neurons connected by reciprocally inhibitory synapses. We examine the role of asymmetric coupling factors in shaping rhythm activity and how different network topologies contribute to network efficiency. We have discovered that neurons with lower synaptic strength are more susceptible to noise that affects rhythm changes. Our research highlights the importance of asymmetric coupling factors, noise, and other synaptic parameters in shaping the broad regimes of CPG rhythm. Finally, we compare three topology types' regular regimes and provide insights on how to locate the rhythm activity.

Keywords: rhythm activity; topology; noise; robustness; central pattern generator

1. Introduction

Central pattern generator (CPG) is a microcircuit of neuron network that can generate multi-rhythm pattern sequences spontaneously without any external information input [1,2]. It controls motor behaviors such as swimming [3,4], walking, breathing, heartbeat, and more [2,5–7]. Recently, Marder et al. made a well-summarized study about CPG and put forward new insights on small rhythmic circuits [8]. CPG is characterized by the robustness and flexibility of the neuronal network in rhythmic activity.

There have been numerous studies examining the working mechanisms of CPGs from both theoretical and experimental perspectives [9–16]. However, achieving flexibility and robustness in CPGs remains not fully understood. Coordination of motor rhythms can be better achieved through the

connection between CPGs, which may form an attractor. Each attractor determines a rhythmic behavior [17, 18]. Some researchers have proposed a rhythmic pattern for human arm movement, indicating that humans also possess a higher level of CPG in their central nervous system. Research on the reasons for these characteristics of CPGs is still ongoing, and it remains unclear how CPGs achieve the robustness and flexibility required for the collaborative implementation of essential rhythm patterns [19]. Thus, discussion on the rhythmic activity pattern of CPGs is still active [20, 21]. Some models are based on Hodgkin-Huxley (HH) neurons, while others are non-periodic neural oscillation models. Theoretical researchers have revealed the hidden internal mechanisms of CPGs from the perspective of dynamics [13, 22]. Collens et al. have revealed a mutually inhibitory tri-neuron neural network that explains the emergence, disappearance, and stability of neuronal rhythm with the change of synaptic parameters [22]. Lu et al. [23, 24] have studied the synchronization and resonance of small-world networks based on CPGs and proposed integer and fractional models based on the working mechanisms of CPGs. Recent research by Zang and Marder in PNAS (2023) demonstrates that how the spatial morphology of neurons can significantly impact the firing patterns of the CPG circuit [25]. The firing mechanism of neuronal rhythm is known to vary according to several studies [26–28]. However, it is still unclear whether this diversity in neuronal rhythm implies a diversity of CPG circuit function. A crucial question is whether the same CPG circuit can produce multiple motor behaviors, making it multifunctional [29, 30]. The generation of motor behavior depends on the modulation of a variety of motor rhythms, making it necessary and important to study rhythm diversity in order to understand the function of CPG.

Studying small circuits is crucial to understanding CPG. Typically, these circuits are half-center oscillators (HCO), the smallest building unit that consists of groups of neurons that inhibit each other [31, 32]. HCO circuits are considered the easiest to identify. The firing patterns of HCOs may also be influenced by neuronal phase response curves, as indicated in the work by Zang et al. [33]. The synchronization of two neurons has been explored by researchers [34, 35]. They have analyzed how neuronal parameters affect the network activity of HCO, which in turn affects motor control [36]. Researchers have also analyzed the effect of changes in system parameter space on the robustness of the HCO bursting model [37, 38]. Noise, the robustness of HCO, and sensory feedback are closely related [39, 40]. However, the effect of synaptic conductance on HCO rhythm patterns still needs to be analyzed. Inhibition of connection can improve the stability of CPG, and we will explore how changes in the rhythm pattern of HCO and tri-neuron CPG occur with the system parameter regime. We will also examine the effects of synaptic conductance and noise on CPG rhythm patterns.

In this study, we investigate the origin of the flexibility and robustness of CPGs as well as the impact of synaptic conductance on the network rhythm. We examine three different topological modes where each neuron has at least one connection to the other member of the CPG. Our findings demonstrate that diverse rhythm patterns exist in Patterns B and C, as shown in Figure 3. These results are based on the functional characteristics of CPG network structures, which are classified as “open” and “non-open” and were studied by Huerta et al. These findings are also consistent with certain biological principles [41]. Rhythmic motor patterns are associated with diseases such as spinal cord injury and can be easily studied quantitatively. Therefore, the study of CPG rhythm can significantly contribute to the development of disease diagnosis and the advancement of intelligent science. For example, Mader et al. (2001) elaborated that CPG can contribute to the development of new therapeutic methods in the recovery of spinal cord injury and summarized the mechanism process of CPG [1]. The biological

CPG principle and the establishment of spiking neural network [42–45] inspire the development of intelligent science.

The paper is structured as follows. In Section 2, we describe the materials and methods we used in building CPG, including the HH neuron model. Then, in Section 3.1, we illustrate how the rhythm pattern of HCO is regulated by synaptic strength and noise. In Section 3.2, we investigate CPG rhythms in other topologies. Finally, we present the discussion and conclusion in Section 4.

2. Materials and methods

2.1. Neuronal model and dynamics

In our CPG, each interneuron is modeled by a Hodgkin–Huxley (HH) model. This microcircuit captures the dynamics by a single compartment, which is described by the following differential equations [28, 46, 47]:

$$\begin{aligned} C_m \frac{dV}{dt} &= -I_{Na} - I_K - I_{Leak} + I_D, \\ \frac{dn}{dt} &= \frac{n_\infty - n}{\tau_n}, \\ \frac{dQ}{dt} &= \omega + \sqrt{2D}\xi(t). \end{aligned} \quad (2.1)$$

Here, C_m denotes the neural membrane capacitance density ($\mu F/cm^2$); V represents the membrane potential (mV); the gating variable n of activated K^+ channels, denotes the activation probability of potassium ion channels; τ_n is the time constant (ms); $\xi(t)$ is Gaussian white noise; ω and D are angular frequency and noise intensity for forcing currents; $Q(t)$ is phase noise; and I_{Na} , I_K , and I_{Leak} are sodium ion current, potassium ion current, and leakage current. Their expressions are as follows:

$$\begin{aligned} I_{Na} &= g_{Na} m_\infty(V) (1 - n) (V - E_{Na}), \\ I_K &= g_K n (V - E_K), \\ I_{Leak} &= g_L (V - E_L), \\ I_D &= A \sin(Q(t)), \end{aligned}$$

where the parameter g_{Na} and g_K are the maximal conductances (mS/cm^2); E_{Na} , E_K , and E_L are the reversal potentials (mV); m_∞ and n_∞ are the steady-state of the ionic gating channels; and A is amplitude for forcing currents. They are modeled using:

$$m_\infty(V) = \frac{1}{1 + \exp\left(-\frac{V + 35}{5}\right)}, \quad n_\infty(V) = \frac{1}{1 + \exp\left(-\frac{V + 36}{5}\right)}.$$

Specifically, we add a voltage-dependent linear control current (I) to this model, which is expressed as follows.

$$\frac{dI}{dt} = \varepsilon(-80 - V). \quad (2.2)$$

Now, ε is the feedback coefficient, and $\varepsilon = 0.001$ is used if not otherwise specified.

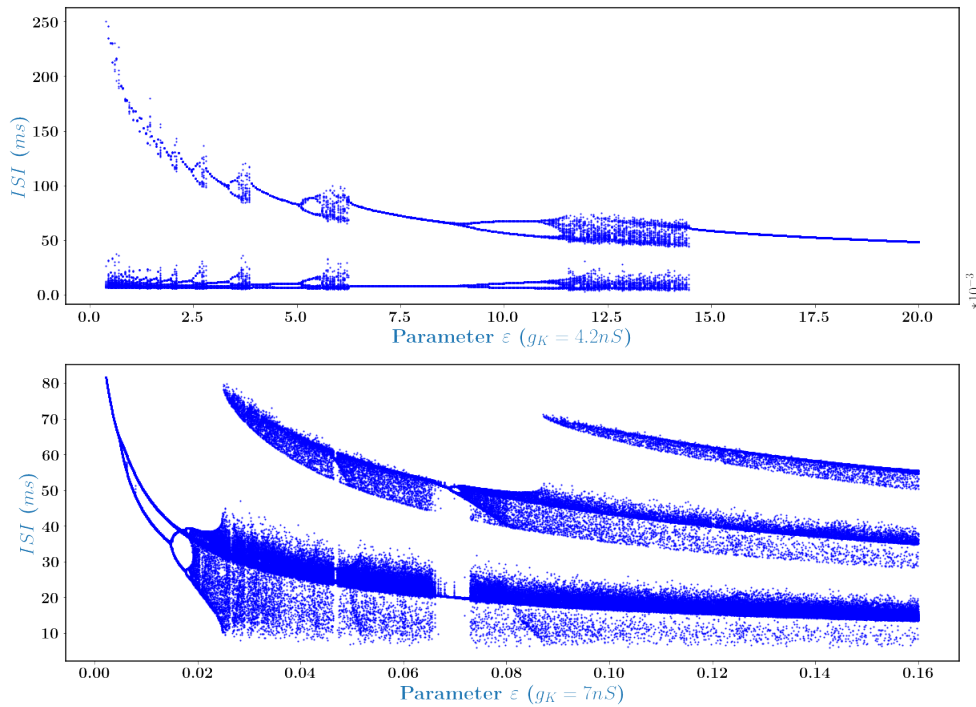


Figure 1. Sequence diagram of interspike intervals of a single neuron for $g_K = 4.2nS$ and $7nS$, as the change of parameter ε .

By adjusting parameters, the HH model can reproduce the firing patterns observed in neurons, which underlie their rhythmic properties in the CPG. Figure 1 displays the sequence diagram of interspike intervals (ISIs) of a single neuron without noise. When $g_K = 4.2nS$, the system undergoes period-doubling bifurcation with the change of parameter ε , leading to chaos. At this point, the system has two period-doubling cascade paths, and the range of parameters that produce chaos broadens as ε increases. One period-doubling cascade path disappears around $\varepsilon = 0.0145$, while the other path has an interspike interval remaining. As we will see below, the system displays the spiking mode when $\varepsilon > 0.0145$. When $g_K = 7nS$, the system shows a bifurcation diagram that resembles the period-adding cascade as parameters increase. There is still a bifurcation path from period-doubling to chaos. The ISI diagram clearly shows three layers, which may contain deep neural information not captured by the firing patterns of neurons. In the following section, we will present the firing sequence diagram for the corresponding parameters of Figure 1.

In Figure 2, the left panel displays the time series for $g_K = 4.2nS$ (above Figure 1). When $\varepsilon = 0.001$, the neuron model exhibits bursting, which corresponds to several ISIs shown in Figure 1. For $\varepsilon = 0.005$ and 0.0075 , there are three and two ISIs respectively, represented by three spikings and two spikings per bursting. When $\varepsilon = 0.01$, this extends to four ISIs, and although the firing pattern appears similar to that of $\varepsilon = 0.0075$, it has changed. At $\varepsilon = 0.0125$, the system discharges chaotically, while at $\varepsilon = 0.015$, the firing is a single spiking. The right panel of Figure 2 displays the time series for $g_K = 7nS$ (below Figure 1). At $\varepsilon = 0.01$, the model discharge shows two ISIs. As the parameter varies from 0.02 to 0.014, the discharge pattern of the model exhibits different chaotic discharges. In this manner, by calculating the ISIs, we can observe the hidden information of the firing sequence.

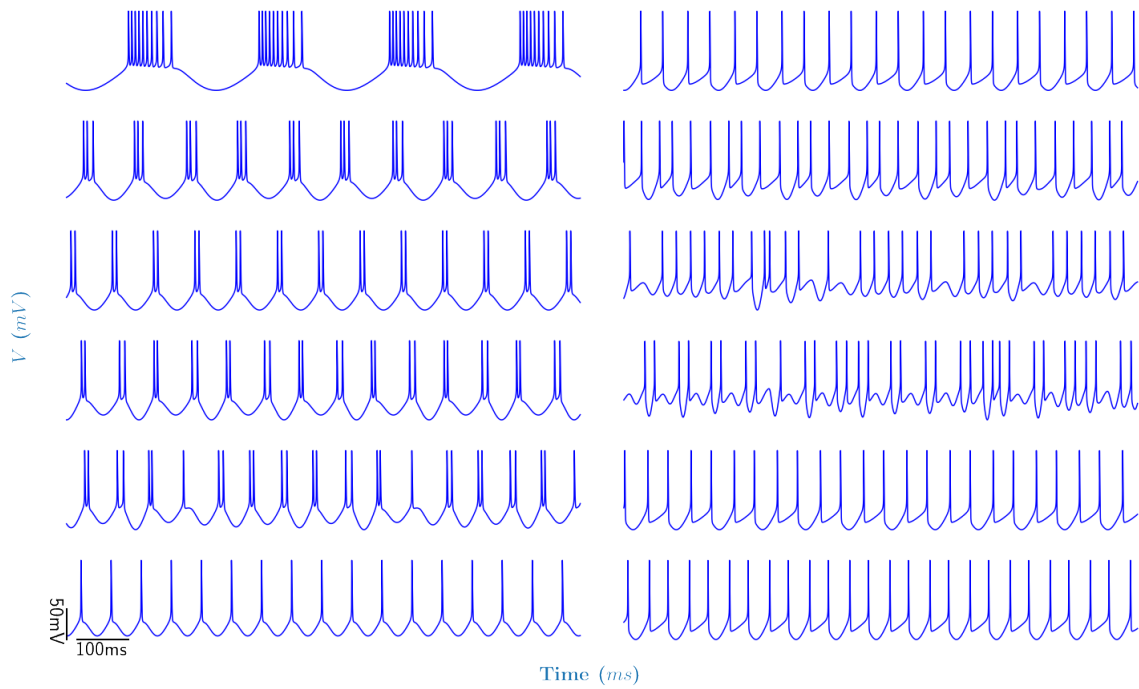


Figure 2. Time series diagram. Left panel $g_K = 4.2nS$ and parameter ε from top to bottom is 0.001, 0.005, 0.0075, 0.01, 0.0125, 0.015; right panel $g_K = 7nS$ and parameter ε from top to bottom is 0.01, 0.02, 0.04, 0.08, 0.12, 0.14.

2.2. CPG based model

The inhibitory relationship between neurons is considered to be a key point in the generation of rhythms. Our CPG models typically consist of two or three neurons. The most common structure describing firing rhythmic activities consists of two coupled neurons that inhibit each other (Figure 3A). This structure is widely known as half-center oscillator and is symmetrically coupled through both inhibitory connections with g_{12} and g_{21} . We will start off with the simplest network where two cells next section. On this basis, we extended the number of neurons to three (Figure 3B,C). In three circuits, neurons and inhibitory synapses (small black solid dots) form a hybrid microcircuit. And neurons are labeled with different colors (blue, red and green) which correspond to the colors in the firing activities. The synaptic transmission contained in the CPG structure in Figure 3 are ionotropic synapses. These synaptic are inhibitory synapses and are modeled using a first-order kinetic equations, which are conductance-based type similar to previous studies [48–51]:

$$\begin{cases} I_{pre \rightarrow post} = g_{pre \rightarrow post} H_{\infty}(V_{pre}) (V_{pre} - E_{pre \rightarrow post}), \\ H_{\infty}(V_{pre}) = \frac{1}{1 + \exp\left(-\frac{V_{pre} - \theta}{\sigma}\right)}. \end{cases} \quad (2.3)$$

Here, V_{pre} is the presynaptic voltage, $\sigma = 1mV$ is the steepness, $\theta = -60mV$ sets the value when the function is semi-activated, $E_{pre \rightarrow post}$ is the reversal potential, and $g_{pre \rightarrow post}$ is the maximal conductance (g_{ij} , $i, j = 1, 2, 3$ & $i \neq j$ in Figure 3).

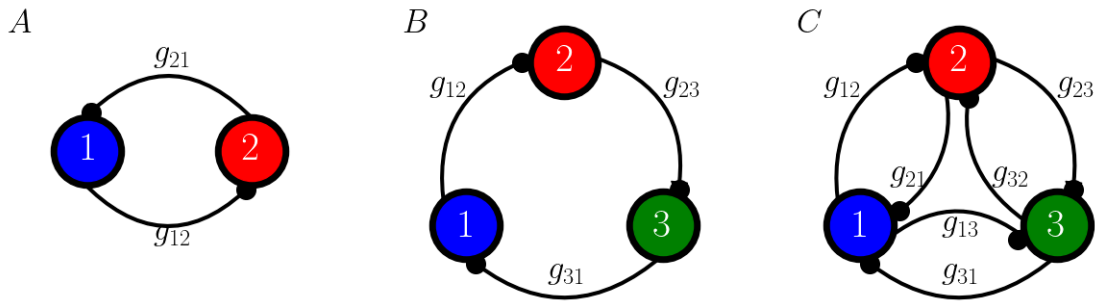


Figure 3. Three different topologies of mutually inhibited neuronal circuits in this study. The solid blue, green, and red circles represent neurons and are labeled as 1, 2 and 3, respectively. These neurons are modeled by the HH model, see eqs 2.1 and 2.2. Black filled circles represent inhibitory synapses and the model see eq 2.3. The conductance of the connection between neurons is noted as g_{ij} , $i, j = 1, 2, 3$ & $i \neq j$. This indicates that the synapse from neuron i to neuron j .

For numerical integration of network system, the fourth-order Runge–Kutta algorithm was used with a time step of $0.05ms$. The total integration time length of each simulation run was $5000ms$. Simulations were implemented in Python 3.9.7 on PC with 12th Gen Intel(R) Core(TM) i7-12700H 2.30 GHz CPU.

3. Results

3.1. The rhythm activity of half-center oscillator

The discussion in this section is based on the reciprocal inhibition of two neurons, which we call half-center oscillators (pattern A in Figure 3). The synchronous firing of neurons contains very important neural information. Here we investigate the synchrony of half-central oscillator rhythm activity. In Figure 4, we show the variation trend of synchronous firing with synaptic parameters of the model, and we can see the roughly synchronous discharge pattern. Fixing the synaptic parameter σ , we can find that the reversal potential E_{syn} has an intermittent effect on synchrony. The effect of the synaptic parameter σ is more continuous than fixing it. The transversely separated bands are very distinct, indicating that the synaptic reversal potential has a significant effect on synchrony. In the following, we will select three appropriate sets of parameters to investigate the synchronization of half-central oscillation according to the phase difference diagram shown in Figure 4. The three sets of parameters are $E_{syn} = -110mV$, $\sigma = 1$ (phase difference between $100ms$ and $200ms$); $E_{syn} = -89mV$, $\sigma = 1/2$ (phase difference between 200 and $250ms$); and $E_{syn} = -61mV$, $\sigma = 1/6$ (phase difference between 0 and $50ms$).

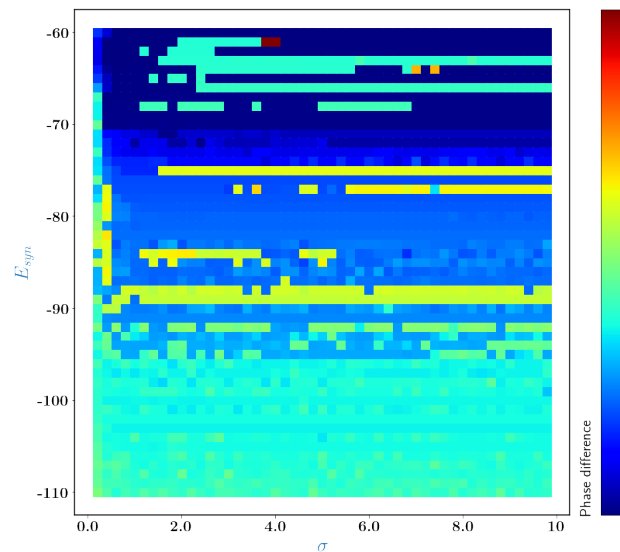


Figure 4. The phase difference bifurcation diagram of the model firing under the change of the bisynaptic parameters. σ and E_{syn} are two synaptic parameters. The smaller the value of the phase difference, the closer it is to synchronization.

From the top of the Figure 5 (i.e., when the synaptic parameters are $E_{syn} = -110mV$ and $\sigma = 1$), as the two-parameter synaptic conductance is changed, the phase difference of the neuronal membrane potential exceeds 100 except near the diagonal. The diagonal is shown in dark blue, indicating that the two neurons are perfectly synchronized. By simulating their discharge state, it can also be confirmed that synchronization is achieved when the conductance parameters of the two synapses are equal. In particular, in the small regime of two synaptic conductances close to zero and close to one, the area of perfect synchrony is slightly larger. Dark purple indicates that the phase difference between the two neurons is maximal. One interesting observation is that the bifurcation diagram of the phase difference is symmetric about the diagonal as the two-parameter synaptic conductance change.

When the synaptic parameters were changed to $E_{syn} = -89mV$ and $\sigma = 1/2$, we obtained the synchronous firing diagram of the half-center oscillator as shown in the middle of Figure 5. The diagonal synchrony seems to be preserved as we can see from the figure. However, the discharge of the diagonal is richer (The variety of the phase difference indicates the richness in the rhythm activity of the half-central oscillator). The bifurcation diagram of the phase difference is still symmetric and we can get a variety of differences in the phase difference depending on the color distribution of the pattern. A variety of rhythm activities of the half-center oscillator can be realized, which makes it easier to operate and transform the half-center oscillator. Furthermore, we can perform the rhythm control of the half-center oscillator. Eventually, we may be able to achieve synchronous control of a half-central oscillator. Synchronization does not necessarily require the two-parameter synaptic conductance to be equal as can be seen from the bottom of Figure 5. Unlike in the previous two diagrams, the distinct dark blue diagonals are missing, but the symmetry about the synaptic conductance is preserved. Here the dark blue area is spread throughout the parameter bifurcation plane and the phase difference is radially spread around the upper right corner, like a ripple of water. Based on the above analysis, small synaptic conductance parameters may make it easier to achieve the synchronous rhythm of the half-center oscillator, and synaptic parameters E_{syn} and σ have significant effects on their synchronization.

In the following, we will investigate the ISIs of each neuron in the half-center oscillator model with different potassium conductance g_K under the above three sets of parameters. The left panel of Figure 6 depicts the bifurcation diagram under the three groups of parameters when the conductance parameter is $4.2nS$. It can be seen from the figure that the rhythm activity in the half-center oscillator of the three bifurcation graphs is not synchronous. The top is like a bifurcation process of inverse period-adding and the discharge of the system is relatively stable. We can see that the discharge is very abundant from the middle, especially when the ε is between 0.01 and 0.015, which can be related to the middle of Figure 5. The bottom shows the complex diversity of ISIs. Like the first two, ISIs are concentrated in two layers and it is in a chaotic state. This corresponds to the bottom of Figure 5 and it is interspersed with large phase differences dotted with dots. When the potassium conductance $g_K = 7nS$, the ISIs for the three sets of parameters are shown on the right panel of Figure 6. Compared with the left panel, the ISIs have changed fundamentally. Neuron 1 in the half-center oscillator shows smaller ISIs than neuron 2 shown at the top. In the middle, there is only one ISI in the former stage, and the chaotic ISIs start to appear in the later stage. Therefore, the change in potassium conductance has a great influence on the rhythm activity of the half-center oscillator.

We analyzed the bifurcation patterns and the ISIs patterns of the half-center oscillator to investigate the rhythm activity when the potassium conductance is changed. Our research found that altering the relative size of the two-parameter synaptic conductances could control the rhythm pattern of the half-center oscillator. Different synaptic parameters such as E_{syn} and σ can trigger very different rhythm patterns. Figure 7 presents an example where we took $E_{syn} = -110mV$, $\sigma = 1$, $g_{12} = 0.2nS$, $g_{21} = 0.8nS$ to investigate the HCO rhythm under different potassium conductances. It turns out that a single spike on the left panel has branches that cause neuron 1's ISIs to decrease when noise is added to it. We looked at the bursts rhythm, spiking rhythm, and mixed mode rhythm in HCO. A large number of discharge patterns can be implemented in HCO, especially when $g_K = 7nS$, by adjusting the asymmetric coupling factor. By comparing the rhythmic activity, we found that when g_{12} is larger than g_{21} , neuron 1 fires earlier than neuron 2, and vice versa. In other words, synaptic conductance parameters can control the firing start time of neurons in HCO. Synapse conductance parameters can also synchronize discharge patterns in HCO as shown in Figure 8 under different discharge modes when the synaptic parameters are exactly equal. Different discharge mode synchronization will occur under different conductances such as burst synchronization, spiking synchronization, and subthreshold synchronization. We found that in HCO, the synchronization regime is likely to appear when the synaptic conductance parameters are equal, but the synchronization state will also appear when the synaptic conductance parameters are not equal. Synaptic parameters are required to participate in the mediation of neuron firing in this case. The inequality of the two synaptic parameters will lead to a rich rhythm pattern of HCO. The synchronization state disappears when noise acts on neuron 1. When $g_K = 4.2nS$, the rhythmic discharge of neuron 1 changes greatly, while the burster structure of neuron 2 is stable. When $g_K = 7nS$, the spiking of neurons is disturbed. In particular, when $g_K = 47.4nS$, only neuron 1, which was originally subthreshold began to discharge, while neuron 2 remained subthreshold.

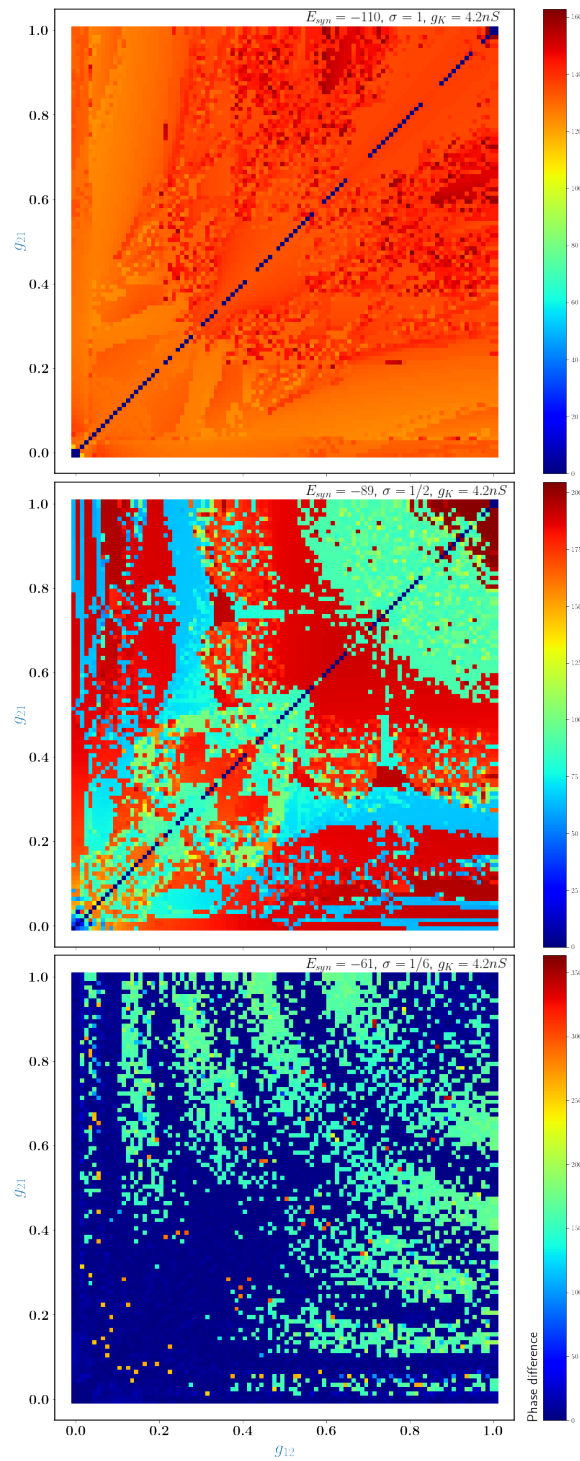


Figure 5. Phase bifurcation diagram as a function of asymmetric coupling factor. Synaptic parameters: top ($E_{syn} = -110$, $\sigma = 1$), middle ($E_{syn} = -89mV$, $\sigma = 1/2$), bottom ($E_{syn} = -61mV$, $\sigma = 1/6$). Potassium conductance $g_K = 4.2nS$. Here dark blue indicates gradual synchronization, and dark purple is the largest phase difference.

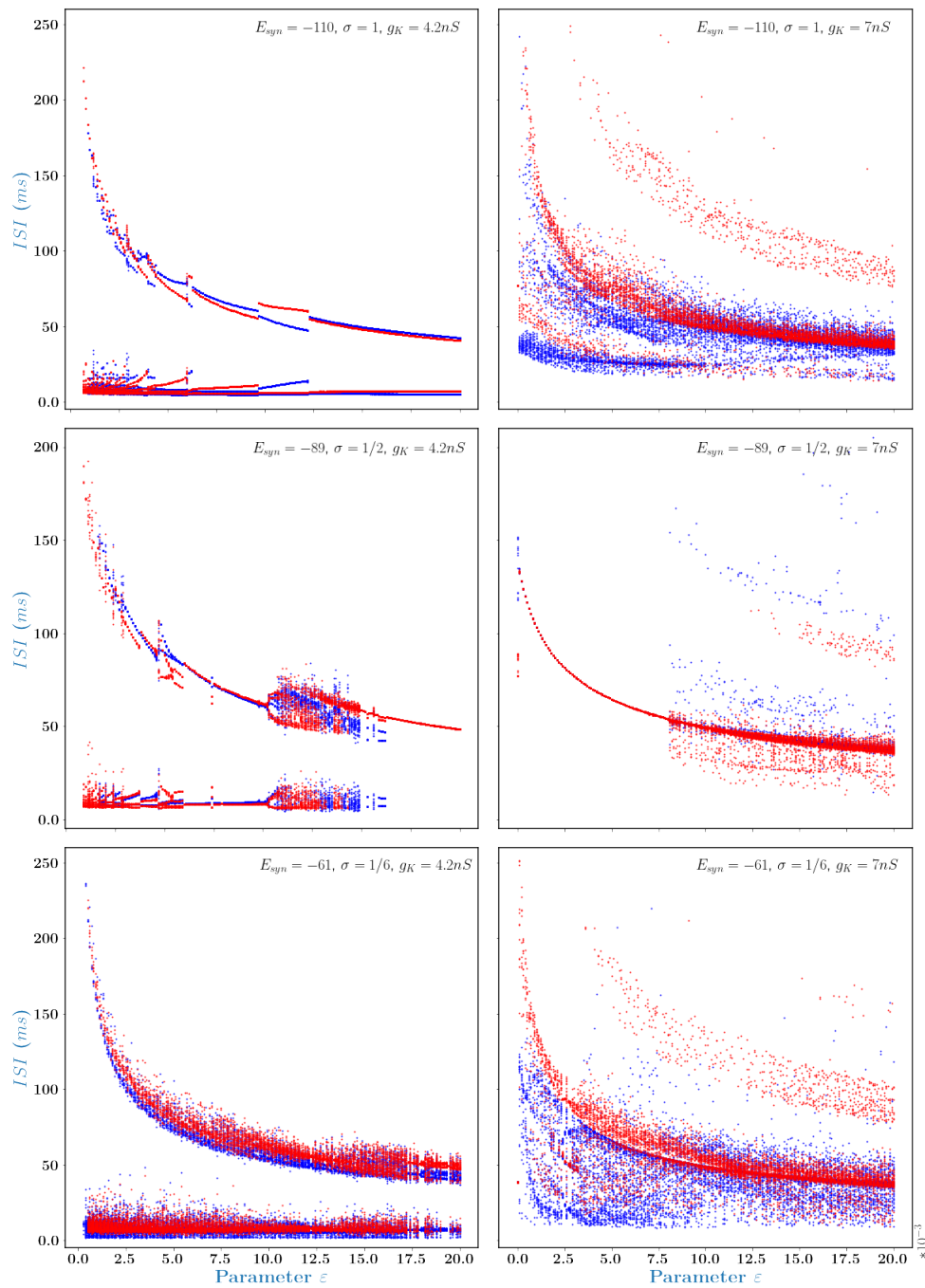


Figure 6. Sequence diagram of interspike intervals of half-center oscillators. The blue track shows the ISIs of neuron 1, and the red track shows the ISIs of neuron 2. Synaptic parameters: top ($E_{syn} = -110\text{mV}$, $\sigma = 1$), middle ($E_{syn} = -89\text{mV}$, $\sigma = 1/2$), and bottom ($E_{syn} = -61\text{mV}$, $\sigma = 1/6$). Left panel: potassium conductance $g_K = 4.2\text{nS}$; right panel: potassium conductance $g_K = 7\text{nS}$.

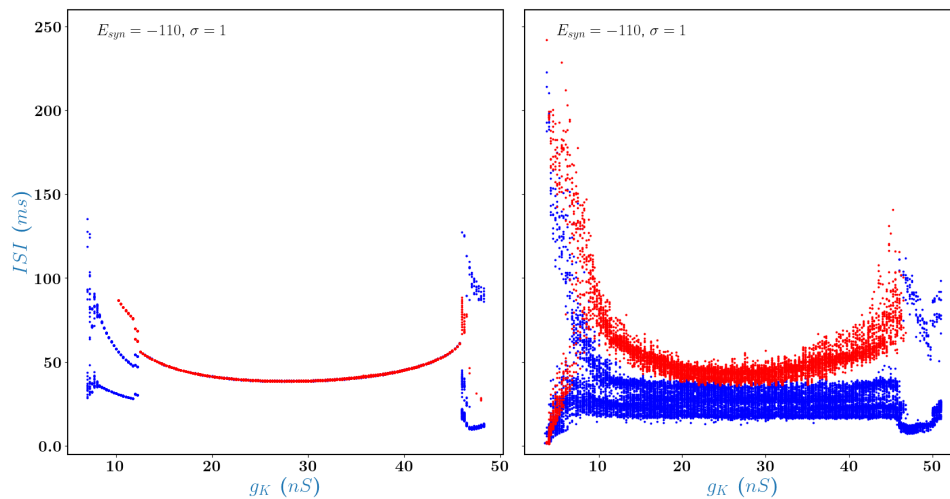


Figure 7. Sequence diagram of interspike intervals of half-center oscillators as potassium conductance changes. Blue shows the firing sequence of neuron 1, red shows the firing sequence of neuron 2. Synaptic conductance $g_{12} = 0.2nS$, $g_{21} = 0.8nS$. The left panel: HCO without noise, and the right panel: HCO with noise and parameters $A = 5$, $D = 2$, $\omega = 0.5$. Here the noise only acts on neuron 1.

Subthreshold oscillation contains rich expression of neuronal information [52]. Here, subthreshold oscillations of the half-center oscillator are shown in Figure 9. As you can be seen from the right panel, Subthreshold oscillations alternate between neurons 1 and 2 in HCO, and subthreshold oscillations appear accompanied by small oscillations at lower membrane voltage values. The subthreshold oscillations in neuron 2 are consistent with the current in synapse 2. A more detailed subthreshold oscillation process can be found in the left panel, where the membrane voltage value of neuron 2 hovers near the lowest center when subthreshold oscillation of neuron 1 begins. When neuron 1 ends subthreshold oscillation, it continuously changes to hover around smaller membrane voltage values, while neuron 2 begins subthreshold oscillation. This is how subthreshold oscillations of neurons 1 and 2 alternate.

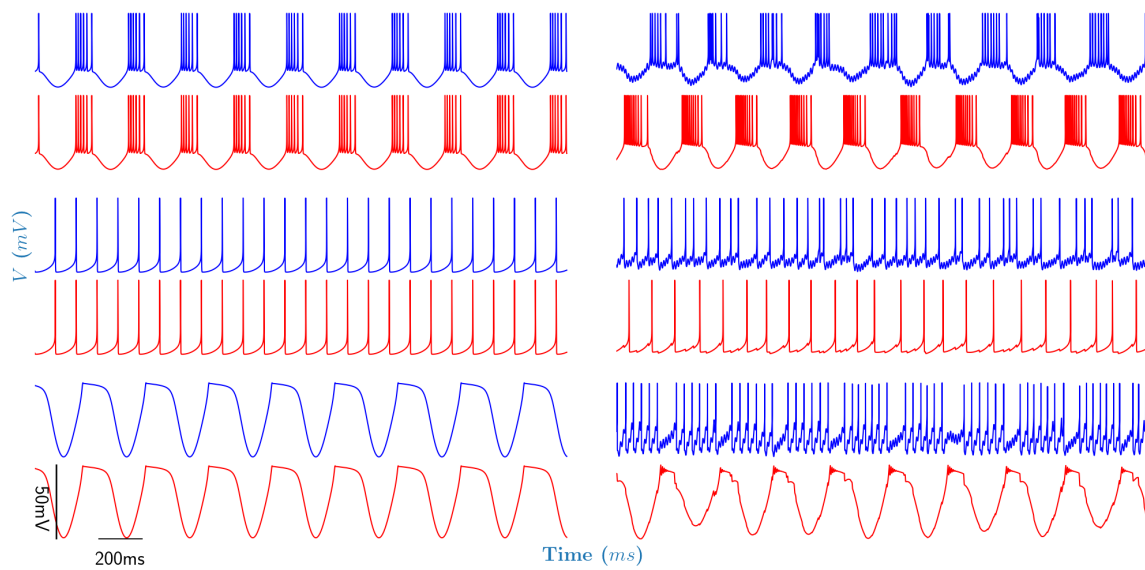


Figure 8. Synchronization of half-center oscillators rhythm activity. Synaptic conductance $g_{12} = 0.1nS$, $g_{21} = 0.1nS$. The top, middle, and bottom represent the synchronization of bursts mode, spiking, and subthreshold oscillation when $g_K = 4.2nS$, $7nS$, and $47.4nS$, respectively. The left panel: HCO without noise, and the right panel: HCO with noise and parameters $A = 5$, $D = 2$, $\omega = 0.5$. Here the noise only acts on neuron 1.

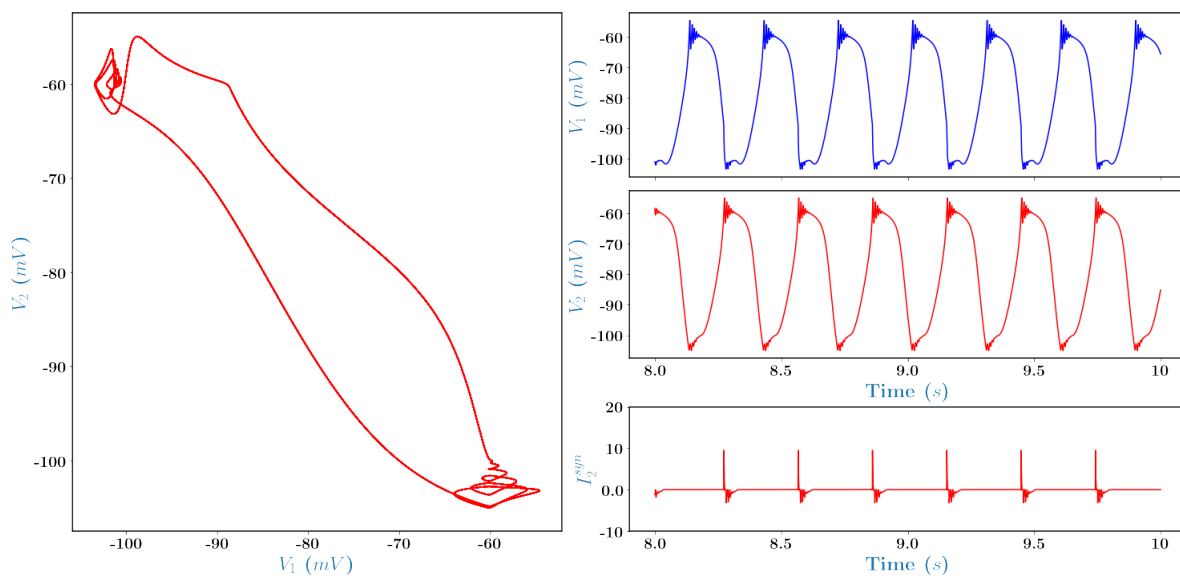


Figure 9. Subthreshold firing phase diagram of half-center oscillator. The left panel is the phase diagram. The right panel, from top to bottom, are the firing of neuron 1, firing of neuron 2, and the current at synapse 2. $g_K = 46.4nS$, $g_{12} = 0.5nS$, $g_{21} = 1.0nS$, $\sigma = 1/5$, $E_{syn} = -100mV$.

3.2. Sequentially inhibit the connected CPG rhythm pattern

This section discusses the patterns B and C (Figure 3) in a tri-neuron CPG. The time difference in calculating its discharge sequence is significant by comparing the single neuron, half-center oscillator, and tri-neuron CPG. The increase in the number of neurons will greatly reduce the computational efficiency. In contrast, the increase in the number of synapses will also affect the computational efficiency, but it is not as obvious as the increase in the number of neurons. Figures 10 and 11 show the discharge pattern in pattern B (Figure 3) under two different synaptic conductance parameters while fixing the potassium conductance $g_K = 4.2nS$ and two synaptic parameters $E_{syn} = -110mV$, $\sigma = 1$. Pattern B (Figure 3) is the sequential inhibition of connected neuronal circuits, g_{ij} indicates the synaptic conductance that the i th neuron inhibits the j th neuron.

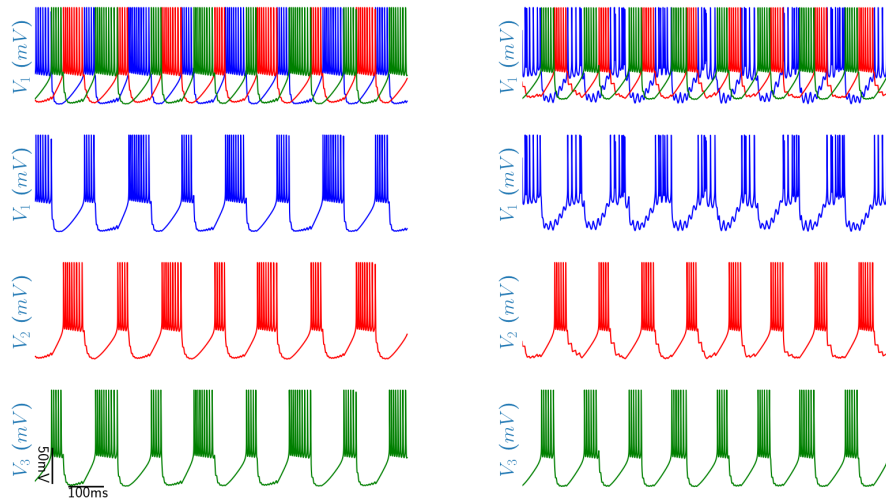


Figure 10. The rhythm pattern is in the tri-neuron CPG. Blue, red, and green are the membrane voltages of neurons 1–3, respectively. The synaptic conductance parameters are $g_{12} = 0.4nS$, $g_{23} = 0.6nS$, $g_{31} = 0.8nS$. The corresponding display is pattern B (Figure 3). The left panel: HCO without noise, and the right panel: HCO with noise and parameters $A = 5$, $D = 2$, $\omega = 0.5$. Here the noise only acts on neuron 1.

As can be seen from Figure 10, for this set of synaptic conductance parameters, members of CPG exhibit different rhythm patterns than those in single neurons and half-center oscillators, which are caused by synaptic coupling of neurons (left panel). If the discharge of blue neuron 1 is taken as the starting point of the member in CPG, the typical CPG rhythm pattern is shown, that is, the discharge order in CPG members is “blue-green-red” or “neuron 1-neuron 3-neuron 2”. When the noise is applied to neuron 1, we find that the firing of neuron 1 changes greatly and the firing of neurons 2 and 3 changes weakly.

When we change the synaptic conductance $g_{12} = 0.1nS$ in Figure 10, the rhythm pattern shown in Figure 11 is obtained. At this time, the subtle shift in the discharge of members in CPG can be controlled by adjusting the synaptic conductance g_{12} . That is, the rhythm pattern control of such CPG members can be realized and changes in synaptic conductance regulate the rhythm pattern of members in CPG. When the noise is applied to neuron 1, the firing of neurons 2 and 3 changes weakly.

When the conductance of three synapses is equal, the members in CPG exhibit the same burst dis-

charge in pattern B (Figure 3). In pattern B, we found a small rule that increased synaptic conductance delayed the start time of postsynaptic neuron firing. When g_{31} is much smaller than g_{12} , neurons 3 and 1 tend to be in sync. Using this property, the firing synchronization of neurons in CPG can be easily regulated and controlled.

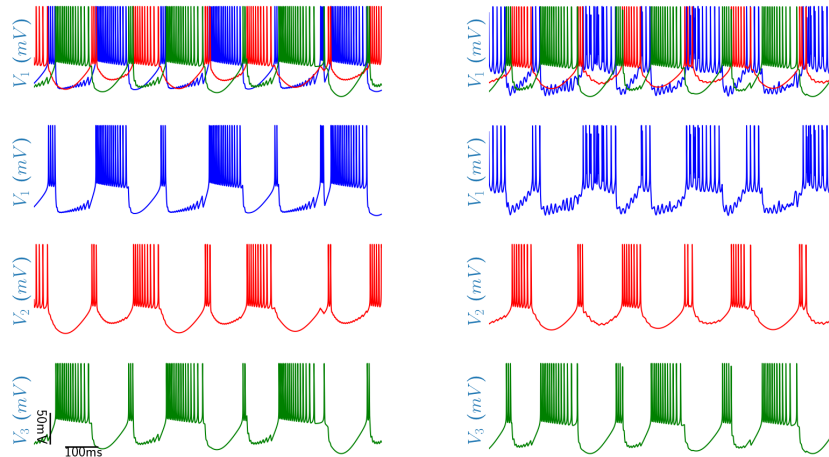


Figure 11. The rhythm pattern is in the tri-neuron CPG. Blue, red, and green are the membrane voltages of neurons 1–3, respectively. The synaptic conductance parameters are $g_{12} = 0.1nS$, $g_{23} = 0.6nS$, $g_{31} = 0.8nS$. The corresponding display is pattern B (Figure 3). The left panel: HCO without noise, and the right panel: HCO with noise and parameters $A = 5$, $D = 2$, $\omega = 0.5$. Here the noise only acts on neuron 1.

3.3. CPG rhythm patterns of reciprocal inhibition connections

In the same way, we also analyze the rhythm pattern of tri-neuron CPG, namely pattern C (Figure 3). This pattern is a tri-neuron circuit composed of pairs of neurons that inhibit each other. Although it has the same two discharge sequences as the members of CPG in pattern B (Figure 3), the discharge mode of members in CPG is completely different from that of pattern B (Figure 3), as shown in Figure 12. At this time, the discharge order of CPG members showed “neuron 1–neuron 2–neuron 3”, but the membrane voltage sequence of neuron 1 is different from that of neurons 2 and 3. Unlike the Figure 10, each member of the CPG behaves in the same discharge. That is, the reciprocal inhibition of the CPG loop increases the diversity of the discharge activities of its members. In addition, we found that when noise was stimulated to neurons 1–3 respectively, the stimulation of neuron 2 completely destroyed the original CPG firing rhythm pattern. The reason may be that the synaptic conductance parameters of neuron 2 are very small.

In particular, when the conductance of each synapse in the CPG is different (As shown in Figure 13), the member of CPG named neuron 1 shows an burster firing pattern, while neurons 2 and 3 show a mixed bursting pattern. The discharge activities of such CPG members are caused by completely asymmetric coupling factor regulation. The results show that asymmetric coupling factors can strongly regulate the discharge of neurons. Under these synaptic parameters, the firing rhythm pattern was substantially altered when we stimulated neurons 1–3 with noise, respectively. This may be because CPG at this synaptic parameter is in a critical state. The members of CPG show very rich discharge activities in pattern C (Figure 3), not all of which are shown here. We also investigated the patterns of

two other types of synaptic connections in which members also have different discharges, only two of which are shown here.

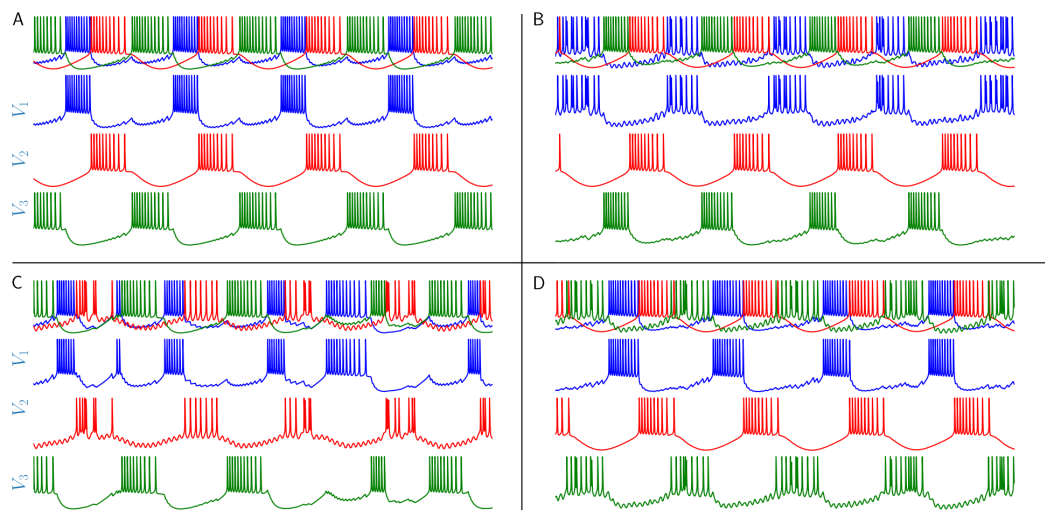


Figure 12. The rhythm pattern is in the tri-neuron CPG. Blue, red, and green are the membrane voltages of neurons 1–3, respectively. The synaptic conductance parameters are $g_{12} = 0.02nS$, $g_{23} = 0.2nS$, $g_{31} = 0.3nS$, $g_{21} = 0.3nS$, $g_{32} = 0.02nS$, $g_{13} = 0.2nS$. The corresponding display is pattern C (Figure 3). A) represents HCO without noise; B), C) and D) represent HCO with noise and parameters $A = 5$, $D = 2$, $\omega = 0.5$. Here the noise only acts on neuron 1 (B), neuron 2 (C), and neuron 3 (D), respectively.

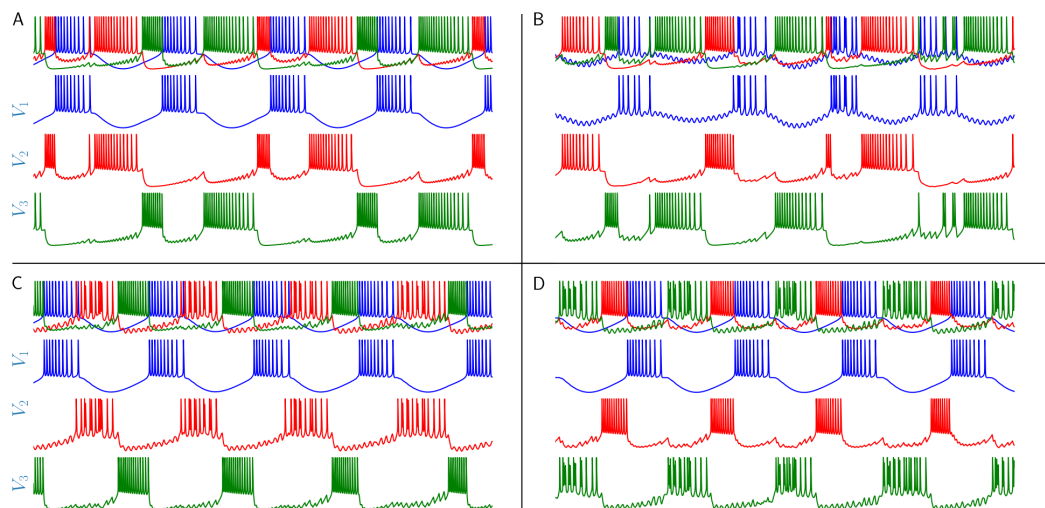


Figure 13. The rhythm pattern is in the tri-neuron CPG. Blue, red, and green are the membrane voltages of neurons 1–3, respectively. The synaptic conductance parameters are $g_{12} = 0.3nS$, $g_{23} = 0.5nS$, $g_{31} = 0.02nS$, $g_{21} = 0.02nS$, $g_{32} = 0.4nS$, $g_{13} = 0.6nS$. The corresponding display is pattern C (Figure 3). A) represents HCO without noise; B), C) and D) represent HCO with noise and parameters $A = 5$, $D = 2$, $\omega = 0.5$. Here the noise only acts on neuron 1 (B), neuron 2 (C), and neuron 3 (D), respectively.

4. Conclusions

This paper first introduces the rich discharge properties of the single neuron model, which has been used in our modeling. Second, the influence of asymmetric coupling factor and two synaptic parameters σ and E_{syn} on the half-center oscillators discharge synchronization is discussed. We find that synaptic parameters and noise together affect the discharge of two neurons in the half-center oscillator. Asymmetric coupling factors modulate the rhythm activity in the half-center oscillator. We find that the firing synchronization occurred not only at the diagonal, but also when the remaining two synaptic parameters σ and E_{syn} are changed. Small synaptic conductance parameters may make it easier to synchronize the half-center oscillator, and the synaptic conductance may control the discharge order of neurons in the half-center oscillator. The interspike intervals diagram of two neurons in the half-center oscillator is used to verify the firing synchronization under several fixed parameters. In addition to the synaptic conductance parameters, the synaptic parameters σ and E_{syn} can be adjusted to increase the diversity of rhythm activity of the half-center oscillator. The synaptic conductance and synaptic parameters together control its rhythm activities. The rhythms properties of CPG are regulated by the potassium conductance value. The typical CPG modes and discharge synchronization of three groups of different potassium conductance parameters are shown, which are bursting, spiking, and mixed-mode oscillations (MMOs) respectively. It has been shown that noise can regulate the discharge rhythm and synchronization of HCO. Finally, two typical pattern are discussed, and how the asymmetric coupling factors regulate the discharge of members in CPG is analyzed.

The asymmetric coupling factor can adjust the discharge mode of CPG members, such as bursting mode, spiking, and MMOs, to realize the control of rhythms activity in CPG. The phase diagram explains the alternations between neuronal firing patterns and the effect of synaptic currents on membrane potential. We simulated six connected modes, and only the discharge modes of members in partial CPG of the three types were shown here. We find that the rhythm activity of neurons in patterns B and C (Figure 3) were more abundant than those in single and half-center oscillators neurons. Asymmetric coupling factors (synaptic conductance) can control the start time of postsynaptic neuron firing, and the increase of synaptic conductance will delay the start time of postsynaptic neuron firing. When potassium conductance g_K is changed, the discharge of CPG members will be greatly changed. For example, when $g_K = 7nS$, the members of CPG show abundant spiking discharge mode in pattern B (Figure 3). In the reciprocal inhibition CPG pattern C (Figure 3), when the potassium conductance $g_K = 4.2nS$ and the synaptic conductance is equal, the members of CPG do not discharge synchronously, which is different from the performance of pattern B (Figure 3). When the potassium conductance $g_K = 7nS$ and the synaptic conductance is equal, the discharge of the CPG members does not spiking synchronously, which is a very interesting question but we have not shown the diagram in detail here due to space constraints. That will be one of the things we will look at in the future. In addition, we found that noise and synaptic strength together determine the robustness of CPG, and the critical state of CPG rhythmic discharge is sensitive to noise. Furthermore, we have observed the same noise had a greater effect on the rhythm changes of neurons with lower synaptic strength. That is, high strength inhibition connection will improve the stability of CPG. Of course, the changes in synaptic parameters can also regulate the discharge mode of CPG members, so these factors will jointly determine the discharge mode of CPG members. The influence of comprehensive factors will be the focus and difficulty of our future research, and the rhythm activities of other members will also need to be

investigated. Finally, synapse parameters will be integrated to control and realize the rhythm activity of CPG.

Our study focused on the chemical synapses between neurons, while the electrical coupling between them was not considered. However, in future studies, we will analyze the synergistic effects of both electrical and chemical coupling in CPG as it can lead to very different rhythmic patterns. Our current model demonstrates that synaptic conductance can influence the rhythm pattern of the tri-neuron network and a change in the conductance can shift the members of the CPG into typical regular sequential discharge mode. Our findings reveal a unique rhythm pattern in CPG, where neuron 1 exhibits chaotic spiking while neurons 2 and 3 show regular bursting. This rhythmic activity and regular sequential discharge pattern of the CPG is crucial for its flexibility, robustness, and ultimate realization of swimming, walking, or other cognitive functions. The diversity of rhythm activities in CPG is essential for its flexibility and robustness, which can resist interference from external information. Changes in synaptic conductance and noise can produce a large number of different rhythm activities, making the CPG less susceptible to external interference.

CPG rhythm patterns have been discovered in invertebrates (crustacean pyloric or gastric) and leech heartbeats. These patterns are used to simulate the rhythm activity of the human central nervous system, which in turn controls the rhythm of arm movement [17]. Additionally, CPG rhythm can help in the diagnosis of various diseases. For instance, Mader et al. [1] have claimed that CPG can assist in the development of therapeutic methods for the recovery of strong spinal cord injuries. Tassinari et al. reviewed the relationship of central pattern generators with parasomnias and sleep-related epileptic seizures and explained some epileptic seizures and parasomnias using the firing patterns of the CPG [53, 54]. Therefore, studying the functioning principle of CPG rhythm activities is essential for understanding related motor behaviors and achieving better motor control as well as improving disease diagnosis.

Use of AI tools declaration

The authors declare they have not used Artificial Intelligence (AI) tools in the creation of this article.

Acknowledgments

This work was funded by the National Natural Science Foundation of China (Grant Nos. 12202208 and 11872183), the Basic Science (Natural Science) Research Project of Colleges and Universities of Jiangsu Province (Grant No. 22KJB130009), the Research and Cultivation Project for Young Teachers of Nanjing Audit University (Grant No. 2021QNPY015), 2022 Doctoral program of Entrepreneurship and Innovation in Jiangsu Province (Grant No. JSSCBS20220717), the China Scholarship Council (Grant No. 202206150096).

Conflict of interest

The authors declare there is no conflict of interest.

References

1. E. Marder, D. Bucher, Central pattern generators and the control of rhythmic movements, *Curr. Biol.*, **11** (2001), R986–R996. [https://doi.org/10.1016/S0960-9822\(01\)00581-4](https://doi.org/10.1016/S0960-9822(01)00581-4)
2. E. Marder, R. L. Calabrese, Principles of rhythmic motor pattern generation, *Physiol. Rev.*, **76** (1996), 687–717. <https://doi.org/10.1152/physrev.1996.76.3.687>
3. A. Sakurai, C. A. Gunaratne, P. S. Katz, Two interconnected kernels of reciprocally inhibitory interneurons underlie alternating left-right swim motor pattern generation in the mollusk *Melibe leonina*, *J. Neurophysiol.*, **112** (2014), 1317–1328. <https://doi.org/10.1152/jn.00261.2014>
4. D. Alaçam, A. Shilnikov, Making a swim central pattern generator out of latent parabolic bursters, *Int. J. Bifurcation Chaos*, **25** (2015), 1540003. <https://doi.org/10.1142/S0218127415400039>
5. A. I. Selverston, *Model Neural Networks and Behavior*, New York, 1985. <https://doi.org/10.1007/978-1-4757-5858-0>
6. W. N. Frost, P. S. Katz, Single neuron control over a complex motor program, *PNAS*, **93** (1996), 422–426. <https://doi.org/10.1073/pnas.93.1.422>
7. P. S. Katz, S. L. Hooper, Invertebrate central pattern generators, *Cold Spring Harbor Monogr. Ser.*, **49** (2007), 251.
8. E. Marder, S. Kedia, E. O. Morozova, New insights from small rhythmic circuits, *Curr. Opin. Neurobiol.*, **76** (2022), 102610. <https://doi.org/10.1016/j.conb.2022.102610>
9. E. Marder, Neuromodulation of neuronal circuits: back to the future, *Neuron*, **76** (2012), 1–11. <https://doi.org/10.1016/j.neuron.2012.09.010>
10. I. Belykh, A. Shilnikov, When weak inhibition synchronizes strongly desynchronizing networks of bursting neurons, *Phys. Rev. Lett.*, **101** (2008), 078102. <https://doi.org/10.1103/PhysRevLett.101.078102>
11. T. Nowotny, M. I. Rabinovich, Dynamical origin of independent spiking and bursting activity in neural microcircuits, *Phys. Rev. Lett.*, **98** (2007), 128106. <https://doi.org/10.1103/PhysRevLett.98.128106>
12. A. I. Selverston, Invertebrate central pattern generator circuits, *Phil. Trans. R. Soc. B*, **365** (2010), 2329–2345. <https://doi.org/10.1098/rstb.2009.0270>
13. A. I. Selverston, M. I. Rabinovich, H. D. Abarbanel, R. Elson, A. Szücs, R. D. Pinto, et al., Reliable circuits from irregular neurons: a dynamical approach to understanding central pattern generators, *J. Physiol.-Paris*, **94** (2000), 357–374. [https://doi.org/10.1016/S0928-4257\(00\)01101-3](https://doi.org/10.1016/S0928-4257(00)01101-3)
14. R. Huerta, M. A. Sánchez-Montañés, F. Corbacho, J. A. Sigüenza, A central pattern generator to control a pyloric-based system, *Biol. Cybern.*, **82** (2000), 85–94. <https://doi.org/10.1007/PL00007963>
15. M. Lodi, A. L. Shilnikov, M. Storace, Design principles for central pattern generators with preset rhythms, *IEEE Trans. Neural Networks Learn. Syst.*, **31** (2019), 3658–3669. <https://doi.org/10.1109/TNNLS.2019.2945637>
16. S. Chen, Y. Liu, T. Chen, J. Lou, Rhythm motion control in bio-inspired fishtail based on central pattern generator, *IET Cyber-Syst. Robot.*, **3** (2021), 53–67. <https://doi.org/10.1049/csy2.12007>

17. J. Wojcik, J. Schwabedal, R. Clewley, A. L. Shilnikov, Key bifurcations of bursting polyrhythms in 3-cell central pattern generators, *PLoS One*, **9** (2014), e92918. <https://doi.org/10.1371/journal.pone.0092918>
18. J. T. C. Schwabedal, A. B. Neiman, A. L. Shilnikov, Robust design of polyrhythmic neural circuits, *Phys. Rev. E*, **90** (2014), 022715. <https://doi.org/10.1103/PhysRevE.90.022715>
19. R. Azodi-Avval, F. Bahrami, A mathematical model of arm movement during rhythmic motor activity, in *2011 18th Iranian Conference of Biomedical Engineering (ICBME)*, (2011), 304–308. <https://doi.org/10.1109/ICBME.2011.6168578>
20. M. B. Reyes, P. V. Carelli, J. C. Sartorelli, R. D. Pinto, A modeling approach on why simple central pattern generators are built of irregular neurons, *PLoS One*, **10** (2015), e0120314. <https://doi.org/10.1371/journal.pone.0120314>
21. J. Dethier, G. Drion, A. Franci, R. Sepulchre, A positive feedback at the cellular level promotes robustness and modulation at the circuit level, *J. Neurophysiol.*, **114** (2015), 2472–2484. <https://doi.org/10.1152/jn.00471.2015>
22. J. Collens, K. Pusuluri, A. Kelley, D. Knapper, T. Xing, S. Basodi, et al., Dynamics and bifurcations in multistable 3-cell neural networks, *Chaos*, **30** (2020), 072101. <https://doi.org/10.1063/5.0011374>
23. Q. Lu, X. Wang, J. Tian, A new biological central pattern generator model and its relationship with the motor units, *Cognit. Neurodyn.*, **16** (2022), 135–147. <https://doi.org/10.1007/s11571-021-09710-0>
24. Q. Lu, J. Tian, Synchronization and stochastic resonance of the small-world neural network based on the CPG, *Cognit. Neurodyn.*, **8** (2014), 217–226. <https://doi.org/10.1007/s11571-013-9275-8>
25. Y. Zang, E. Marder, Neuronal morphology enhances robustness to perturbations of channel densities, *PNAS*, **120** (2023), e2219049120. <https://doi.org/10.1073/pnas.2219049120>
26. E. M. Izhikevich, Neural excitability, spiking, and bursting, *Int. J. Bifurcation Chaos*, **10** (2000), 1171–1266. <https://doi.org/10.1142/S0218127400000840>
27. B. Lu, X. Jiang, Reduced and bifurcation analysis of intrinsically bursting neuron model, *Electron. Res. Arch.*, **31** (2023), 5928–5945. <https://doi.org/10.3934/era.2023301>
28. F. Zhan, S. Liu, X. Zhang, J. Wang, B. Lu, Mixed-mode oscillations and bifurcation analysis in a pituitary model, *Nonlinear Dyn.*, **94** (2018), 807–826. <https://doi.org/10.1007/s11071-018-4395-7>
29. W. B. Kristan, Neuronal decision-making circuits, *Curr. Biol.*, **18** (2008), R928–R932. <https://doi.org/10.1016/j.cub.2008.07.081>
30. K. L. Briggman, W. B. Kristan, Multifunctional pattern-generating circuits, *Annu. Rev. Neurosci.*, **31** (2008), 271–294. <https://doi.org/10.1146/annurev.neuro.31.060407.125552>
31. A. A. A. Hill, J. Lu, M. A. Masino, O. H. Olsen, R. L. Calabrese, A model of a segmental oscillator in the leech heartbeat neuronal network, *J. Comput. Neurosci.*, **10** (2001), 281–302. <https://doi.org/10.1023/A:1011216131638>
32. R. L. Calabrese, Half-center oscillators underlying rhythmic movements, in *The Handbook of Brain Theory and Neural Networks*, (1998), 444–447.

33. Y. Zang, S. Hong, E. D. Schutter, Firing rate-dependent phase responses of Purkinje cells support transient oscillations, *eLife*, **9** (2020), e60692. <https://doi.org/10.7554/eLife.60692>
34. M. Liu, L. Duan, In-phase and anti-phase spikes synchronization within mixed Bursters of the pre-Bötzinger complex, *Electron. Res. Arch.*, **30** (2022), 961–977. <https://doi.org/10.3934/era.2022050>
35. S. Li, G. Zhang, J. Wang, Y. Chen, B. Deng, Emergent central pattern generator behavior in chemical coupled two-compartment models with time delay, *Physica A*, **491** (2018), 177–187. <https://doi.org/10.1016/j.physa.2017.08.121>
36. A. Doloc-Mihu, R. L. Calabrese, A database of computational models of a half-center oscillator for analyzing how neuronal parameters influence network activity, *J. Biol. Phys.*, **37** (2011), 263–283. <https://doi.org/10.1007/s10867-011-9215-y>
37. A. Doloc-Mihu, R. L. Calabrese, Analysis of family structures reveals robustness or sensitivity of bursting activity to parameter variations in a half-center oscillator (HCO) model, *eNeuro*, **3** (2016). <https://doi.org/10.1523/ENEURO.0015-16.2016>
38. I. Elices, P. Varona, Asymmetry factors shaping regular and irregular bursting rhythms in central pattern generators, *Front. Comput. Neurosci.*, **11** (2017), 9. <https://doi.org/10.3389/fncom.2017.00009>
39. A. J. White, Sensory feedback expands dynamic complexity and aids in robustness against noise, *Biol. Cybern.*, **116** (2022), 267–269. <https://doi.org/10.1007/s00422-021-00917-2>
40. Z. Yu, P. J. Thomas, Dynamical consequences of sensory feedback in a half-center oscillator coupled to a simple motor system, *Biol. Cybern.*, **115** (2021), 135–160. <https://doi.org/10.1007/s00422-021-00864-y>
41. R. Huerta, P. Varona, M. I. Rabinovich, H. D. I. Abarbanel, Topology selection by chaotic neurons of a pyloric central pattern generator, *Biol. Cybern.*, **84** (2001), L1–L8. <https://doi.org/10.1007/PL00007976>
42. V. In, A. Kho, P. Longhini, J. D. Neff, A. Palacios, P. L. Buono, Meet ANIBOT: the first biologically-inspired animal robot, *Int. J. Bifurcation Chaos*, **32** (2022), 2230001. <https://doi.org/10.1142/S0218127422300014>
43. A. S. Lele, Y. Fang, J. Ting, A. Raychowdhury, Learning to walk: bio-mimetic hexapod locomotion via reinforcement-based spiking central pattern generation, *IEEE J. Emerging Sel. Top. Circuits Syst.*, **10** (2020), 536–545. <https://doi.org/10.1109/JETCAS.2020.3033135>
44. T. Sun, Z. Dai, P. Manoonpong, Distributed-force-feedback-based reflex with online learning for adaptive quadruped motor control, *Neural Networks*, **142** (2021), 410–427. <https://doi.org/10.1016/j.neunet.2021.06.001>
45. A. Espinal, H. Rostro-Gonzalez, M. Carpio, E. I. Guerra-Hernandez, M. Ornelas-Rodriguez, M. Sotelo-Figueroa, Design of spiking central pattern generators for multiple locomotion gaits in hexapod robots by christiansen grammar evolution, *Front. Neurobot.*, **10** (2016), 6. <https://doi.org/10.3389/fnbot.2016.00006>
46. F. Zhan, S. Liu, Response of electrical activity in an improved neuron model under electromagnetic radiation and noise, *Front. Comput. Neurosci.*, **11** (2017), 107. <https://doi.org/10.3389/fncom.2017.00107>

47. F. Zhan, S. Liu, J. Wang, B. Lu, Bursting patterns and mixed-mode oscillations in reduced Purkinje model, *Int. J. Mod. Phys. B*, **32** (2018), 1850043. <https://doi.org/10.1142/S0217979218500431>
48. D. Terman, J. E. Rubin, A. C. Yew, C. J. Wilson, Activity patterns in a model for the subthalamopallidal network of the basal ganglia, *J. Neurosci.*, **22** (2002), 2963–2976. <https://doi.org/10.1523/JNEUROSCI.22-07-02963.2002>
49. F. Su, J. Wang, S. Niu, H. Li, B. Deng, C. Liu, et al., Nonlinear predictive control for adaptive adjustments of deep brain stimulation parameters in basal ganglia–thalamic network, *Neural Networks*, **98** (2018), 283–295. <https://doi.org/10.1016/j.neunet.2017.12.001>
50. J. Song, S. Liu, H. Lin, Model-based quantitative optimization of deep brain stimulation and prediction of Parkinson's states, *Neuroscience*, **498** (2022), 105–124. <https://doi.org/10.1016/j.neuroscience.2022.05.019>
51. J. Song, H. Lin, S. Liu, Basal ganglia network dynamics and function: role of direct, indirect and hyper-direct pathways in action selection, *Network: Comput. Neural Syst.*, **34** (2023), 84–121. <https://doi.org/10.1080/0954898X.2023.2173816>
52. M. Valero, I. Zutshi, E. Yoon, G. Buzsáki, Probing subthreshold dynamics of hippocampal neurons by pulsed optogenetics, *Science*, **375** (2022), 570–574. <https://doi.org/10.1126/science.abm1891>
53. C. A. Tassinari, G. Cantalupo, B. Hoegl, P. Cortelli, L. Tassi, S. Francione, et al., Neuroethological approach to frontolimbic epileptic seizures and parasomnias: the same central pattern generators for the same behaviours, *Rev. Neurol.*, **165** (2009), 762–768. <https://doi.org/10.1016/j.neurol.2009.08.002>
54. C. A. Tassinari, E. Gardella, G. Cantalupo, G. Rubboli, Relationship of central pattern generators with parasomnias and sleep-related epileptic seizures, *Sleep Med. Clin.*, **7** (2012), 125–134. <https://doi.org/10.1016/j.jsmc.2012.01.003>



AIMS Press

©2024 the Author(s), licensee AIMS Press. This is an open access article distributed under the terms of the Creative Commons Attribution License (<http://creativecommons.org/licenses/by/4.0>)



Research article

Complex rhythm and synchronization of half-center oscillators under electromagnetic induction

Feibiao Zhan¹ and Jian Song^{2,3,*}

¹ School of Mathematics, Nanjing Audit University, Nanjing 211815, China

² School of Mathematics, South China University of Technology, Guangzhou 510640, China

³ School of Mathematical and Computational Sciences, Massey University, Auckland 4442, New Zealand

* **Correspondence:** Email: masongj_vlp@mail.scut.edu.cn.

Abstract: Half-center oscillators are typical small circuits that are crucial for understanding CPG. The complex rhythms of CPG are closely related to certain diseases, such as epilepsy. This paper considered the influence of electromagnetic induction on the discharge mode of the half-center oscillators. First, we analyzed the response of individual firing neuron rhythms to electromagnetic induction when the slow-variable parameters vary. We also discussed the changes in the dynamic bifurcation structure when the intensity of electromagnetic induction varies. Furthermore, we determined the effects of mutually inhibitory and self-inhibitory synaptic parameters on the firing rhythm of the half-center oscillators. The different responses induced by electromagnetic induction interventions, showed that mutually inhibitory synapses modulate the firing rhythm weakly and self-inhibition synapses have a significant impact on firing rhythm. Finally, with the change of synaptic parameter values, the combined effects of autapse and mutually inhibitory synapses on the discharge rhythm of half-center oscillators were analyzed in symmetric and asymmetric autapse modes. It was found that the synchronous state of the half-center oscillators had a more robust electromagnetic induction response than the asynchronous state.

Keywords: complex rhythm; half-center oscillators; synchronization; neuron model; electromagnetic induction

1. Introduction

Central pattern generator (CPG) rhythms have been discovered in invertebrates such as crustacean pyloric or gastric and leech heartbeats. CPGs are typical small circuits of neural networks, providing a new perspective on how circuit dynamics depend on neurons and synapses. CPG can spontaneously

generate multiple rhythmic patterns in the absence of external stimuli [1, 2], and it is associated with various motor behaviors, such as swimming and walking [3, 4]. The characteristics of CPG are described as the stability and robustness of the firing rhythm of neuronal small circuits. Recently, a large amount of research has focused on the working mechanism of CPG from both theoretical and experimental perspectives, providing a biological theoretical basis for the study of CPG-inspired rhythmic motion control [5–8]. Still, only some have directly studied the discharge rhythm of CPG. However, how to efficiently control and use the flexibility and robustness of CPG to guide research inspired by it is still being explored. Some researchers believe that the connection of CPG forms attractors, and each attractor corresponds to a rhythmic motor behavior [9]. Theoretical researchers have explained the potential internal mechanisms of CPG from a dynamic perspective [10], revealing the mechanism of the emergence, disappearance, and stabilization of neuronal rhythms in a tri-neuron network with mutual inhibition under changes in synaptic parameters. Lu et al. investigated the synchronization and stochastic resonance characteristics of small-world networks based on CPG [11]. Researchers have studied the impact of transient input on neuronal firing using phase response curves [12, 13].

Recent studies have shown how the morphology of neurons can significantly affect the rhythmic patterns of CPG circuits [14]. There are many studies on the mechanism of neuronal rhythm generation [15–19], but it is unclear whether the different firing mechanisms of neurons mean the diversity of CPG circuit functions. Can the same CPG circuit generate multiple motion behaviors, making its motion functions diverse [20, 21]. Research has shown that the generation of motor behavior depends on the rhythmic modulation of CPG. One proposal suggests that the CPG rhythm pattern can simulate the human central system's rhythmic activity and control the arm movement rhythm [22]. In addition, CPG rhythm patterns can improve the diagnosis of multiple diseases. For instance, Mader et al. [1] explained that CPG can assist in developing therapeutic methods for the recovery of spinal solid cord injuries. Tassinari et al. reviewed the relationship of central pattern generators with parasomnias and sleep-related epileptic seizures. They explained some epileptic seizures and parasomnias using the rhythm patterns of the CPG [23, 24]. Therefore, studying the functioning principle of CPG rhythm activities is essential for understanding related motor behaviors, improving motor control and disease diagnosis. It is necessary to examine the diversity of rhythm patterns to understand the function of CPG. The study of CPG rhythm patterns has recently been discussed [25, 26].

A half-center oscillator (HCO) is a unit composed of two neurons that mutually inhibit each other, and studying the rhythmic pattern of HCO is crucial for understanding CPG [27, 28]. Studying motion control is facilitated by the easy identification of HCO rhythm patterns. Researchers discussed how neuron parameters affect the rhythmic patterns of HCO to achieve motion control [29], and analyze how the system parameter space changes the robustness of HCO rhythmic patterns [30]. Recently, delayed half-center oscillator (DHCO) in-phase and antiphase dynamics behavior and the coexistence of multiple routes leads to chaos was studied [31, 32]. Noise closely affects the robustness of HCO rhythm patterns [33], and the impact of electromagnetic induction on neuronal firing rhythms and diseases such as epilepsy cannot be ignored [34, 35]. Few people have paid attention to the effects of electromagnetic induction and connection modes on the HCO discharge rhythm. Here, the synaptic conductance parameters and the effects of electromagnetic induction on the HCO rhythm pattern are analyzed. Mutual inhibitory neurons can improve the stability of HCO. Here, we explore the rhythmic pattern of HCO under electromagnetic induction, and a model containing self-inhibitory synapses and mutual inhibitory synapses is established. We examine the impact of electromagnetic induction and

connection modes on the HCO rhythm pattern.

This study investigates complex rhythm and synchronization of HCOs under electromagnetic induction. First, the dynamic changes of individual neurons under electromagnetic induction are analyzed. Moreover, we discuss the effects of mutual inhibition and self-inhibition synaptic parameters on the rhythmic patterns of HCO and show their different responses to electromagnetic induction. The results indicate that mutual inhibition has a weaker effect on the discharge rhythm than self-inhibition. The study examines the impact of self-inhibition synapses, mutual inhibitory synapses, and electromagnetic induction on the HCO rhythm pattern, both symmetrically and asymmetrically. It has been found that the synchronous state of the HCO exhibits a more robust electromagnetic induction response than the asynchronous state. Rhythm patterns are closely related to motor control. The research of rhythmic patterns of small circuits contributes to the development of intelligent science. Intelligent science is inspired by the principle of biological CPG and the establishment of spiking neural networks [36,37].

The paper is organized as follows. Section 2 presents the materials and methods we used to build HCO, including the Hodgkin–Huxley (HH) neuron model. Then, Section 3.1 illustrates the rhythmic discharge of HCOs with different synaptic coupling. Section 3.2 investigates the synchronization of HCOs with different symmetric and asymmetric autapses. Finally, we have a discussion and conclusion in Section 4.

2. Materials and methods

2.1. Neuronal model and dynamics under electromagnetic induction

In our CPG, each interneuron is modeled by a simplified HH model. Variable ϕ denotes the magnetic flux across the membrane, and $\rho(\phi)$ represents the incremental memductance function of flux controlled memristor [38], which is used to describe the coupling between membrane potential and magnetic flux. The incremental memductance function is often described by $\rho(\phi) = \alpha + 3\beta\phi^2$, and α, β are fixed parameters [38,39]. The term $k\rho(\phi)V$ could be viewed as induction current on the membrane as follows:

$$i' = \frac{dq(\phi)}{dt} = \frac{dq(\phi)}{d\phi} \frac{d\phi}{dt} = \rho(\phi)V_0 = k\rho(\phi)V.$$

This microcircuit captures the dynamics by a single compartment, which is described by the following differential equations [17, 34, 40]:

$$\begin{aligned} C_m \frac{dV}{dt} &= -I_{Na} - I_K - I_{Leak} + I + k\rho(\phi)V, \\ \frac{dn}{dt} &= \frac{n_\infty - n}{\tau_n}, \\ \frac{dI}{dt} &= \varepsilon(-80 - V), \\ \frac{d\phi}{dt} &= (k_1 V - k_2 \phi). \end{aligned} \tag{2.1}$$

Here, C_m denotes the neural membrane capacitance density ($\mu F/cm^2$); V represents the membrane potential (mV); the gating variable n of activated K^+ channels denotes the activation probability of

potassium ion channels; the h variable (the formulations of I_{Na} in the original model) represents a merged refractory variable (Na^+ inactivation and K^+ activation). It is replaced by $1 - n$ in the simplified HH model. So, the n gate appears in the formulations of I_{Na} . τ_n is the time constant (ms); I is a voltage-dependent linear control current; electromagnetic induction parameters are $\alpha = 0.1, \beta = 0.02, k_1 = 0.9, k_2 = 0.5$; and I_{Na} , I_K , and I_{Leak} are sodium ion current, potassium ion current, and leakage current. Their expressions are as follows.

$$\begin{aligned} I_{Na} &= g_{Na} m_{\infty}(V) (1 - n) (V - E_{Na}), \\ I_K &= g_K n (V - E_K), \\ I_{Leak} &= g_L (V - E_L), \end{aligned}$$

where the parameters g_{Na} and g_K are the maximal conductances (mS/cm^2); E_{Na} , E_K , and E_L are the reversal potentials (mV); and m_{∞} and n_{∞} are the steady-state of the ionic gating channels. They are modeled using:

$$m_{\infty}(V) = \frac{1}{1 + \exp\left(-\frac{V + 35}{5}\right)}, n_{\infty}(V) = \frac{1}{1 + \exp\left(-\frac{V + 36}{5}\right)}.$$

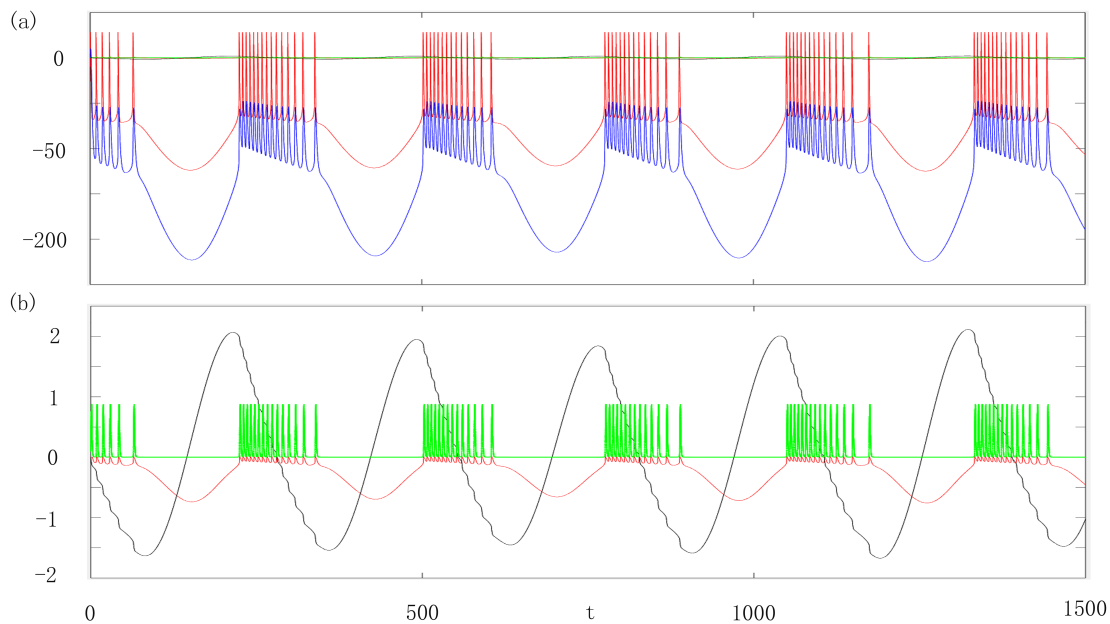


Figure 1. Time series diagrams of various variables in the neuron model under electromagnetic induction. (a) The red trajectory represents the potential time series, the blue trajectory represents the electromagnetic induction sequence diagram, and three-time series diagrams are next to the green trajectory near the zero line. (b) The enlarged image near the zero line in the Figure (a), where red represents $\rho(\phi)$, green represents the gating variable n , and black represents the feedback current I . Electromagnetic induction parameters $k = 0.00002$, $\varepsilon = 0.001$.

First, we present a time series diagram of the neuron model under electromagnetic induction. It is

found that the membrane potential of neurons exhibits a regular burster discharge pattern (in the Figure 1 red trace), and the time series of the electromagnetic induction parameter ϕ (in the Figure 1 blue trace) and the peak time of the membrane potential sequence are synchronous. The electromagnetic induction parameter ϕ affects the membrane potential of neurons at all times, although their amplitudes differ. The neuronal membrane potential strongly responds to the fluctuations of electromagnetic induction parameter ϕ . We enlarge the green curve near the zero line in the Figure 1(a) to obtain Figure 1(b), where the green trajectory represents the time series of the gating variable; the black trajectory represents the feedback current I , which is a slow regulating variable. The red trajectory shows the sequence diagram of the electromagnetic induction term $\rho(\phi)$ changing over time. Figure 1(b) shows that compared to the slowly regulated variable I , the change in the electromagnetic induction term is weaker, but the regulation of the system variables does not weaken. Its impact on the system is equivalent to adding external stimuli that change over time with a red trajectory and the membrane potential time series displayed by the system under this external stimulus. Below, we will provide the trend of the dynamic bifurcation diagram of the system as the electromagnetic induction parameters change.

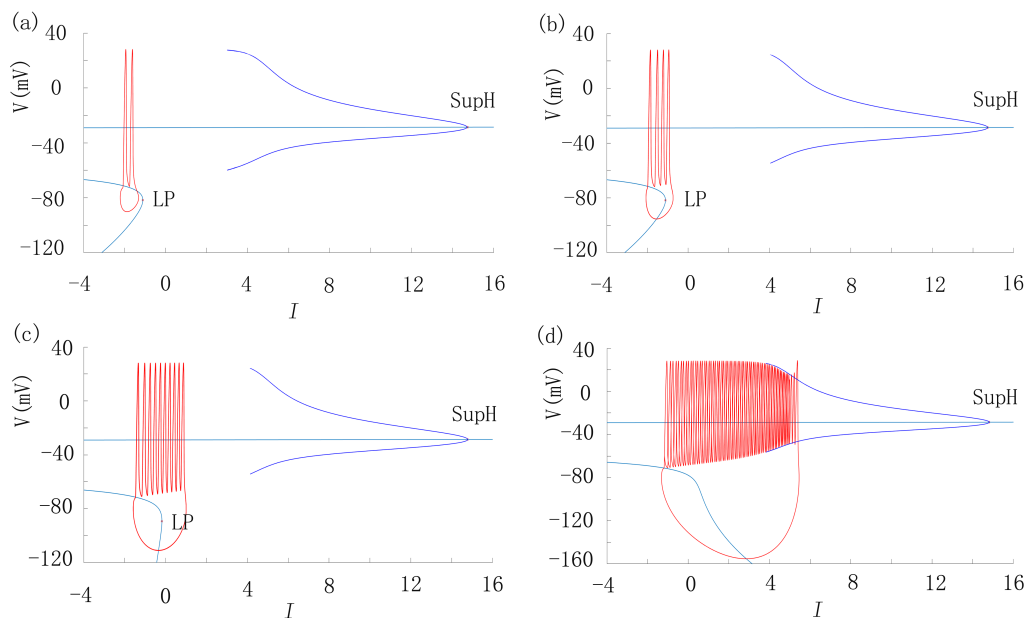


Figure 2. The bifurcation diagram of fast-slow dynamics varies with the electromagnetic induction parameters. Red represents the phase trajectory; blue represents the maximum and minimum values of the limit cycle; and green represents the equilibrium point curve. Here LP represents the saddle-node, and $supH$ represents the supercritical Hopf point. Parameter $\varepsilon = 0.001$; the electromagnetic induction parameters k are -0.000012 , -0.000008 , 0 , 0.000005 (from (a) to (d)), respectively.

From the above analysis, we know that the neuronal system's membrane potential strongly responds to electromagnetic induction as an external stimulus. Here, we take the feedback current I of the system as a slow variable and provide a bifurcation diagram of the system with the participation of electromagnetic induction. First, we can see that the system membrane potential exhibits burster discharge with ten peaks per burster when the electromagnetic induction parameter $k = 0$ (in the Figure 2(c)).

With k increased to 0.000005, the positive response of the system membrane potential to electromagnetic induction leads to a significant increase in the number of peaks per burster (in the Figure 2(d)). Based on the review about classification of bursters [15], here may show a Circle/Circle bifurcation type. With k reduced to -0.000008 , electromagnetic induction exhibits inhibition of action potential, resulting in burster discharge of membrane potential with only 4 peaks appearing in each burster (in the Figure 2(b)). When the electromagnetic induction $k = -0.000012$, the membrane potential exhibits 2 peaks per burster (in the Figure 2(a)). If the electromagnetic induction k further decreases, the system membrane potential sequence will exhibit a single spiking.

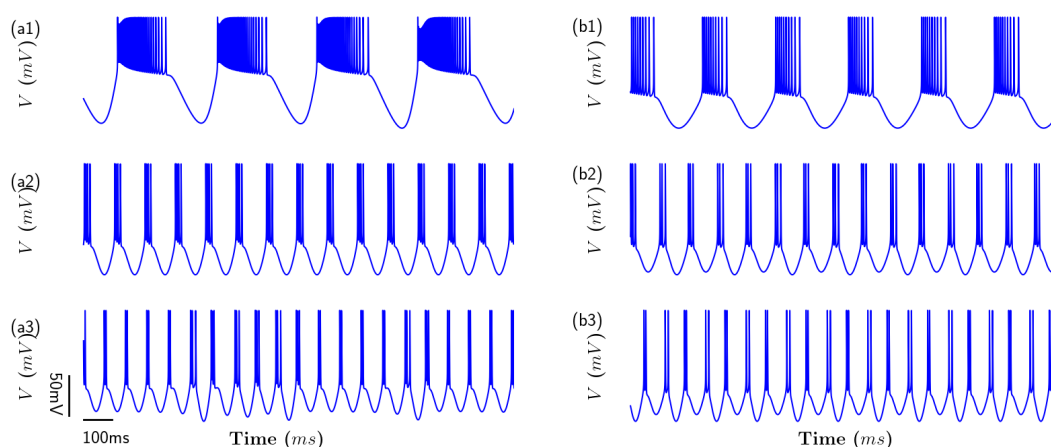


Figure 3. Time series diagram of membrane potential. The parameters ε from top to bottom are equal to 0.001, 0.005, and 0.01, respectively. On the left side is electromagnetic induction intervention, parameter $k = 0.00005$; there is no electromagnetic induction on the right side.

Here, we investigate the dynamic changes in membrane potential discharge rhythm by adding electromagnetic induction under different slow variable parameters ε . In the Figure 3, we can see that the discharge rhythm of the membrane potential exhibits a regular rectangular wave burster (in the Figure 3(b1)) when the parameter $\varepsilon = 0.001$, and the discharge rhythm of the membrane potential exhibits a parabolic burster when electromagnetic induction is added to the system (in the Figure 3(a1)). The number of peaks per burster significantly increases. When the parameter $\varepsilon = 0.005$, the system exhibits a regular burster discharge rhythm pattern, and the number of bursters within the same time interval significantly increases (in the Figure 3(b2)), and the burster interval decreases. The addition of electromagnetic induction transforms the discharge rhythm of the membrane potential from an initial irregular burster to a regular burster, and the number of peaks per burster increases (in the Figure 3(a2)). The membrane potential of the system exhibits a periodic burster when the parameter $\varepsilon = 0.01$ (in the Figure 3(b3)), and two peaks appear in each burster, with a smaller burster interval than the first two groups. Adding electromagnetic induction results in an irregular discharge rhythm of the membrane potential. The system's sensitivity increases with the addition of electromagnetic induction under this parameter (in the Figure 3(a3)). In summary, electromagnetic induction significantly impacts the membrane potential rhythm of individual neurons.

2.2. HCOs-based model

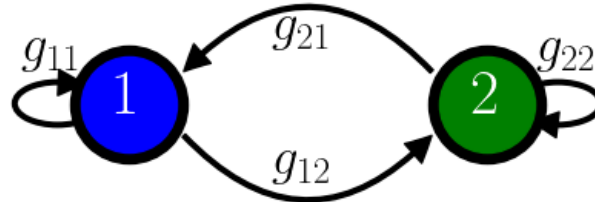


Figure 4. Connection diagram of an improved HCO with autapse (coupled system with chemical synapse). The solid blue and green circles represent neurons and are labeled as 1 and 2, respectively. These neurons are modeled by the HH model; see Eq (2.1). Black filled arrows represent inhibitory synapses; see Eq (2.2). The conductance of the connection between neurons is noted as g_{ij} , $i, j = 1, 2$. This indicates that the synapse is from neuron i to neuron j .

Next, we will consider the improved firing rhythm of two neurons that mutually inhibit each other, also known as HCOs. We have added two self-synapses of neurons here. Considering how the synchronization of neurons changes with changes in two sets of synaptic parameters, we first examine whether inhibition from autapse and mutual inhibition is consistent. Furthermore, we research HCOs in both symmetric and asymmetric autapse modes. When only g_{12} is not 0 and only g_{11} or g_{22} is not 0, we investigate the difference in the firing rhythm of neurons. The inhibitory relationship between neurons is a crucial factor in rhythm generation. The most common structure describing firing rhythmic activities consists of two coupled neurons that inhibit each other (in the Figure 4). This structure is widely known as an HCO and is symmetrically coupled through both inhibitory connections with g_{12} and g_{21} . We will start with the most straightforward network where two cells next section and extended self-inhibition from neurons. Neurons are color-coded (blue and green) based on firing activity. The synaptic transmission in the structure of the HCO in the Figure 4 is ionotropic synapses. First-order kinetic equations model these synapses, which are inhibitory and conductance-based, similar to previous studies [41–44]:

$$\begin{cases} I_{pre \rightarrow post} = g_{pre \rightarrow post} H_{\infty}(V_{pre}) (V_{pre} - E_{pre \rightarrow post}), \\ H_{\infty}(V_{pre}) = \frac{1}{1 + \exp\left(-\frac{V_{pre} - \theta}{\sigma}\right)}. \end{cases} \quad (2.2)$$

Here, V_{pre} is the presynaptic voltage, $\sigma = 1mV$ is the steepness, $\theta = -60mV$ sets the value when the function is semi-activated, $E_{pre \rightarrow post} = -110$ is the reversal potential, and $g_{pre \rightarrow post}$ is the maximal conductance (g_{ij} , $i, j = 1, 2$ in the Figure 4).

For numerical integration of network system, the fourth-order Runge–Kutta algorithm was used with a time step of $0.05\ ms$. The total integration time length of each simulation run was $5000\ ms$.

Simulations were implemented in Python 3.9.7 on PC with 12th Gen Intel(R) Core(TM) i7-12700H 2.30 GHz CPU.

3. Results

3.1. Rhythmic discharge of HCOs with different synaptic coupling

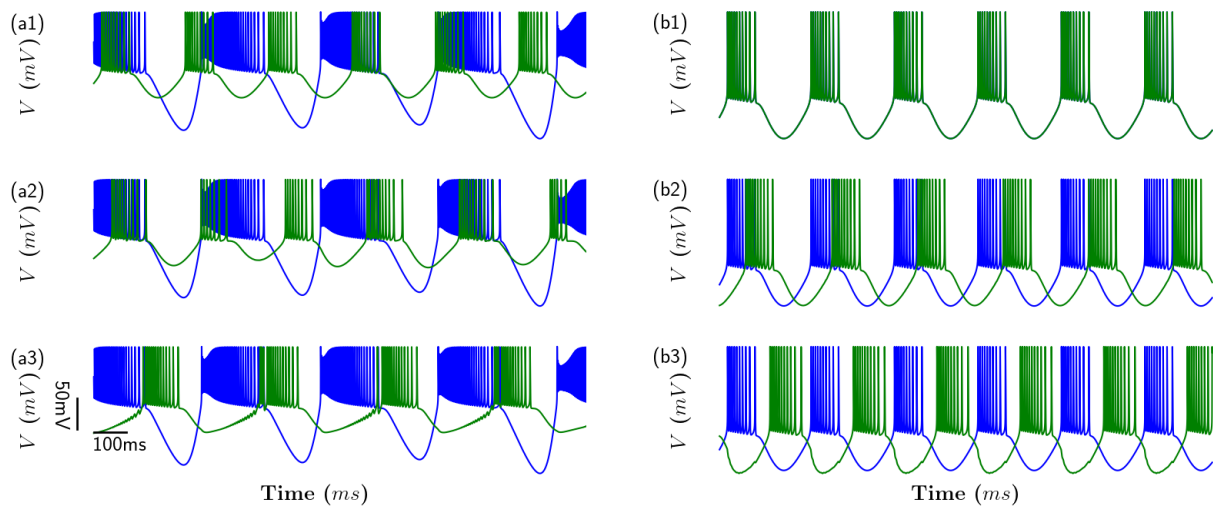


Figure 5. The discharge rhythm of HCOs when there is only one synaptic conductance change, i.e., when g_{12} changes. Here, $g_{11} = g_{21} = g_{22} = 0$. The coupling conductance parameters g_{12} from top to bottom are 0, 0.02, and 0.2, respectively. On the right side is no added electromagnetic induction; on the left, there is added electromagnetic induction, and the parameter $k = 0.00005$ only stimulates neuron 1. Blue represents the membrane potential sequence of neuron 1, and green represents the membrane potential sequence of neuron 2.

The section discusses the reciprocal inhibition between two neurons, which are HCOs (in the Figure 4). The synchronous firing of neurons contains essential neural information. Here, we investigate the synchrony of HCO rhythm activity. First, we investigate the firing rhythm when the synaptic conductance g_{12} is not zero; only neuron 1 inhibits neuron 2. When $g_{12} = 0$, neurons 1 and 2 have a wholly synchronized discharge pattern (in the Figure 5(b1)), which is reasonable. By changing g_{12} to 0.02 in Figure 5(b2), it is found that the firing rhythm of neuron 1 does not change, while the firing rhythm of neuron 2 gradually changed from the state of synchronous neuron 1 (the first two burster patterns) to an asynchronous state, until it reached an asynchronous state. When $g_{12} = 0.2$, the discharge mode of neuron 1 remains unchanged, and the discharge modes of the two neurons directly exhibit a strictly asynchronous state (in the Figure 5(b3)), with the burster mode states of neurons 1 and 2 alternating. We obtain the firing rhythm on the left side of Figure 5 when only neuron 1 in the system adds electromagnetic induction. We can observe that the rhythmic pattern of neuron 1 under electromagnetic induction is consistent under all three sets of coupled conductance parameters. Under weak coupling conductance ($g_{12} = 0.02$), the rhythmic pattern of neuron 2 transitions to irregular discharge, meaning that the discharge rhythm of neuron 2 is greatly affected by electromagnetic induction (in the Figure 5(a2)). At a relatively strong coupling conductance coefficient ($g_{12} = 0.2$) (in the Figure 5(a3)),

the burster firing rhythm pattern of neuron 2 is strengthened. We can see a significant increase in the number of peaks per burster, and the stability of the burster pattern is also more robust.

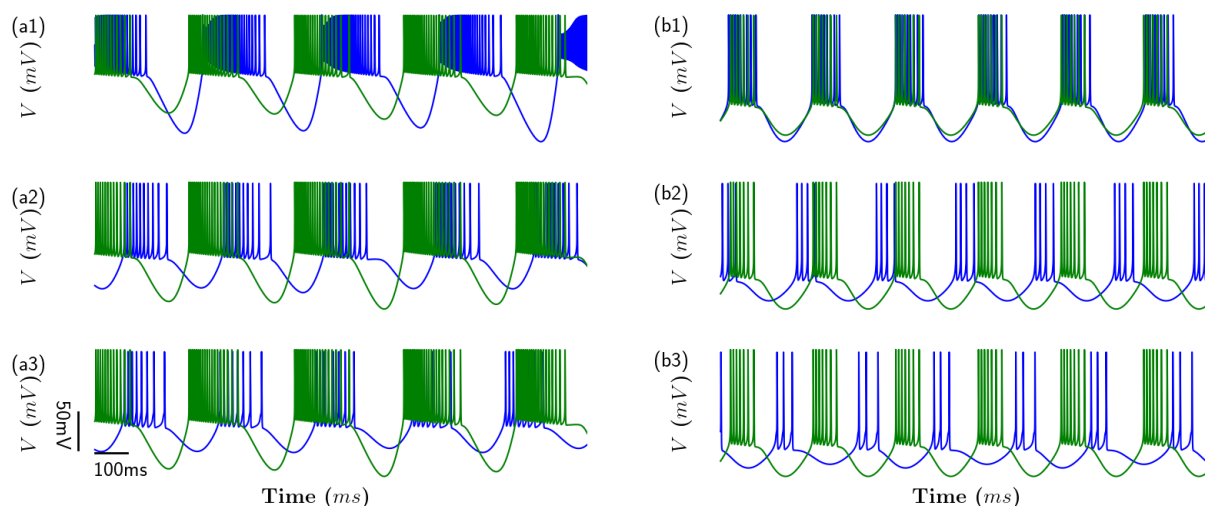


Figure 6. The discharge rhythm of HCOs. Only when the self-inhibitory synaptic conductance is not 0, that is, when only g_{11} is changed, here $g_{12} = g_{21} = 0$. As a comparison, we always take $g_{22} = 0.05$ in all the figures. The coupling conductance parameters g_{11} from top to bottom are 0, 0.2, and 0.35, respectively. On the right side, there is no added electromagnetic induction; on the left, there is added electromagnetic induction, and the parameter $k = 0.00005$. Neurons 1 and 2 are both being stimulated at the same time. Blue represents the membrane potential sequence of neuron 1, and green represents the membrane potential sequence of neuron 2.

Here, we consider the discharge rhythm when the self-inhibitory synaptic conductance changes, where $g_{12} = g_{21} = 0$. It is evident from the righthand side of Figure 6 that the firing neuron 2 has a consistent firing rhythm, unaffected by neuron 1 within a fixed g_{22} . Its firing rhythm is different from that when the coupling conductance $g_{11} = 0$ (blue trace in the Figure 6(b1)), and at this point, the firing rhythm of neuron 1 (in the Figure 6(b1)) is entirely consistent with that of neuron 1 in the Figure 5(b1). In the Figure 6(b2), when $g_{11} = 0.2$, neuron 1 shows a regular burster pattern with four peaks in each burster. This pattern is distinct from the firing rhythm pattern in the Figure 5(b3), where the coupling parameter g_{12} between neuron 1 and neuron 2 is 0.2. The different firing patterns might indicate that the inhibitory effects of autapse and mutually inhibitory synaptic conductance on neurons are different. This is an exciting observation worth noting. Here, self-inhibition reduces the number of peaks per burster in neuron 1 (in the Figure 6(b2)). When increasing g_{11} to 0.35, the discharge pattern of neuron 1 exhibits an irregular rhythm, appearing to be a burster pattern with three peaks in each burster (in the Figure 6(b3)). Continuing to increase the self-coupling synaptic conductance g_{11} , the firing rhythm of neuron 1 may transform into a burster rhythm pattern with two peaks in each burster and a regular burster discharge pattern, which is not shown here. These all indicate that self-synaptic coupling is essential to regulating the diversity of discharge rhythms. The left side of Figure 6 shows the discharge

rhythm pattern obtained by adding electromagnetic induction to the system. In all three cases, the discharge pattern of neuron 2 is undoubtedly wholly consistent. The firing pattern of neuron 1 (in the Figure 6(b1)) is consistent with the firing rhythm of neuron 1 in the Figure 5(b1) when $g_{11} = 0.2$ (in the Figure 6(a2)), and the addition of electromagnetic induction increases the number of peaks per burster in the neuron 1. When $g_{11} = 0.35$, the irregular discharge pattern of neuron 1 remains irregular under electromagnetic induction as if the number of peaks in each burster increases. Under these three types of autapse, perhaps electromagnetic induction enhances the discharge of membrane potential. We also found that the impact of electromagnetic induction on the discharge mode of HCOs varies depending on the different synaptic connections. The effects of self-synaptic inhibition and mutual inhibition on the firing patterns of neurons are also other, as shown by comparing Figures 5 and 6. Therefore, this suggests that the effects of electromagnetic induction on HCOs must be carefully considered in terms of their synaptic connections.

3.2. Synchronization of HCOs with different symmetric and asymmetric autapse

Here, we examine the synchronization state of two neurons with a half-center oscillator by phase difference $\Delta^{(n)}$ and average phase difference $S = \frac{1}{N} \sum_{n=1}^N \Delta^{(n)}$ (N is the number of samples within the range of values of the vertical coordinate parameter) [45], as shown in the Figure 7. Figure 7(a1) shows the branch diagram of the phase difference when two mutually inhibitory coupling conductance and self-synaptic conductance are equal, respectively, under the introduction of electromagnetic induction in neuron 1. The calculation results show that, without introducing electromagnetic induction, the HCO exhibits a fully synchronized state. We will discuss the discharge mode of the HCO under symmetric self-synaptic conductance, i.e., fixed self-synaptic conductance $g_{11} = g_{22} = 0$ (in the Figure 8) and $g_{11} = g_{22} = 0.2$ (in the Figure 9). When we fixed $g_{11} = 0.2$ and $g_{12} = 0.1$, we analyzed the synchronous branches of the HCO in the presence or absence of electromagnetic induction (in the Figure 7(a2),(a3)), respectively. It can be observed that the addition of electromagnetic induction fundamentally changes the phase difference of the HCO. We show the change in phase difference before and after the addition of electromagnetic induction in the Figure 7(b), which is obtained by taking the difference in phase difference at the corresponding points in the Figure 7(a2),(a3) as the dependent variable. The independent variables are conductance g_{21} and g_{22} . We will also discuss the discharge rhythm of the HCO under asymmetric self-coupling conductance (in the Figure 10).

We present the phase difference diagram of the HCO when electromagnetic induction stimulates neuron 1, and when the autapse conductance and mutual inhibition conductance are equal, respectively (in the Figure 7(a1)). We also calculated that when the autapse conductance and mutual inhibition conductance are equal (not shown in the Figure), the HCO, without introducing electromagnetic induction, is in an absolute and completely synchronized state. Here, Figure 8(b2) is a special case of complete synchronization (where $g_{11} = g_{22} = 0$, $g_{12} = g_{21} = 0.2$). At this point, whether reducing the conductance g_{12} to 0.02 or increasing g_{12} to 0.4 (in the Figure 8(b1),(b3)), not only will it change the synchronization state of the discharge patterns of the two neurons, but it will also affect the discharge rhythm patterns of the two neurons. We observed that the addition of electromagnetic induction to the synchronized state not only fundamentally altered the synchronization of the two neurons but also resulted in significant changes in the firing neuron rhythms (as shown in the Figure 8(a2)). This suggests that the discharge mode of the system in the synchronous state is more responsive to the addition of

electromagnetic induction than the asynchronous rhythm modes. These findings are consistent with our previous analysis. The number of peaks in each neurons 1 and 2 burster in the HCO gradually increases as the conductance parameter g_{21} increases from 0.02 to 0.4. Electromagnetic induction seems to make the peak changes in the firing rhythm of neurons not continuous in each burst but rather a direct burst of multiple peaks. Therefore, electromagnetic induction has a more profound impact on the synchronization of HCOs.

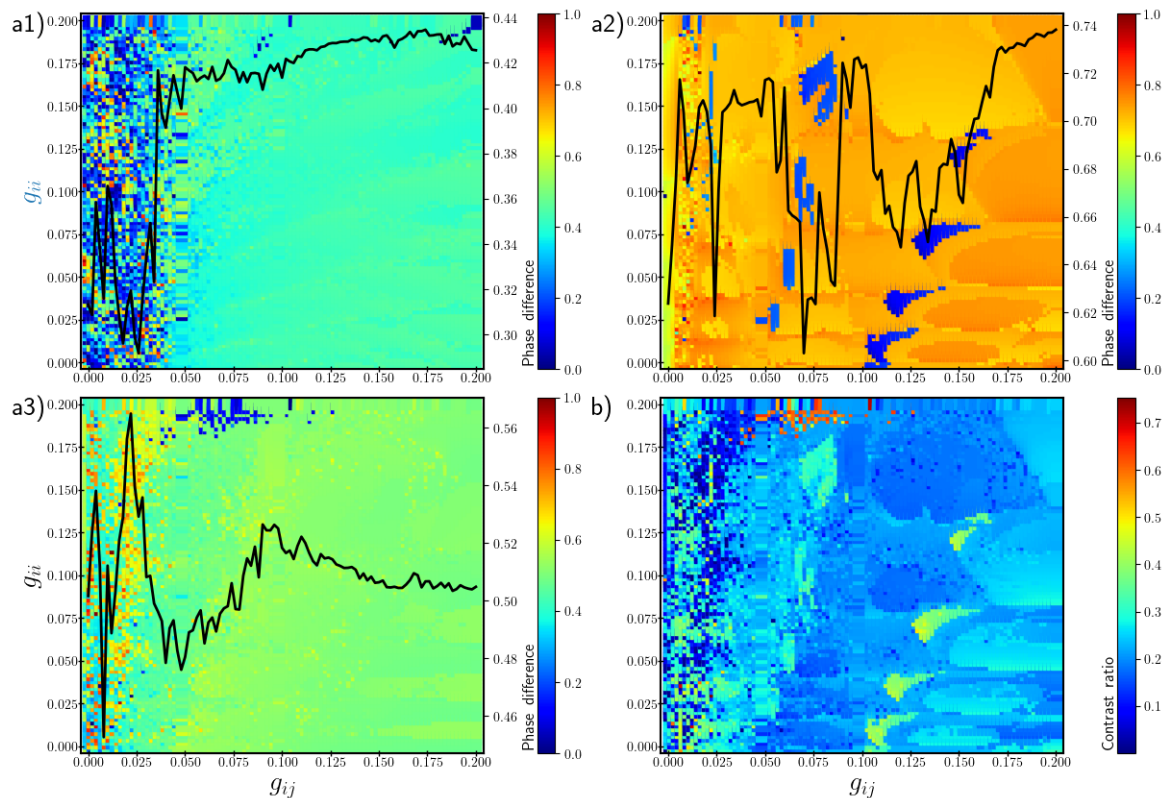


Figure 7. The combined effect of synaptic conductance g_{ii} and g_{ij} on synchronization in the HCO. The color bar indicates the phase difference $\Delta^{(n)}$, which is similar with the definition in Ref [45]. Dark blue zone corresponds to the zero phase difference (indicates complete synchronization). Dark red color indicates the maximum phase difference. Three black curves representing fixed horizontal axis values and the average phase difference (S) with changes in vertical axis values. (a1) When $g_{11} = g_{22} = g_{ii}$, $g_{12} = g_{21} = g_{ij}$, the phase difference diagram with changes in g_{ii} and g_{ij} , $k = 0.00005$, only stimulating neuron 1; (a2) Fix $g_{11} = 0.2$, $g_{12} = 0.1$, the phase difference diagram with changes in g_{21} and g_{22} , $k = 0$; (a3) Fix $g_{11} = 0.2$, $g_{12} = 0.1$, and the phase difference diagram with changes in g_{21} and g_{22} , $k = 0.00005$, only stimulating neuron 1; (b) Comparison chart of phase difference between (a2) and (a3).

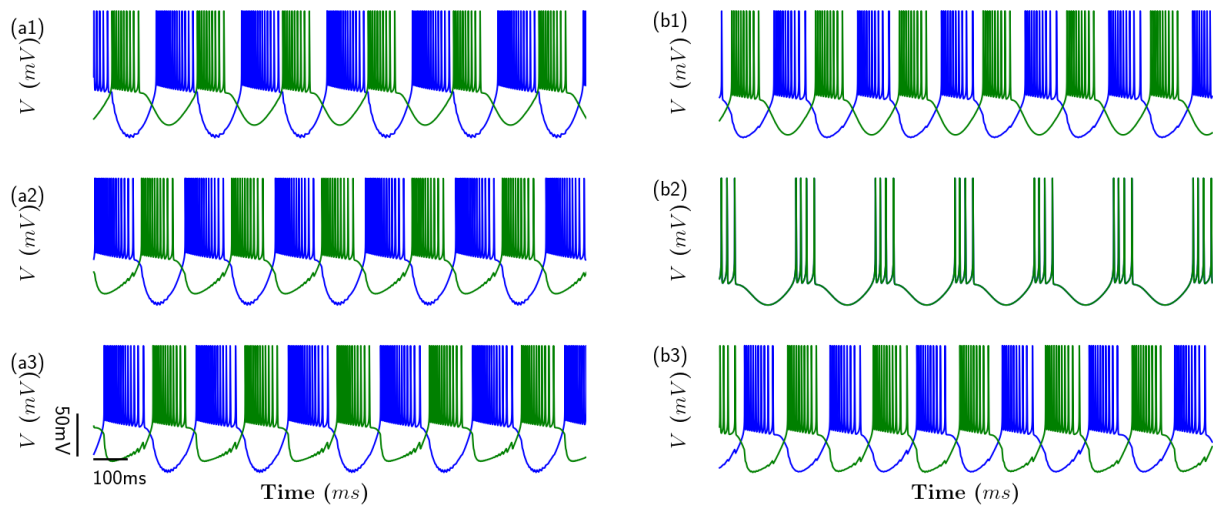


Figure 8. The discharge rhythm of the HCO when the autapse conductance $g_{11} = g_{22} = 0$. Here, g_{21} is fixed at 0.2. The conductance parameters g_{12} from top to bottom are 0.02, 0.2, and 0.4, respectively. On the right side, there is no electromagnetic induction; on the left, electromagnetic induction is added, and the parameter $k = 0.00005$ only stimulates neuron 1. Blue represents the membrane potential sequence of neuron 1, and green represents the membrane potential sequence of neuron 2.

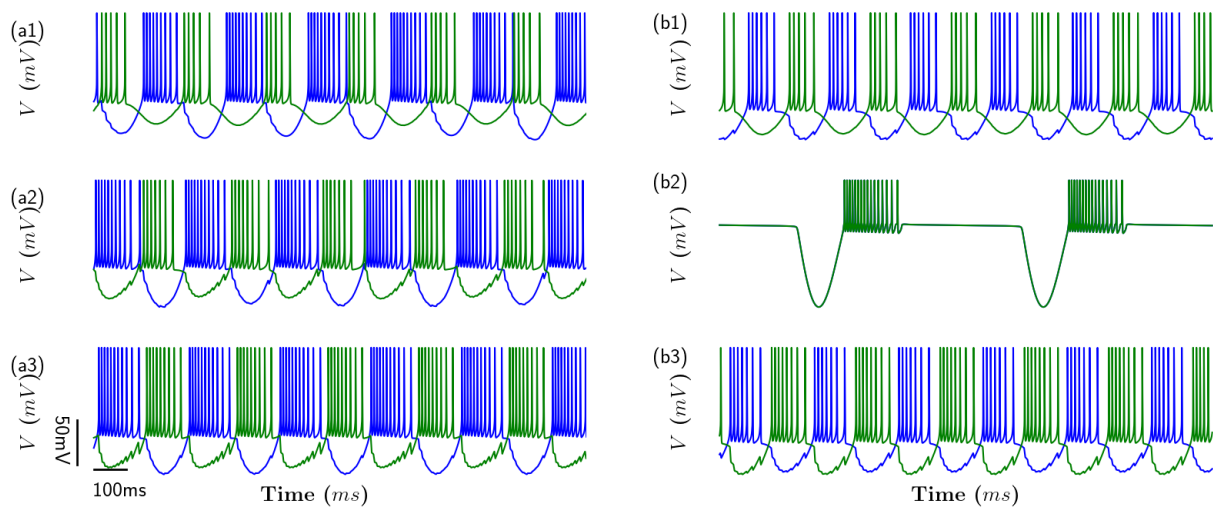


Figure 9. The discharge rhythm of HCO varies with the parameter g_{12} , where $g_{21} = 0.2$ when $g_{11} = g_{22} = 0.2$. The conductance parameters g_{12} from top to bottom are 0.02, 0.2, and 0.4, respectively. On the right side, there is no electromagnetic induction, while on the left side, electromagnetic induction is added, and the parameter $k = 0.00005$ only stimulates neuron 1. Blue represents the membrane potential sequence of neuron 1, and green represents the membrane potential sequence of neuron 2.

According to the phase difference analysis above, the two neurons in the HCO exhibit a fully syn-

chronized state when the autapse conductance and mutual inhibition conductance are equal, respectively, and no electromagnetic induction is introduced (not shown in the Figure). Figure 8(b2) shows the discharge rhythm when $g_{11} = g_{22} = 0$. In the Figure 9(b2), neurons 1 and 2 demonstrate an HCO with synchronized discharge rhythm when autapse and mutual inhibition conductance parameters are 0.2. Here, we present the discharge rhythms of the HCO when the two autapse conductance parameters are equal to 0 and 0.2, respectively (in the Figure 8(b2) and Figure 9(b2)). It is evident that the conductance parameters of autapse significantly affect the neuron's discharge rhythm. With g_{12} reduced to 0.02 (in the Figure 9(b1)), synchronization disappears, peak count decreases, and amplitude increases. When increasing $g_{12} = 0.4$ (in the Figure 9(b3)), the synchronization state of the system will also disappear, the amplitude of the peaks will increase, and the number of peaks in each burster will decrease, but it is still more than when $g_{12} = 0.02$. In an HCO, the left side of Figure 9 is obtained when electromagnetic induction stimulates neuron 1, and we can see that the synchronization state of the system immediately disappears (in the Figure 9(a2)). Neuron 1 is more sensitive to electromagnetic induction when $g_{12} = 0.02$ (in the Figure 9(a1)), while at this time, neuron 2 has almost no change in the peak number of each burster except for the change in the initial discharge time of the burster. When the value of g_{12} is 0.4 (in the Figure 9(a3)), the changes in the firing rhythms of neurons 1 and 2 show an enhanced response to electromagnetic induction. From the variation of the discharge rhythm from top to bottom on the left side, we can see that the larger the g_{12} , the better the robustness of the HCO, and the discharge rhythm in the synchronous state is more sensitive to the intervention of electromagnetic induction.

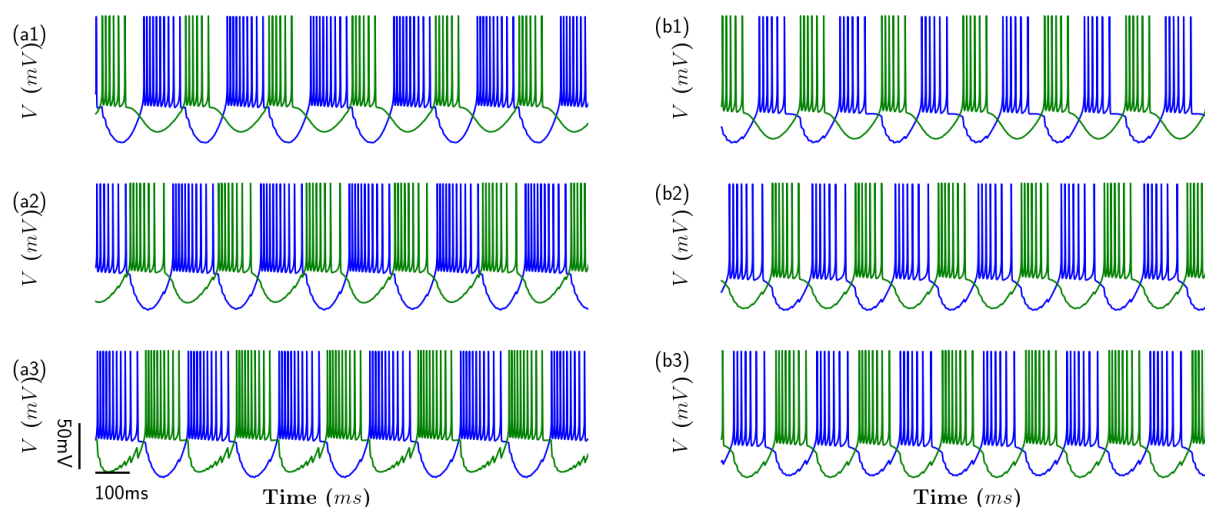


Figure 10. The discharge rhythm of HCOs varies with g_{12} when $g_{11} = 0.2$ and $g_{22} = 0.1$, where $g_{21} = 0.2$. The conductance parameters g_{12} from top to bottom are 0.02, 0.1, and 0.4, respectively. There is no electromagnetic induction on the right side, but there is electromagnetic induction on the left side that only stimulates neuron 1 with the parameter $k = 0.00005$. Blue represents the membrane potential sequence of neuron 1, and green represents the membrane potential sequence of neuron 2.

Previously, we discussed the discharge rhythms of HCOs in two cases where the conductance of two autapses is equal. Here, we will consider the discharge rhythm of the HCO at $g_{11} = 0.2$, $g_{12} = 0.1$, $g_{21} =$

0.2, and $g_{22} = 0.1$ (in the Figure 10(a2),(b2)), that is, how the discharge rhythm of the HCO changes when the autapse conductance is not equal (corresponding to a position point in the Figure 7(a2),(a3)). In addition, we also discussed the discharge rhythms of the system at $g_{12} = 0.02$ and 0.4, as shown in the Figure 10 (a1),(b1),(a3),(b3), respectively. Compared with Figure 9(b2) ($g_{12} = g_{22} = 0.2$), here we change g_{12} and g_{22} from 0.2 to 0.1, respectively, to obtain Figure 10(b2) ($g_{12} = g_{22} = 0.1$). The number of bursts and the intensity of the burst mode vary considerably. The discharge timing of the burster mode has undergone significant changes. When the value of g_{12} is 0.02, the firing rhythm of neuron 1 is significantly affected by electromagnetic induction. The peak number of each burster in neuron 2 remains unchanged, but the firing time of the burster mode is changing (in the Figure 10(a1)). When g_{12} increases by 0.1 or 0.4, the HCO becomes more sensitive to the addition of electromagnetic induction (in the Figure 10(a2),(a3)). The firing rhythm of neuron 1 directly receiving electromagnetic induction stimulation will undergo fundamental changes. The left panel of Figure 10 shows the firing rhythm of neuron 2. The larger the conductance g_{12} , the better the robustness of the system, which is consistent with our previous analysis (in the Figure 9). Here, we discuss the changes in the HCO discharge patterns of symmetric autapse (in the Figures 8 and 9) and asymmetric autapse (in the Figure 10), as well as the influence of electromagnetic induction on the discharge patterns. It is important to consider the connection modes of autapse and non-autapse connections.

4. Conclusions

In this article, we analyze the discharge rhythm of an individual neuron model under electromagnetic induction and demonstrate it as a classical burster pattern. We show the time series of slow variables, gate variables, and the electromagnetic induction term $\rho(\phi)$. It is found that the electromagnetic induction term $\rho(\phi)$ has a minor regulatory effect on the firing rhythm of neurons compared to slow variables. Moreover, we demonstrate an individual neuron's fast-slow dynamics branch diagram, which varies with different electromagnetic induction parameters. We discover that electromagnetic induction has a profound impact on the dynamic characteristics of individual neurons. Next, we examined the firing rhythms of three groups of neurons with different slow variable parameters ε . We concluded that the addition of electromagnetic induction fundamentally changes the firing rhythm of an individual neuron. We are interested in the effect of electromagnetic induction on the HCO. Here, we examine the improved HCO discharge mode, which includes the addition of autapse. The impact of autapse and mutually inhibitory synapses under electromagnetic induction on the rhythmic patterns of the HCO are considered (in the Figures 5 and 6). When the synaptic parameter values are the same, there is a significant difference in the performance of self-inhibitory synaptic and mutually inhibitory synaptic discharge patterns. Electromagnetic induction affects the discharge rhythm of the HCO differently based on the type of synapses, whether self-inhibitory or mutually inhibitory. Therefore, it is essential to take note of the connection modes of the synapses during the experiment.

Furthermore, we investigate the synchronization phenomenon of the improved HCO. The change in phase difference of the HCO with and without the introduction of electromagnetic induction is analyzed when synaptic parameters change. We discuss a comparison plot of the phase difference before and after the introduction of electromagnetic induction, which more intuitively shows the change in phase difference caused by the introduction of electromagnetic induction. By further exploring the discharge modes of the HCO and summarizing the changes in the discharge modes of the two sym-

metric autapses (in the Figures 8 and 9), it can be found that the discharge mode in the synchronous state of the system has a more robust response to electromagnetic induction compared to the asynchronous rhythmic mode. It is apparent that the larger the conductance g_{12} , the greater the robustness of the HCO. At the same time, the discharge rhythm of neuron 1 directly receiving electromagnetic induction stimulation changes significantly, while the discharge rhythm of neuron 2 passively receiving stimulation is affected by the value of g_{12} . The larger the value of g_{12} , the stronger the response of neuron 2. Finally, we analyze the changes in the discharge mode of the HCO with changes in synaptic conductance parameters under asymmetric autapse. The response patterns of the HCO of symmetric and asymmetric autapse to electromagnetic induction are different, manifested by the diverse discharge modes of the HCO.

Therefore, these rules of the HCO need to be paid attention to, including different synaptic connections, the response of different synaptic connections to electromagnetic induction, the different effects of electromagnetic induction on its synchronization, and the different effects of symmetric and asymmetric autapse on the discharge mode of the HCO. In our study, we examined chemical synapses between neurons and did not consider any electrical coupling that may have been present between them. In future studies, we will analyze the synergistic effects of electrical and chemical coupling in HCO or CPG, which can lead to very different rhythmic patterns. Our current model demonstrates that synaptic conductance can influence the rhythm pattern of the HCO. The diversity of rhythm activities in CPG is essential for its flexibility and robustness, which can resist interference from external information. Synaptic conductance and electromagnetic induction changes can produce many different rhythm activities, making the CPG less susceptible to external interference. Of course, the relationship between rhythmic activities of HCO (or CPG) and epilepsy and other diseases will also be paid attention to.

Use of AI tools declaration

The authors declare they have not used Artificial Intelligence (AI) tools in the creation of this article.

Acknowledgments

This work was funded by the National Natural Science Foundation of China (Grant Nos. 12202208), the Basic Science (Natural Science) Research Project of Colleges and Universities of Jiangsu Province (Grant No. 22KJB130009), the Research and Cultivation Project for Young Teachers of Nanjing Audit University (Grant No. 2021QNPY015), 2022 Doctoral program of Entrepreneurship and Innovation in Jiangsu Province (Grant No. JSSCBS20220717), the China Scholarship Council (Grant No. 202206150096).

Conflict of interest

The authors declare there is no conflicts of interest.

References

1. E. Marder, D. Bucher, Central pattern generators and the control of rhythmic movements, *Curr. Biol.*, **11** (2001), R986–R996. [https://doi.org/10.1016/S0960-9822\(01\)00581-4](https://doi.org/10.1016/S0960-9822(01)00581-4)

2. E. Marder, R. L. Calabrese, Principles of rhythmic motor pattern generation, *Physiol. Rev.*, **76** (1996), 687–717. <https://doi.org/10.1152/physrev.1996.76.3.687>
3. D. N. Masaev, A. A. Suleimanova, N. V. Prudnikov, M. V. Serenko, A. V. Emelyanov, V. A. Demin, et al., Memristive circuit-based model of central pattern generator to reproduce spinal neuronal activity in walking pattern, *Front. Neurosci.*, **17** (2023), 1124950. <https://doi.org/10.3389/fnins.2023.1124950>
4. D. Alaçam, A. Shilnikov, Making a swim central pattern generator out of latent parabolic bursters, *Int. J. Bifurcation Chaos*, **25** (2015), 1540003. <https://doi.org/10.1142/S0218127415400039>
5. E. Marder, S. Kedia, E. O. Morozova, New insights from small rhythmic circuits, *Curr. Opin. Neurobiol.*, **76** (2022), 102610. <https://doi.org/10.1016/j.conb.2022.102610>
6. E. Marder, Neuromodulation of neuronal circuits: back to the future, *Neuron*, **76** (2012), 1–11. <https://doi.org/10.1016/j.neuron.2012.09.010>
7. T. Nowotny, M. I. Rabinovich, Dynamical origin of independent spiking and bursting activity in neural microcircuits, *Phys. Rev. Lett.*, **98** (2007), 128106. <https://doi.org/10.1103/PhysRevLett.98.128106>
8. M. Lodi, A. L. Shilnikov, M. Storace, Design principles for central pattern generators with preset rhythms, *IEEE Trans. Neural Networks Learn. Syst.*, **31** (2019), 3658–3669. <https://doi.org/10.1109/TNNLS.2019.2945637>
9. J. T. C. Schwabedal, A. B. Neiman, A. L. Shilnikov, Robust design of polyrhythmic neural circuits, *Phys. Rev. E*, **90** (2014), 022715. <https://doi.org/10.1103/PhysRevE.90.022715>
10. J. Collens, K. Pusuluri, A. Kelley, D. Knapper, T. Xing, S. Basodi, et al., Dynamics and bifurcations in multistable 3-cell neural networks, *Chaos*, **30** (2020), 072101. <https://doi.org/10.1063/5.0011374>
11. Q. Lu, J. Tian, Synchronization and stochastic resonance of the small-world neural network based on the CPG, *Cognit. Neurodyn.*, **8** (2014), 217–226. <https://doi.org/10.1007/s11571-013-9275-8>
12. Y. Zang, S. Hong, S. E. De, Firing rate-dependent phase responses of Purkinje cells support transient oscillations, *eLife*, **9** (2020), e60692. <https://doi.org/10.7554/eLife.60692>
13. B. S. Gutkin, G. B. Ermentrout, A. D. Reyes, Phase-response curves give the responses of neurons to transient inputs, *J. Neurophysiol.*, **94** (2005), 1623–1635. <https://doi.org/10.1152/jn.00359.2004>
14. Y. Zang, E. Marder, Neuronal morphology enhances robustness to perturbations of channel densities, *PNAS*, **120** (2023), e2219049120. <https://doi.org/10.1073/pnas.2219049120>
15. E. M. Izhikevich, Neural excitability, spiking, and bursting, *Int. J. Bifurcation Chaos*, **10** (2000), 1171–1266. <https://doi.org/10.1142/S0218127400000840>
16. B. Lu, X. Jiang, Reduced and bifurcation analysis of intrinsically bursting neuron model, *Electron. Res. Arch.*, **31** (2023), 5928–5945. <https://doi.org/10.3934/era.2023301>
17. F. Zhan, S. Liu, X. Zhang, J. Wang, B. Lu, Mixed-mode oscillations and bifurcation analysis in a pituitary model, *Nonlinear Dyn.*, **94** (2018), 807–826. <https://doi.org/10.1007/s11071-018-4395-7>

18. H. Zhou, B. Lu, H. Gu, X. Wang, Y. Liu, Complex nonlinear dynamics of bursting of thalamic neurons related to Parkinson's disease, *Electron. Res. Arch.*, **32** (2024), 109–133. <https://doi.org/10.3934/era.2024006>
19. Z. Song, J. Xu, Codimension-two bursting analysis in the delayed neural system with external stimulations, *Nonlinear Dyn.*, **67** (2012), 309–328. <https://doi.org/10.1007/s11071-011-9979-4>
20. W. B. Kristan, Neuronal decision-making circuits, *Curr. Biol.*, **18** (2008), R928–R932. <https://doi.org/10.1016/j.cub.2008.07.081>
21. K. L. Briggman, W. B. Kristan, Multifunctional pattern-generating circuits, *Annu. Rev. Neurosci.*, **31** (2008), 271–294. <https://doi.org/10.1146/annurev.neuro.31.060407.125552>
22. J. Wojcik, J. Schwabedal, R. Clewley, A. L. Shilnikov, Key bifurcations of bursting polyrhythms in 3-cell central pattern generators, *PLoS One*, **9** (2014), e92918. <https://doi.org/10.1371/journal.pone.0092918>
23. C. A. Tassinari, G. Cantalupo, B. Hoegl, P. Cortelli, L. Tassi, S. Francione, et al., Neuroethological approach to frontolimbic epileptic seizures and parasomnias: the same central pattern generators for the same behaviours, *Rev. Neurol.*, **165** (2009), 762–768. <https://doi.org/10.1016/j.neurol.2009.08.002>
24. C. A. Tassinari, E. Gardella, G. Cantalupo, G. Rubboli, Relationship of central pattern generators with parasomnias and sleep-related epileptic seizures, *Sleep Med. Clin.*, **7** (2012), 125–134. <https://doi.org/10.1016/j.jsmc.2012.01.003>
25. F. Zhan, J. Song, S. Liu, The influence of synaptic strength and noise on the robustness of central pattern generator, *Electron. Res. Arch.*, **32** (2024), 686–706. <https://doi.org/10.3934/era.2024033>
26. V. Baruzzi, M. Lodi, M. Storace, A. Shilnikov, Towards more biologically plausible central-pattern-generator models, *Phys. Rev. E*, **104** (2021), 064405. <https://doi.org/10.1103/PhysRevE.104.064405>
27. R. L. Calabrese, Half-center oscillators underlying rhythmic movements, in *The Handbook of Brain Theory and Neural Networks*, (1998), 444–447.
28. A. Sakurai, P. S. Katz, The central pattern generator underlying swimming in *Dendronotus iris*: a simple half-center network oscillator with a twist, *J. Neurophysiol.*, **116** (2016), 1728–1742. <https://doi.org/10.1152/jn.00150.2016>
29. A. Doloc-Mihu, R. L. Calabrese, A database of computational models of a half-center oscillator for analyzing how neuronal parameters influence network activity, *J. Biol. Phys.*, **37** (2011), 263–283. <https://doi.org/10.1007/s10867-011-9215-y>
30. A. Doloc-Mihu, R. L. Calabrese, Analysis of family structures reveals robustness or sensitivity of bursting activity to parameter variations in a half-center oscillator (HCO) model, *eNeuro*, **3** (2016). <https://doi.org/10.1523/ENEURO.0015-16.2016>
31. Z. Song, J. Xu, Multiple switching and bifurcations of in-phase and anti-phase periodic orbits to chaotic coexistence in a delayed half-center CPG oscillator, *Nonlinear Dyn.*, **111** (2023), 16569–16584. <https://doi.org/10.1007/s11071-023-08670-w>
32. Z. Song, J. Xu, Multi-coexistence of routes to chaos in a delayed half-center oscillator (DHCO) system, *Nonlinear Dyn.*, **112** (2024), 1469–1486. <https://doi.org/10.1007/s11071-023-09089-z>

33. A. J. White, Sensory feedback expands dynamic complexity and aids in robustness against noise, *Biol. Cybern.*, **116** (2022), 267–269. <https://doi.org/10.1007/s00422-021-00917-2>
34. F. Zhan, S. Liu, Response of electrical activity in an improved neuron model under electromagnetic radiation and noise, *Front. Comput. Neurosci.*, **11** (2017), 107. <https://doi.org/10.3389/fncom.2017.00107>
35. Z. Wang, Y. Yang, L. Duan, Control effects of electromagnetic induction on epileptic seizures, *Nonlinear Dyn.*, **112** (2024). <https://doi.org/10.1007/s11071-024-09373-6>
36. A. S. Lele, Y. Fang, J. Ting, A. Raychowdhury, Learning to walk: bio-mimetic hexapod locomotion via reinforcement-based spiking central pattern generation, *IEEE J. Emerging Sel. Top. Circuits Syst.*, **10** (2020), 536–545. <https://doi.org/10.1109/JETCAS.2020.3033135>
37. T. Sun, Z. Dai, P. Manoonpong, Distributed-force-feedback-based reflex with online learning for adaptive quadruped motor control, *Neural Networks*, **142** (2021), 410–427. <https://doi.org/10.1016/j.neunet.2021.06.001>
38. B. Muthuswamy, Implementing memristor based chaotic circuits, *Int. J. Bifurcation Chaos*, **20** (2010), 1335–1350. <https://doi.org/10.1142/S0218127410026514>
39. M. Lv, C. Wang, G. Ren, J. Ma, X. Song, Model of electrical activity in a neuron under magnetic flow effect, *Nonlinear Dyn.*, **85** (2016), 1479–1490. <https://doi.org/10.1007/s11071-016-2773-6>
40. F. Zhan, S. Liu, J. Wang, B. Lu, Bursting patterns and mixed-mode oscillations in reduced Purkinje model, *Int. J. Mod. Phys. B*, **32** (2018), 1850043. <https://doi.org/10.1142/S0217979218500431>
41. D. Terman, J. E. Rubin, A. C. Yew, C. J. Wilson, Activity patterns in a model for the subthalamopallidal network of the basal ganglia, *J. Neurosci.*, **22** (2002), 2963–2976. <https://doi.org/10.1523/JNEUROSCI.22-07-02963.2002>
42. F. Su, J. Wang, S. Niu, H. Li, B. Deng, C. Liu, et al., Nonlinear predictive control for adaptive adjustments of deep brain stimulation parameters in basal ganglia–thalamic network, *Neural Networks*, **98** (2018), 283–295. <https://doi.org/10.1016/j.neunet.2017.12.001>
43. J. Song, S. Liu, H. Lin, Model-based quantitative optimization of deep brain stimulation and prediction of Parkinson’s states, *Neuroscience*, **498** (2022), 105–124. <https://doi.org/10.1016/j.neuroscience.2022.05.019>
44. J. Song, H. Lin, S. Liu, Basal ganglia network dynamics and function: role of direct, indirect and hyper-direct pathways in action selection, *Network: Comput. Neural Syst.*, **34** (2023), 84–121. <https://doi.org/10.1080/0954898X.2023.2173816>
45. Z. Song, F. Ji, J. Xu, Is there a user-friendly building unit to replicate rhythmic patterns of CPG systems? Synchrony transition and application of the delayed bursting-HCO model, *Chaos, Solitons Fractals*, **182** (2024), 114820. <https://doi.org/10.1016/j.chaos.2024.114820>



AIMS Press

© 2024 the Author(s), licensee AIMS Press. This is an open access article distributed under the terms of the Creative Commons Attribution License (<http://creativecommons.org/licenses/by/4.0>)

国家自然科学基金资助项目批准通知

(包干制项目)

詹飞彪 先生/女士:

根据《国家自然科学基金条例》、相关项目管理办法规定和专家评审意见,国家自然科学基金委员会(以下简称自然科学基金委)决定资助您申请的项目。项目批准号: 12202208, 项目名称: 神经元模型的节律转迁机理及网络动力学研究, 资助经费: 30.00万元, 项目起止年月: 2023年01月至 2025年12月, 有关项目的评审意见及修改意见附后。

请您尽快登录科学基金网络信息系统(<https://isisn.nsfc.gov.cn>), **认真阅读《国家自然科学基金资助项目计划书填报说明》并按要求填写《国家自然科学基金资助项目计划书》(以下简称计划书)**。对于有修改意见的项目,请您按修改意见及时调整计划书相关内容;如您对修改意见有异议,须在电子版计划书报送截止日期前向相关科学处提出。

请您将电子版计划书通过科学基金网络信息系统(<https://isisn.nsfc.gov.cn>)提交,由依托单位审核后提交至自然科学基金委。自然科学基金委审核未通过者,将退回的电子版计划书修改后再行提交;审核通过者,打印纸质版计划书(一式两份,双面打印)并在项目负责人承诺栏签字,由依托单位在承诺栏加盖依托单位公章,且将申请书纸质签字盖章页订在其中一份计划书之后,一并报送至自然科学基金委项目材料接收工作组。纸质版计划书应当保证与审核通过的电子版计划书内容一致。**自然科学基金委将对申请书纸质签字盖章页进行审核,对存在问题的,允许依托单位进行一次修改或补齐。**

向自然科学基金委提交电子版计划书、报送纸质版计划书并补交申请书纸质签字盖章页截止时间节点如下:

1. **2022年10月8日16点:** 提交电子版计划书的截止时间;
2. **2022年10月14日16点:** 提交修改后电子版计划书的截止时间;
3. **2022年10月19日:** 报送纸质版计划书(一式两份,其中一份包含申请书纸质签字盖章页)的截止时间。
4. **2022年10月28日:** 报送修改后的申请书纸质签字盖章页的截止时间。

请按照以上规定及时提交电子版计划书，并报送纸质版计划书和申请书纸质签字盖章页，逾期不报计划书或申请书纸质签字盖章页且未说明理由的，视为自动放弃接受资助；未按要求修改或逾期提交申请书纸质签字盖章页者，将视情况给予暂缓拨付经费等处理。

附件：项目评审意见及修改意见表

国家自然科学基金委员会
2022年9月7日

获奖证书

詹飞彪 老师：

在第六届南京审计大学教师教学创新大赛中，荣获
二等奖。

团队成员：陆伟东、郑玉国、李亮
特发此证，以资鼓励。



二〇二五年十二月二十四日

获奖证书

certificate of award

南京审计大学的参赛作品《基于人工智能方法的农业灾害监测研究》，在
2024年（第十届）全国大学生统计建模大赛 江苏赛区 赛区选拔赛中，荣获本科生
组一等奖。

参赛队员：孔惟一、韩雅玥、苗馨悦

指导老师：詹飞彪

证书编号：20242001A0031

中国统计教育学会
二〇二四年七月

